7-2016

Synthesis and Applications of Lanthanide Sulfides and Oxides

Christopher Marin

University of Nebraska-Lincoln, cmarin@huskers.unl.edu

SYNTHESIS AND APPLICATIONS OF LANTHANIDE

SULFIDES AND OXIDES

by

Christopher Mark Marin

A DISSERTATION

Presented to the Faculty of

The Graduate College at the University of Nebraska

In Partial Fulfillment of Requirements

For the Degree of Doctor of Philosophy

Major: Chemistry

Under the Supervision of Professor Chin Li "Barry" Cheung

Lincoln, Nebraska

July, 2016

SYNTHESIS AND APPLICATIONS OF LANTHANIDE

SULFIDES AND OXIDES

Christopher Mark Marin, Ph.D.

University of Nebraska, 2016

Advisor: Chin Li "Barry" Cheung

The chemistry of the lanthanide and actinide elements remains the last great frontier of the periodic table. While many main group and transition metal elements have been known from antiquity, it was not until the late 20th century that the lanthanides found ready industrial and commercial applications as phosphors, optical coatings, polishing agents, and catalytic applications. This dissertation focuses on two of the key fields where lanthanides find ready application: as optically active materials with a focus on the lanthanide sulfides, and as catalytic materials with a focus on cerium oxide.

The lanthanide sulfides have attracted considerable interest for their potential as solar energy conversion materials, pigments, infrared window materials, and phosphor host media. All of these properties stem from their semiconducting properties with useable band gaps ranging from 2.7 to 0 eV. However, applications of these materials remain limited due to their synthetic difficulty along with their not well understood properties compounded by both their difficulty in manufacturing as well as in simulating largely due to the need to take into account f-shell electrons. This dissertation presents the fundamental band properties of lanthanum, gadolinium,

and samarium sulfides as well as a rapid chemical vapor deposition method for the synthesis of highly textured samarium sulfide thin films.

Even more than the sulfides, the lanthanide oxides have attracted tremendous interest from industry and academia for their use as phosphors and catalytic applications, most notably cerium oxide in automotive three-way catalysts and in the petroleum industry as a cracking catalyst. In contrast to the lanthanide sulfides, the syntheses of the oxides are rapid and inexpensive causing many of the oxides to find ready applications even though the complexities of their chemistries are not yet well understood. This dissertation presents the fundamental kinetics and mechanism investigations for cerium oxide (ceria) as it is used for catalyzing the direct synthesis of organic carbonates from CO_2 and methanol. This reaction is of particular interest due to its slow kinetics allowing for fundamental investigations, while ready industrial demand for organic carbonates and CO_2 utilization mean that this chemistry may find ready application.

ACKNOWLEDGEMENTS

Even more so, I would like to thank my advisor Dr. Chin Li "Barry" Cheung for his training, guidance, and especially his patience, which has enabled me to complete my doctoral studies at the University of Nebraska-Lincoln. His perseverance, support, and unwavering curiosity have provided me with the opportunities and the knowledge to carry out the following research. More than that though, his high standards and strong work ethic have taught me what it means to be a professional. Additionally, I would like to thank my committee members: Dr. Rebecca Lai, Dr. Xiao Cheng Zeng, Dr. Alexander Sinitskii, and Dr. Natale Ianno for their support, thoughtful critiques, and for being willing to listen and bounce ideas against.

I would also like to acknowledge my collaborators Dr. Wai-Ning Mei, Dr. Lu Wang, Dr. Xiao Cheng Zeng, and Lei Li for their hard work in simulating band structures and mechanistic pathways. I'm ever grateful for Dr. Martha Morton for her help and expertise in organic characterization. Additionally, I am grateful for my current and former group mates: Anuja Bhalkikar, Tamra Fisher, Bin Wang, Zane Gernhart, Yunyun Zhou, Neil Lawrence, Joseph Brewer, and Dr. Dar for their help, support, patience, and advice. I'm also extremely grateful to my undergraduate students James Doyle and José Santana.

I would like to thank the UNL Chemistry Department, the Morrison Microscopy Core Research Facility, the Nebraska Center for Materials and Nanoscience, and the University of Alabama's Central Analytical Facility for use of their equipment.

Additionally, I'm extremely grateful for Dr. Johnny Goodwin (of the University of Alabama) and Drs. You Zhou and Han Chen who taught me most of what I really know about electron microscopy.

Finally, I would like to thank my family and friends for their love, encouragement, and support. They always heard me out and encouraged me even through the roughest of days.

Contents

Chapter 1 Introduction to lanthanide sulfides

Chapter 2 Band properties of lanthanum, samarium, and gadolinium sulfides

Chapter 3 Synthesis structure and optical properties of Sm$_2$S$_3$

Chapter 4 Sulfides summary and future directions

Chapter 5 Introduction to cerium oxide and CO$_2$ chemistry

Chapter 6 Method development for separating organic carbonates

Chapter 7 Kinetics and mechanistic insights in the ceria catalyzed conversion of methanol and CO$_2$ to dimethyl carbonate

Chapter 8 Future studies

Chapter 1

INTRODUCTION TO LANTHANIDE SULFIDES

1.1 The lanthanide series

The lanthanide series of metals were some of the last elements to be discovered and isolated. The discovery of the first lanthanides, lanthanum and cerium, is credited to Mosander ~1840 CE, isolated from previously discovered cerium earths [1]. However, it took close to a hundred years for the remaining lanthanide elements to be isolated and discovered. Notably for this thesis, samarium and europium were not discovered until 1901 CE [1]. The reason for this long delay was twofold: the lanthanides were thought to be rare due to the scarcity of natural samples rich in lanthanides, and they were extremely difficult to separate due to the entire series preferring to take a +3 oxidation state similar to scandium and yttrium. Because of their assumed low abundance and difficulty in isolating, the lanthanides, scandium, and yttrium were all grouped together under the label "rare earth elements" and set as a footnote to the periodic table (Figure 1.1).

In this thesis, the lanthanide series will not be referred to as "rare earths". The reason for this is simple: the "rare earths" are not rare in terms of crustal abundance. For instance, cerium is the most abundant "rare earth element", and exceeds in crustal abundance such commonly encountered metals as tin, cobalt, or lead [2]. Even the least abundant lanthanide (lutetium) exceeds the crustal abundance of indium, silver, or mercury, and is orders of magnitude greater in abundance than gold and platinum [3] (Figure 1.2). Instead, the term lanthanide will be used (Ln) taken to mean the 15 elements
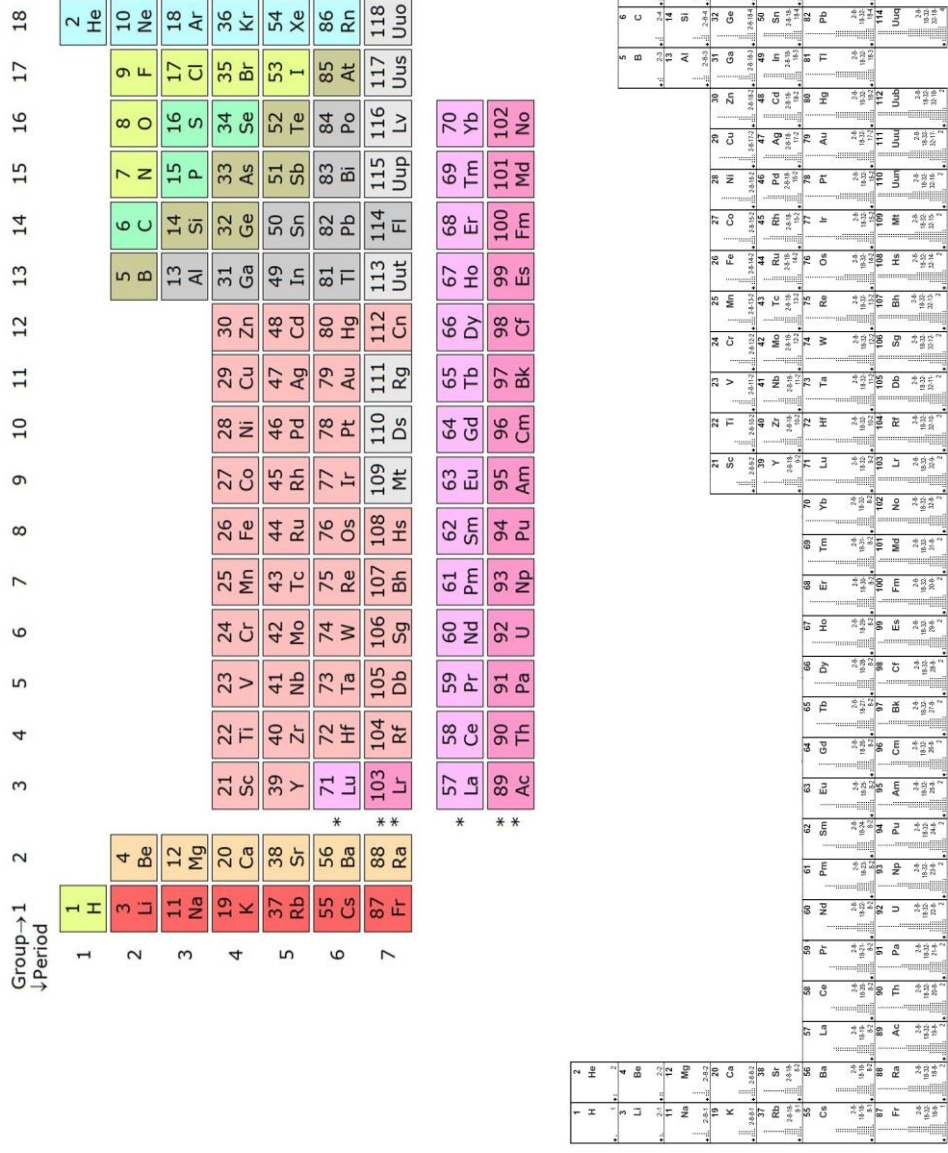
Figure 1.1 Typical periodic table as compared to the true "extended" periodic table. Note the inclusion of the lanthanides as a separate block from the transition metals instead of as a footnote. Both tables distributed under a CC-BY 4.0 license.
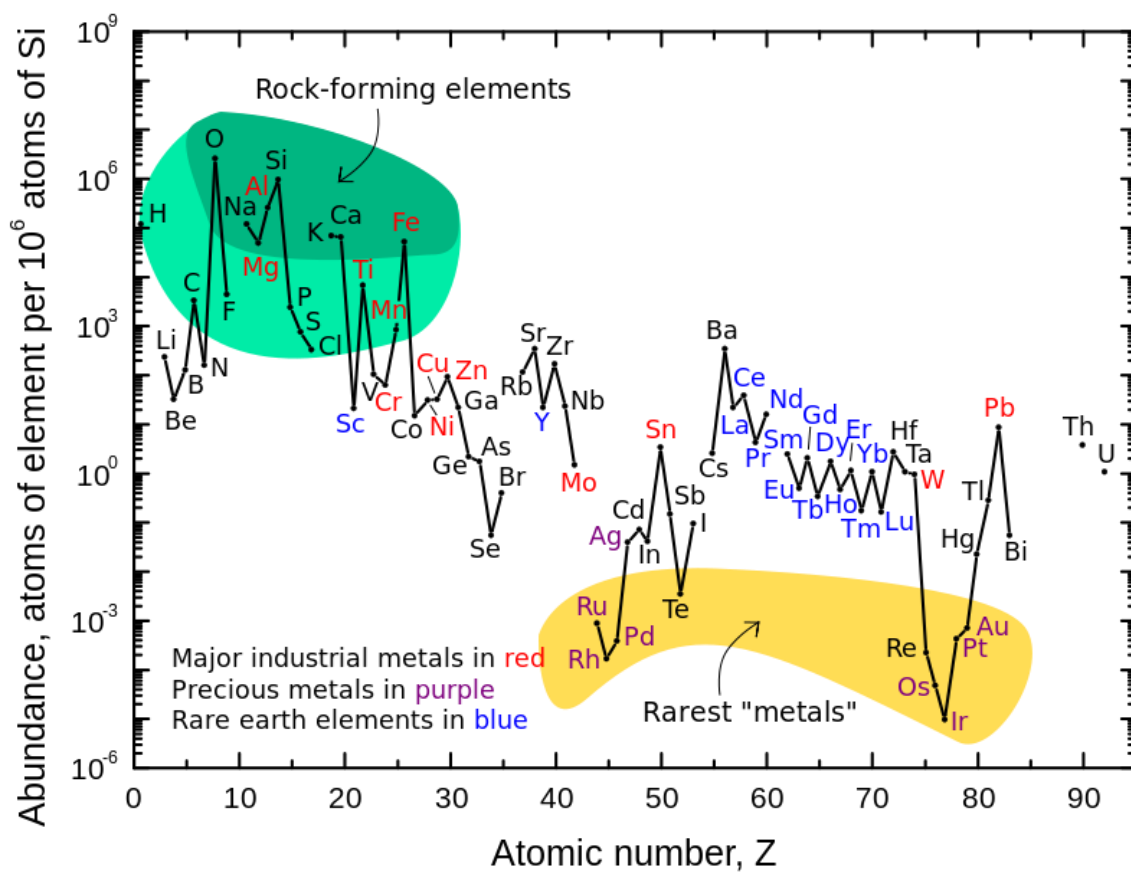
Figure 1.2 Earth crustal abundance of the elements. Note the "rare earth" elements are in blue. Image courtesy of the U.S. Geological Survey. [3]

lanthanum (La^{57}) through lutetium (Lu^{71}). Note that various periodic tables may classify lanthanum or lutetium as d-block elements due to both containing a valence d-shell electron. However, chemically they behave the same as the lanthanides in between and it is thematically useful to include the whole f-block series from zero through 14 f-shell electrons.

1.2 Electronic structure of the lanthanides

All of the lanthanide elements prefer to take a 3+ oxidation state. In contrast to the range of oxidation states present in the d-block metals, the highest oxidation states achievable by the lanthanides is a 4+ state, and this is only by cerium and terbium because it enables them to take a f^0 and an f^{14} configuration respectively. Because of the prevalence of the 3+ state, the electronic structure of the lanthanides was originally hypothesized to be $[Xe]4f^x5d^16s^2$. An electronic structure of this form would neatly explain the prevalence of the 3+ state: there are three valence electrons and the f electrons are too internalized for removal. Unfortunately, spectroscopic studies have failed to show a 5d electron in any of the lanthanides other than lanthanum and lutetium, meaning that from cerium to ytterbium, the electronic structure takes the form $[Xe]4f^x6s^2$ [4] (Table 1.1). Clearly then, some explanation is necessary in order to explain why the lanthanides readily lose three electrons, and rarely any more or less.

Name	Chemical Symbol	Atomic Number	Atomic Configuration	3+ Ion
Lanthanum	La	57	$[Xe]5d6s^2$	$[Xe]$
Cerium	Ce	58	$[Xe]4f^26s^2$	$[Xe]4f$
Praseodymium	Pr	59	$[Xe]4f^36s^2$	$[Xe]4f^2$
Neodymium	Nd	60	$[Xe]4f^46s^2$	$[Xe]4f^3$
Promethium	Pm	61	$[Xe]4f^56s^2$	$[Xe]4f^4$
Samarium	Sm	62	$[Xe]4f^66s^2$	$[Xe]4f^5$
Europium	Eu	63	$[Xe]4f^76s^2$	$[Xe]4f^6$
Gadolinium	Gd	64	$[Xe]4f^75d6s^2$	$[Xe]4f^7$
Terbium	Tb	65	$[Xe]4f^96s^2$	$[Xe]4f^8$
Dysprosium	Dy	66	$[Xe]4f^{10}6s^2$	$[Xe]4f^9$
Holmium	Ho	67	$[Xe]4f^{11}6s^2$	$[Xe]4f^{10}$
Erbium	Er	68	$[Xe]4f^{12}6s^2$	$[Xe]4f^{11}$
Thulium	Tm	69	$[Xe]4f^{13}6s^2$	$[Xe]4f^{12}$
Ytterbium	Yb	70	$[Xe]4f^{14}6s^2$	$[Xe]4f^{13}$
Lutetium	Lu	71	$[Xe]4f^{14}5d6s^2$	$[Xe]4f^{14}$

Table 1.1 Electronic structure of lanthanide elements and 3+ ions. [4]

First and foremost, it is necessary to recall that in a many electron system, the separation of energy levels becomes increasingly small. To get from the 1s energy level to the 2s energy level, much more energy is required than to get from 4s to 5s. This is a necessity in quantum mechanics: energy levels must approach a continuum as we approach a bulk system. For the lanthanide elements, this means that the energy required to get from the ground state 4f energy level to the excited 5d state is not very high. In fact, for systems such as cerium at room temperature, electrons spend a statistically significant amount of time in both the 5d and 4f energy levels (referred to as a fluctuating valency [5]).

Second, it is necessary to remember that the 4f energy level is largely internalized within the fully occupied 5s and 5p energy levels present from the "core" xenon electronic structure. This is best portrayed visually (Figure 1.3). In essence, only a small fraction of the f-subshell electrons spend any significant amount of time as valence electrons. Since the electrons spend most of their time internalized within the fully occupied 5s and 5p subshells making up the xenon core, these electrons are largely not available for ionic or covalent bonding.

Third, the interplay of electron penetration and shielding has to be considered. Even though the f-subshell electrons are largely internalized, there is a reasonable chance that an electron may be found outside the xenon core and can be removed. However, once an electron is removed from an f-orbital, the remaining electrons will be pulled considerably tighter to the positive nucleus.
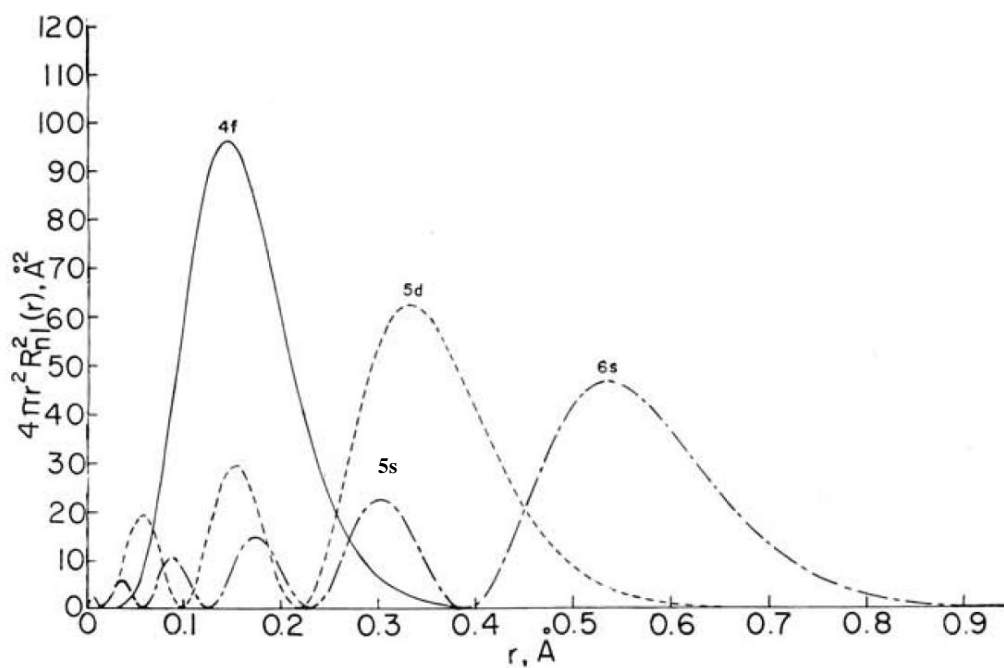
Figure 1.3 Radial distribution function of the subshells. Note that although the 4f subshell is higher energy than the filled 5p subshell of the xenon core, the orbitals penetrate much closer to the nucleus. Reprinted (adapted) with permission from reference[6]. Copyright 1964 American Chemical Society.

This decrease in ionic radius is considerable because electrons at lower energy levels closer to the nucleus shield electrons: electrons at the same energy level do not appreciably contribute to shielding. The lanthanides contain up to 14 electrons at the same 4f energy level where they cannot contribute to shielding one another from the positive nucleus (note, this is also the reason for the famous "lanthanide contraction" causing lutetium to be considerably smaller than cerium). Consequently, removing one f-subshell electron causes the remaining f electrons to move closer to the nucleus, leaving the remaining electrons even more internalized in the xenon core electronic structure, and rendering the remaining electrons unavailable for further chemistry[7]. This is the reason that the lanthanides rarely take an oxidation state higher than +3. Other than lanthanum, the +3 oxidation state does not give the lanthanides a noble gas configuration, but the remaining electrons are not physically available to be removed by chemical means. This results in a stable ion that has both occupied and unoccupied orbitals internal to its electronic structure.

1.3 Sulfur chemistry

Sulfur provides a number of interesting contrasts to the lanthanide elements. For instance, sulfur is one of the oldest known elements, and one that has found use for thousands of years. Originally a valuable commodity mined from volcanic soil, it currently is produced in bulk at high purities as a byproduct of desulfurizing petroleum[8], in contrast to the scarce supply of refined lanthanides. Currently, the largest use for sulfur is for the manufacture of sulfuric acid, with smaller fractions used for fertilizers and metal mining [8], in contrast to the highly specified electronic applications that the lanthanides are used for. Unlike the complex electronic structures of the lanthanide

elements, sulfur has a straightforward configuration of $[Ne]3s^23p^4$. Finally, in contrast to the simple ionic character of the entire lanthanide series, sulfur's chemistry is extremely rich in covalent chemistry.

In elemental form, sulfur needs two additional electrons in order to have a stable argon electron configuration. Unlike oxygen however, sulfur very rarely forms double bonds. In order to complete its octet, sulfur instead tends to form a single bond with two other sulfur atoms, forming covalent rings and chains as a consequence. Consequently, sulfur has a massive amount of allotropes, although the most stable at standard temperature and pressure is the crown shaped, eight sulfur ring (S_8) [9].

Elemental sulfur tends to be quite stable at room temperature and pressure. Consequently, pure sulfur tends to be a very poor sulfurizing agent. In order for elemental S_8 to react with another compound, the sulfur ring must be opened up by breaking one of the sulfur-sulfur bonds, the large 256.6 g/mol molecule must be rearranged for a molecular attack, and a second sulfur-sulfur bond must be broken in order to remove a single sulfur atom from the S_8 molecule. In order to overcome the high activation barrier and steric limitations of using S_8, reactions with pure sulfur tend to occur at high temperatures and in the gas or liquid phase. This is also the reason that, when possible, an alternative sulfurizing agent such as hydrogen sulfide [10] (H_2S), carbon disulfide [11] (CS_2), or thiourea (NH_2CSNH_2) is typically used.

Once sulfur compounds are made, the stability of the compound tends to be determined by the level of covalency of the bonds. For this reason, sulfur compounds with carbon, oxygen, or electron rich transition metals such as gold or silver tend to be very stable. Conversely, ionic sulfide compounds such as those formed from alkaline

earth metals tend to be very unstable. For instance, calcium sulfide readily hydrolyzes water to form calcium hydroxide and H_2S gas and decomposes well before melting by forming calcium carbonate and sulfate[12]. The lanthanide sulfides largely split the difference with stability in water or air, but an autoignition temperature of just 335 °C in air for Ce_2S_3[13].

1.4 The lanthanide sulfides

Lanthanide sulfides have been prepared for every lanthanide element with the exception of promethium[10-11]. Every lanthanide is most stable as an Ln_2S_3 sesquisulfide compound as sulfur lacks the oxidizing power to maintain a +4 oxidation state. However, +2 valent lanthanide monosulfides have been reported for samarium [14], lanthanum [15], europium, and ytterbium [16] with varying degrees of stability. The Ln_2S_3 compounds all adopt one of five distinct crystal structures with the structure adopted dependent primarily on ionic radius and annealing temperature. By convention, these five crystal structures are referred to as the α, β, γ, δ, and ε phases (Figure 1.4).

In general, the α-phase sesquisulfide is the preferred structure for the lighter lanthanides. This structure is an orthorhombic system with a space group of Pnma (62). The nearest neighbor distances in this structure is consistently over three angstroms, making sulfur sulfur single bonds unlikely. Instead, the nearest neighbors for the lanthanides are sulfur atoms, just with complex symmetry common for lanthanide systems.

The β-phase sesquisulfides are, technically speaking, misnamed. Originally characterized as a phase of Ln_2S_3, it was later discovered to be an impurity phase with the formula $Ln_{10}S_{14}O$. An oxygen impurity of less than ten percent is difficult to detect with

most common elemental analysis techniques, which is the reason for the structure originally being assumed to be a pure sulfide. However, the β-phase is a very common structure for the lanthanides, being the thermodynamically preferred at elevated temperatures compared to the alpha phase (1100 °C for Ce_2S_3 [17]). The crystal structure for the beta phase is a very low symmetry tetragonal system with space group I41/acd (142).

For the lighter lanthanides (z<67), the γ-phase sesquisulfide is the last form they are able to take. The gamma phase is a rather complex cubic structure with a space group of I-43d (220). The γ phase is actually a modified Th_3P_4 structure with a decreased Ln site occupancy. Consequently, the formula for this phase is also written as the $Ln_{2.67}S_4$ phase.

The δ and ε phases are primarily found with the heaviest lanthanides (holmium and above). The δ-phase is a very low symmetry monoclinic system with the space group P21/m (11). The ε-phase is a hexagonal system with the space group P63cm (185). As these systems only are found in the heaviest lanthanides, these systems are not further explored in this dissertation.

Finally, there are also mixed valency systems for lanthanide sulfides. The most important of these are the Ln_3S_4 compounds, composed of a mixture of 2+ and 3+ valent lanthanides. This system also takes the Th_3P_4 structure, similar to the γ-phase, but with a full lanthanide site occupancy. Consequently, Ln_3S_4 materials and γ-Ln_2S_3 materials make excellent solid solutions with properties somewhat tunable based on lanthanide atom site occupancy and valency state.
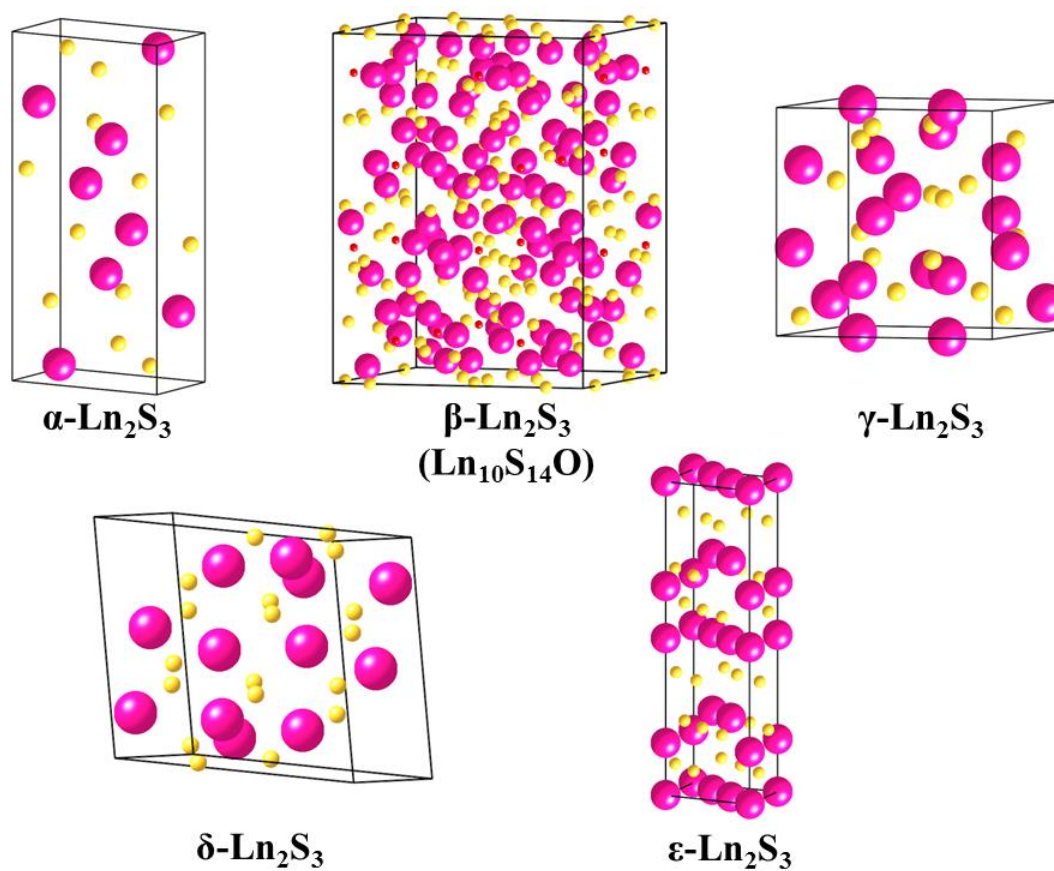
Figure 1.4 Unit cells of the five crystal structures of lanthanide sesquisulfides. Pink atoms are lanthanides, yellow is sulfur. Atoms in models are not drawn to scale between structures. Graphics prepared by CrystalMaker® using crystallographic data from ICDD.

1.5 Semiconductors

Of course, ionic and covalent bonds a predominantly discussed with regards to molecules. When dealing with solids, we really need to extend from the order of quantum mechanics and molecular orbitals into band theory. Doing so allows us to extend some of our chemical insights into the realm of bulk properties, which is ultimately what we care about. As this dissertation is primarily concerned with the synthesis and chemical insights for lanthanide solids, rather than developing the field of solid state physics, a hand waving approach to band diagrams pioneered by Roald Hoffmann will be utilized[18]. Consequently, this thesis is more concerned with the chemistry of lanthanides rather than the details for computing the band diagram structures.

At its most basic, quantum mechanics tells us that there are multiple energy levels for the electrons in an atom to occupy, and these levels are discrete quantized values. However, these quantized states are for each atom. Once we form a molecule, we bring the orbital states from each atom and find where the new molecular orbitals are formed. Consequently, we end up with the same total number of molecular orbitals as the total number of atomic orbitals. As we form bonding molecular orbitals, we also form anti-bonding molecular orbitals, and the stability of the resulting molecule can be predicted depending on where the highest occupied molecular orbital (homo) and lowest unoccupied molecular orbital (lumo) are. This same process occurs as we form a solid, but now we are dealing with moles of molecular orbitals. Consequently, instead of dealing with discrete energy states, we are now dealing with continuous bands of energy states.
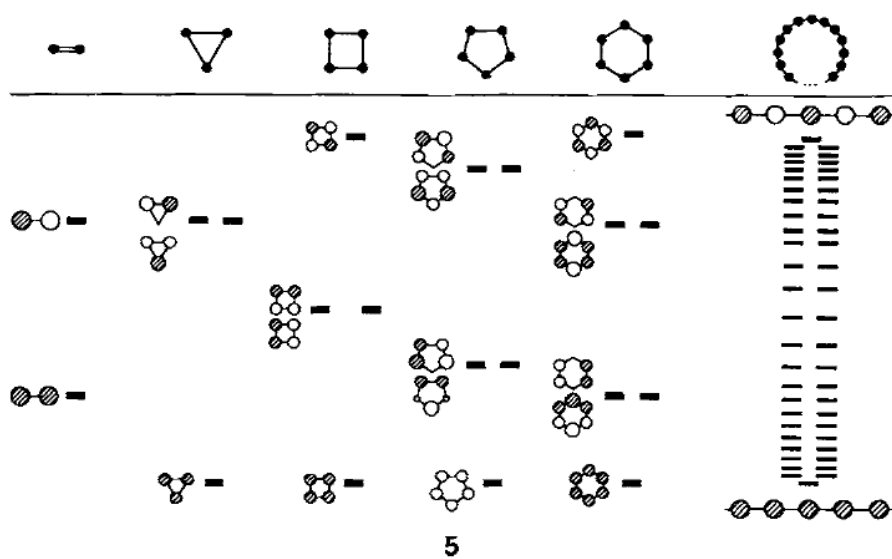
Figure 1.5 Progression from molecular orbitals quantized energy states towards bands of energy states as the number of atoms increases. [18]

Just as the properties of a molecule are described by the position of molecular orbital states as well as the location of HOMO and LUMO, the properties of a solid are described by the band structure and the location of the Fermi level. In a molecule, the stability of the molecular orbitals are determined by the wave functions of the individual orbitals with constructive interference resulting in a lower energy (bonding) molecular orbital and destructive interference resulting in a high energy (antibonding) molecular orbital. For a particularly stable molecule to form, the electrons in the molecule should occupy the bonding orbitals while the anti-bonding orbitals are left unoccupied by electrons. What this means then is that there are specific locations that the electrons prefer to be that result in a lower energy system. However, if we add an additional electron or two (raise the HOMO level), those electrons are forced into unoccupied antibonding orbitals, and these high-energy electrons are unstable and able to be moved around to a lower energy location. Equivalently, if the electrons are highly localized in a solid, there is a wide energy gap between the occupied valence band, and the unoccupied conduction band. This gap in between the valence and conduction bands is the band gap. For a solid in which the electrons are very localized (common for very ionic compounds), we expect to find a large band gap, while a solid with very delocalized electrons (common for metal bonding) is expected to have a very small or no band gap. As sulfur is an electronegative element that generally bonds covalently, sulfide compounds tend to only have somewhat localized electrons – metal sulfides are typically semiconductors with moderate band gaps.

One last important background detail, bonding and antibonding orbitals are assigned symmetrically. For a stable compound then, the low energy bonding orbitals are

normally filled and the high-energy orbitals are empty. Put in context of bands, the Fermi level then is typically halfway between the valence and conduction bands for a pure stable material and the electrons are in a localized arrangement. In order to delocalize the electrons (and improve conductivity), we would need to add extra electrons (which would occupy high energy antibonding orbitals) or remove electrons (add holes) to lower the HOMO level. In a solid, this is achieved by doping the material with elements that can adopt the same bonding arrangement, but that bring either too many or too few electrons compared to the host crystal. Just as doing so in a molecule would move the HOMO level, in a solid this results in the Fermi level being moved such as there are unoccupied bands located close by. A heavily doped semiconductor then would result in considerable overlap of energy states available near the Fermi level offering metal like conductivities, and is classified as a degenerate semiconductor[19].

1.6 Focus of the sulfide section of this dissertation

The sulfide section of this dissertation focuses on the semiconductor characteristics of select lanthanide sulfides along with the synthesis and characterization of α-Sm_2S_3. As lanthanide elements contain unpaired electrons and empty orbitals near but not at the HOMO level, we would expect to find some differences in their band structure compared to transition metal semiconductors. The band structures of the relatively straightforward LnS and Ln_3S_4 compounds of lanthanum, samarium, and gadolinium are interpreted in Chapter 2. Chapter 3 focuses exclusively on the synthesis, characterization, and band structure of α-phase samarium sesquisulfide prepared by chemical vapor deposition. This method is an improvement on previous methods used for preparing α-phase lanthanum sulfides as it very rapidly generates textured thin films from

lanthanide salts using elemental sulfur instead of the hours or days of sulfurizing lanthanide oxides using conventional H_2S methods. It is found both by the DFT calculations and experimentally that the incomplete lanthanide orbitals near the HOMO levels result in metal like materials with a nearby band gap above or below the Fermi level, or put another way, like extremely degenerate semiconductors.

1.7 References

1.   Cerium and cerium compounds. In *Ullmann's Enc. of Industrial Chem.*, 5 ed.; Elvers, B.; Hawkins, S.; Russey, W.; Schulz, G., Eds. John Wiley & Sons: NY, 2004; Vol. 5.

2.   Cerium Mischmetal, alloys, and compounds. In *Ullmann's Enc. of Industrial Chem.*, John Wiley and Sons: NY, 1986; Vol. A6, p 139.

3.   Haxel, G. B.; Hedrick, J. B.; Orris, G. J. *Rare Earth Elements-Critical Resources for High Technology*; U.S. Geological Survey: 2002.

4.   Cotton, F. A.; Wilkinson, G., *Advanced Inorganic Chemistry*. second ed.; Interscience Publishers: New York, 1966.

5.   Lawrence, J. M.; Riseborough, P. S.; Parks, R. D., Valence fluctuation phenomena. *Reports on Progress in Physics* **1981,** *44* (1), 1-84.

6.   Friedman Jr, H. G.; Choppin, G. R.; Feuerbacher, D. G., The Shapes of the f Orbitals. *Journal of Chemical Education* **1964,** *41* (7), 354-358.

7.   Lanthanide Chemistry and Electronic Configuration. http://students.open.ac.uk/omresources/periodictable/ellaac/core.pdf.

8.   Ober, J. A. *Sulfur*; U. S. Geological Survey: 2006.

9.   (a) Meyer, B., Elemental Sulfur. *Chemical Reviews* **1976,** *76* (3), 367-388; (b) Schmidt, M., Elemental Sulfur- A Challenge to Theory and Practice. *Angew. Chem. Internat. Edit.* **1973,** *12* (6), 445-455.

10.   Forster, C. M., White, W. B., Optical absorption edge in rare earth sesquisulfides. *Materials Research Bulletin* **2005,** *41*, 448-454.

11.   Yuan, H., Zhang, J., Yu, R., Su, Q., Synthesis of Rare Earth Sulfides and their UV-vis Absorption Spectra. *Journal of Rare Earths* **2009,** *27* (2), 308-311.

12.   Garcia-Calzada, M.; Marban, G.; Fuertes, A. B., Decomposition of CaS particles at ambient conditions. *Chemical Engineering Science* **2000,** *55*, 1661-1674.

13.   *Cerium Sulphide*; National Occupational Health and Sefety Commission: Camperdown, Australia, 1998.

14.   Meyer, G.; Morss, L. R., *Synthesis of lanthanide and actinide compounds*. Luwer Academic Publishers: Norwell, 1991.

15.   Fairchild, S.; Cahay, M.; Murray, P. T.; Grazulis, L.; Wu, X.; Poitras, D.; Lockwood, D. J., Grain size, texture, and crystallinity in lanthanum monosulfide thin films grown by pulsed laser deposition. *Thin Solid Films* **2012,** *524*, 166-172.

16.   Didchenko, R., Gortsema, F. P., Some electric and magnetic properties of rare earth monosulfides and nitrides. *Journal of Physics and Chemistry of Solids* **1963,** *24* (7), 863-870.

17.   Moffatt, W. G., *The Handbook of Binary Phase Diagrams*. General Electric: Schenectady, NY, 1981; Vol. 2.

18.   Hoffmann, R., How Chemistry and Physics Meet in the Solid State. *Angew. Chem. Int. Ed. Engl.* **1987,** *26*, 846-878.

19.   (a) Kittel, C., *Introduction to Solid State Physics*. 8th ed.; John Wiley & Sons: Hoboken, NJ, 2005; (b) Ziman, J. M., *Principles of the Theory of Solids*. Cambridge at the University Press: NY, 1972.

Chapter 2

ELECTRONIC STRUCTURES OF LANTHANUM, SAMARIUM, AND GADOLINIUM SULFIDES

2.1 Introduction

Chalcogenide based semiconductors are a broad class of materials which display a wide variety of useful electronic properties. For example, copper indium gallium selenides and cadmium tellurides are widely used in photovoltaics for power generation, [1] and bismuth tellurides are widely used for thermoelectric devices [2]. Additionally, while not as common as III-V semiconductor lasers such as gallium arsenide, zinc selenides have been used for lasing applications [3]. Moreover, cadmium tellurides, selenides, and sulfides are widely used for tunable fluorescent dyes (quantum dots) for medical research and diagnostics [4].

In the interest of extending the library of chalcogenide materials available for electronic applications, we have investigated the band structure and the partial density of states for three lanthanide sulfide systems. The lanthanide sulfides (Ln_xS_y) are a class of chalcogenides composed of a lanthanide cation ($^{57}La - {}^{71}Lu$) and the anion sulfur. Sulfur is, by convention, considered as the simplest chalcogen anion due to its similarities with selenium and tellurium and dissimilarity with oxygen. Although lanthanide cations tend to prefer to take a 3+ oxidation state, several lanthanides are known to additionally take a 2+ oxidation state, for instance, as in monosulfide (LnS) or mixed valence (Ln_3S_4)

structures. Generally, La through Sm can most easily take the Ln_3S_4 mixed valence

structure, while Gd through Dy are capable of taking this structure with S and Se, but not

with Te [5]. It is important to note that although the Ln_3S_4 structure is nominally mixed

valency, each Ln atom is crystallographically equivalent in this structure. More exotic is

the lanthanide monosulfide (LnS) structure, in which the rare earth cations are entirely in

the 2+ state. Of the lanthanide monosulfides, samarium monosulfide (SmS) has received

by far the most attention. SmS was discovered as far back as 1956 [6], and is notable for the

presence of a semiconducting low pressure phase and a metallic high pressure phase [7].

More recently, lanthanum monosulfide (LaS) has received increased attention due to its

metallic properties and low work function, potentially making it suitable for use as a cold

cathode material [8]. However, difficulty in preparing high quality lanthanide sulfide

samples with controlled stoichiometry and high crystallinity have limited the

understanding and electronic applications of this class of chalcogenides. Consequently,

several authors have recommended using high quality band structure calculations to

enable a better understanding of the electronic structures of lanthanide sulfides [9].

In order to rectify the lack of high quality data on the lanthanide sulfides, we have

applied density functional theory (DFT) to predict the electronic structures of two

specific crystal systems with varying sulfide content: the LnS structure and the Ln_3S_4

structure. Additionally, calculations with the lanthanide sulfides are very time-consuming

to calculate, because of the need to take into account the effect of the *f*-shell electrons in

these many atom unit cells. Thus, we have limited our study to three lanthanide group

elements: lanthanum, samarium, and gadolinium.

2.2 Theory and calculations

We applied density functional theory implemented in the CASTEP code [10]to calculate the band diagram and density of states of two lattice structures of lanthanide sulfides (LnS and Ln_3S_4) for three lanthanides (Ln = La, Sm and Gd). Spin-polarization was considered in the computation because both Sm and Gd have unpaired spins in these structures. The unit cell of ideal LnS adopts the NaCl structure with space group Fm-3m (#225) symmetry. The lattice parameters for LaS, SmS and GdS were obtained from the International Centre for Diffraction Data (ICDD) and are $a = 5.854$ Å, $a = 5.970$ Å, and $a = 5.562$ Å, respectively. The unit cell of ideal Ln_3S_4 adopts the cubic symmetry with space group I-43d (#220). The lattice parameters for Ln_3S_4 were also obtained from the ICDD, and are: La_3S_4 ($a = 8.73$ Å), Sm_3S_4 ($a = 8.556$ Å), and Gd_3S_4 ($a = 8.378$ Å). Both crystal structures are illustrated in Figure 2.1. The LnS structure is a simple rock salt cubic structure. The Ln_3S_4 structure is considerably more complex, while still remaining cubic. This structure, prototyped by Th_3P_4, is a non-centrosymmetric body centered cubic system with the space group I-43d. In this structure, there are 18 lanthanide cations in each unit cell, with two located in each face along a diagonal glide plane, and the remaining 6 making up a distorted octahedron contained within the unit cell [11]. In spite of its complex appearance, the entire structure is composed of a single unique cation Wyckoff site and a single unique anion site.

The plane wave basis set was utilized together with the generalized gradient approximation (GGA), and Perdew-Burke-Ernzerhof (PBE) exchange and correlation functional [12]. An energy cutoff of 380 eV was applied to the planewave basis set and ultra-soft pseudopotentials were employed with the valence electron configurations as

$5s^25p^65d^16s^2$, $4f^75s^25p^65d^16s^2$, and $4f^65s^25p^66s^2$ for La, Gd, and Sm atoms, respectively. Brillouin zone integrations were performed with a Monkhorst-pack of 7×7×7 k points for the LnS structures, while 5×5×5 k points were used for the Ln_3S_4 structures. A Gaussian broadening was applied with a smearing width of 0.1 eV. The DFT+U method was used for the corrections of on-site coulomb interactions with U = 6 eV [11, 13] for the *f*-electrons of Sm and Gd. Moreover, the ensemble density functional theory (EDFT) [14] scheme programmed in CASTEP was used to overcome the convergence problem inherent in *f*-electron systems.
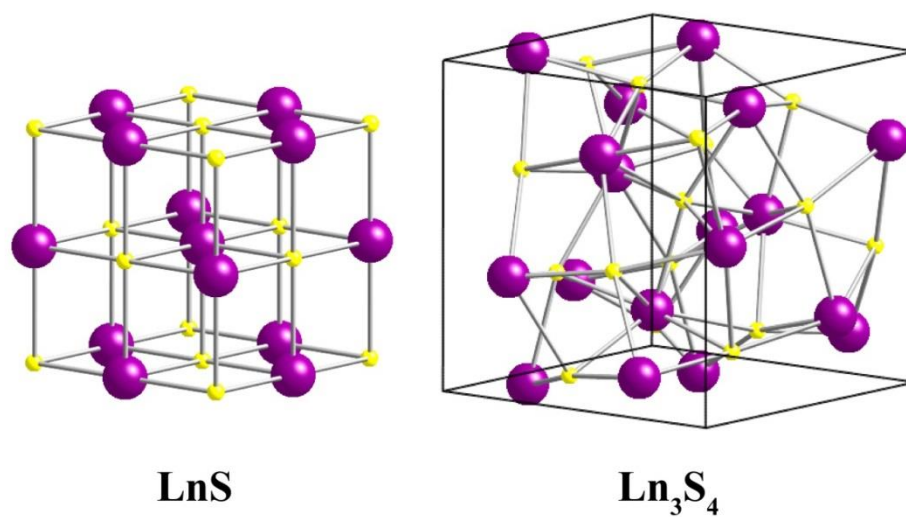
LnS   **Ln₃S₄**

Figure 2.1 Unit cells of two lanthanide sulfides: (left) LnS and (right) Ln_3S_4 (Ln = La, Sm and Gd).

2.3 Results and discussion

As the simplest lanthanide element, lanthanum serves as a natural place to start the discussion of the lanthanide sulfides, even though the electronic structure of LaS does exist in the literature [15]. Lanthanum takes a unique spot in the lanthanide series because it contains no f-shell electrons in its electronic structure of $[Xe]5d^1 6s^2$ [16], which greatly simplifies the electronic structure calculations for lanthanide sulfides. Additionally, the electronic structure of La_3S_4 generated considerable interest in the past due to its conducting to superconducting transition temperature at 7.2 K [17]. As shown in Figure 2.2, both LaS and La_3S_4 are expected to behave as a metal due to occupied bands overlapping the Fermi level (shown as 0 eV in our figures). More specifically, LaS is predicted to be a semimetal due to lower occupancy at the Fermi level with large density of states above and below. This indeed is consistent with the experimentally determined properties of LaS [8, 18] and with previous calculations which made use of a full-potential linear muffin-tin orbital (LMTO) method for computing the band structure [15]. Similarly, La_3S_4 is predicted to be a metal. Although again there is a gap in energy bands less than 1 eV below the Fermi level, the calculated band structure of La_3S_4 has a high occupancy of *d*-orbitals at the Fermi level visible in the partial density of states (pDOS) (Figure 2.2). This is consistent with previously published experimental and computation results [17].
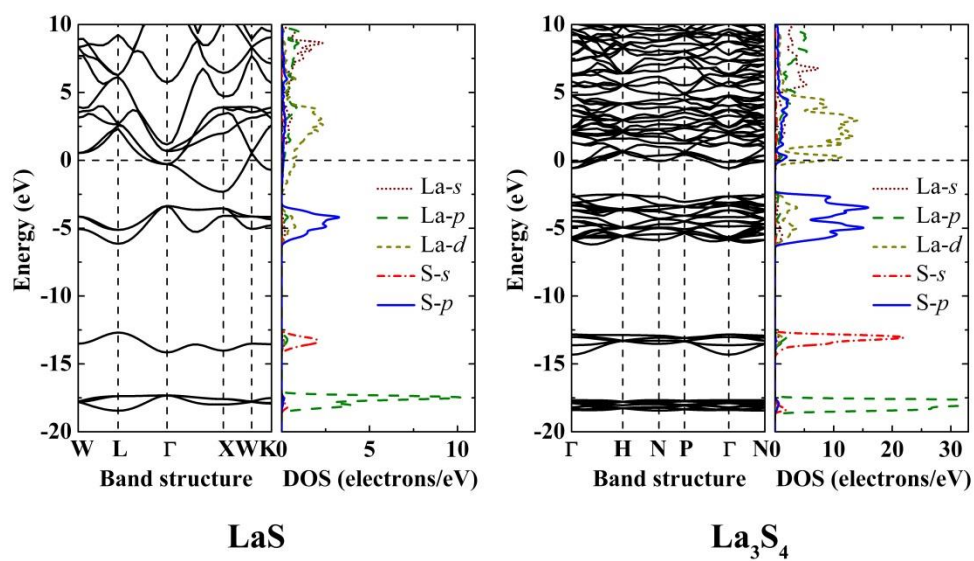
Figure 2.2 Band diagram and density of states of lanthanum sulfides: (left) LaS and (right) La_3S_4. The Fermi level is indicated by the dashed lines.

Samarium is typically believed to take the electronic structure $[Xe]4f^6 6s^2$ [16].

Unlike LaS, SmS is reported to be a narrow band gap semiconductor at atmospheric

pressure and ambient temperature, but with a unique ability to switch to a metallic state at

a moderately low pressure of 6.5 kbar [7]. Just as in the case of LaS, older LMTO methods

were applied to simulate the band structure of SmS [19]. Our results, as shown in Figure

2.3, indicate SmS to be a narrow indirect band gap semiconductor with a gap of about 1

eV. This result corroborates with the observed semiconductor behavior of SmS, although

it does differ from the experimental band gap of 0.15 eV [7]. Still, our calculation is an

improvement from previous simulation results. Earlier work using a LMTO method

predicted metallic behavior for SmS, and was forced to change the unit cell to 1.05 times

the experimental values in order to introduce semiconductor behavior [19]. However, we

have no reasons to doubt previous findings that a decrease in unit cell parameters (such as

from high pressure) would force a narrowing of the band gap and reintroduce metallic
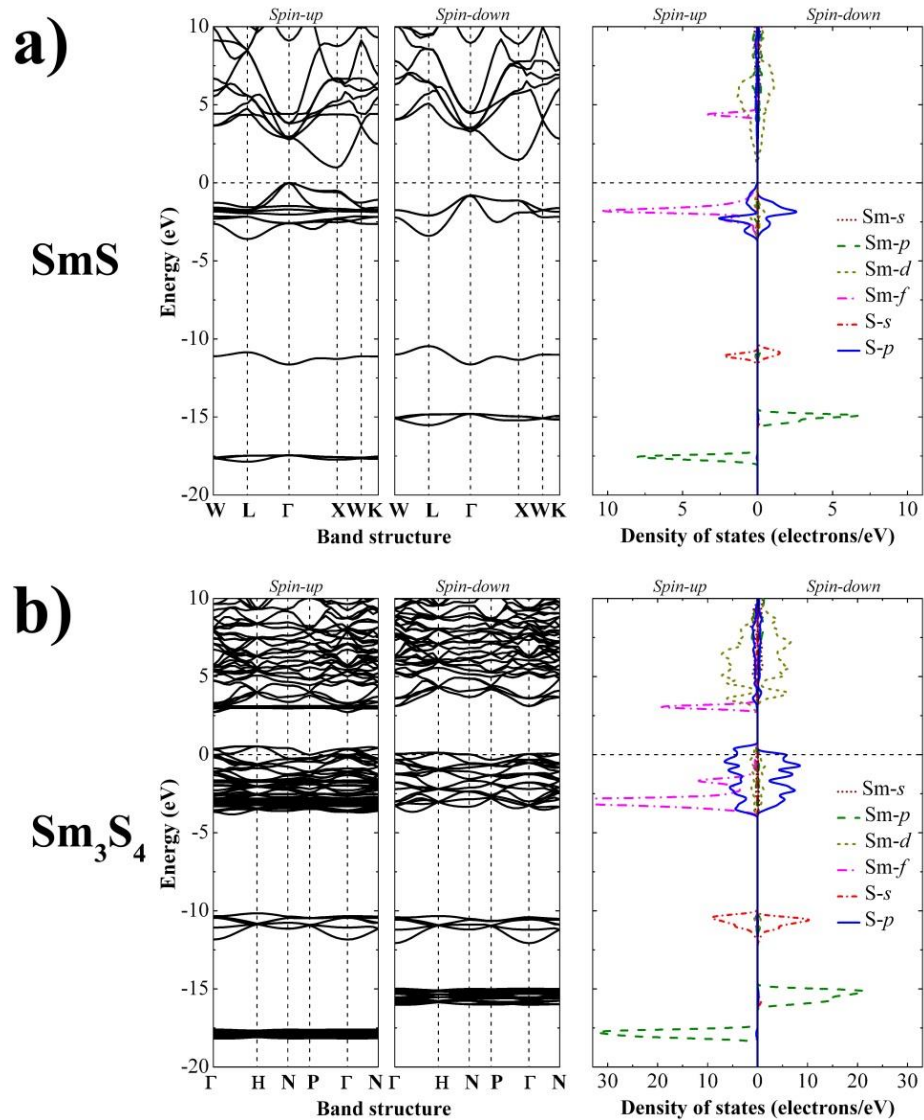
character to the system.

Figure 2.3 Band diagram and density of states of samarium sulfides: (a) SmS and (b) Sm_3S_4. The Fermi level is indicated by the dashed lines.

The electronic structure for Sm_3S_4, as shown in Figure 2.3, is in many ways the most surprising result of our calculations. Unlike the other systems, Sm_3S_4 has a large 2.1 eV band gap above the Fermi level. However, unlike in a well-behaved semiconductor, the Fermi level is not located in between the band gap. Instead, the Fermi level is 0.6 eV below the edge of the bottom bands, suggesting that technically Sm_3S_4 is a metal, but the large band gap's presence gives Sm_3S_4 character similar to that of an extremely degenerate semiconductor. Surprisingly, this result is consistent with the observed properties of experimental Sm_3S_4 samples. It was found that Sm_3S_4's extinction coefficient trails off rapidly for photon energies below 2 eV (similar to a semiconductor with a 2 eV band gap) but remains appreciable all the way down to 0 eV (similar to a metal) [20]. Additionally, this is similar to the behavior of other samarium sulfides such as alpha phase Sm_2S_3 [21].

Unlike the simple case for lanthanum, gadolinium is expected to take the electronic structure of $[Xe]4f^7 5d^1 6s^2$ [16]. However, similar to LaS, our calculation predicted gadolinium monosulfide (GdS) to be a semimetal with occupied d-orbitals present at the Fermi level (Figure 2.4).
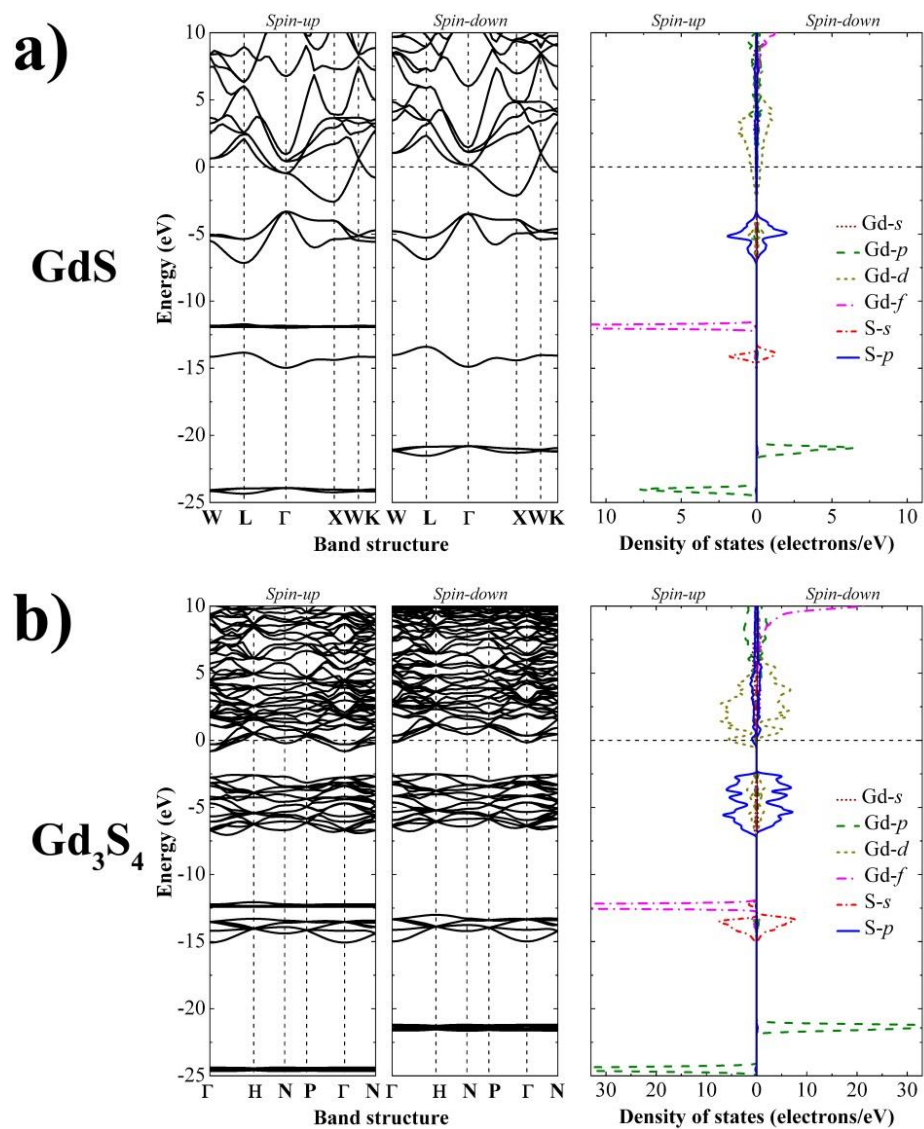
Figure 2.4 Band diagrams and density of states of gadolinium sulfides: (a) GdS and (b) Gd$_3$S$_4$. The Fermi level is indicated by the dashed lines.

Additionally, just as in the case of La_3S_4, Gd_3S_4 is a semimetal with a wide gap in energy states extending from less than 1 eV below the Fermi level to several eVs below. The partial density of states for the gadolinium sulfides provides some clues for this similarity in electronic structure with those of the lanthanide sulfides: their occupied *f*-orbitals are at considerably lower energy levels than in the case of samarium (~ -12 eV for both gadolinium sulfides). This is likely a consequence of Gd containing a completely half-filled *f*-shell, which lowers the energy levels of these orbitals. These results are in excellent agreement with the theoretical band structure of GdS and Gd_3S_4 conjectured from electron energy loss and photoemission spectroscopy experiments [22].

2.4 Conclusions

Band structures and partial density of states have been calculated for LaS, La_3S_4, SmS, Sm_3S_4, GdS, and Gd_3S_4 using a DFT+U approach. To the best of our knowledge, this is the first time that this approach has been applied to most of these studied systems. Additionally, our calculation results have good correlation with existing experimental measurements for these systems. LaS, La_3S_4, GdS, and Gd_3S_4 are predicted to be semimetals. While SmS is predicted to be an indirect gap semiconductor, Sm_3S_4 is expected to behave similarly to a heavily degenerate semiconductor. To improve the predictions of our computation method for other lanthanide systems where reliable *f*-orbital electronic contributions must be considered, further experimental measurement are needed to obtain a better estimation of the correction factor, U, for the on-site coulomb interactions.

2.5 References

1.   Parida, B.; Iniyan, S.; Goic, R., A review of solar photovoltaic technologies. *Renewable and Sustainable Energy Reviews* **2011,** *15*, 1625-1636.

2.   Dughaish, Z. H., Lead telluride as a thermoelectric material for thermoelectric power generation. *Physica B* **2002,** *322*, 205-223.

3.   Jeon, H.; Ding, J.; Patterson, W.; Nurmikko, A. V.; Xie, W.; Grillo, D. C.; Kobayashi, M.; Gunshor, R. L., Blue-green injection laser diodes in (Zn, Cd)Se/ZnSe quantum wells. *Applied Physics Letters* **1991,** *59*, 3619-3621.

4.   Hardman, R., A Toxicologic Review of Quantum Dots: Toxicity Depends on Physicochemical and Environmental Factors. *Environmental Health Perspectives* **2006,** *114* (2), 165-172.

5.   Beaudry, B. J.; Gschneidner, K. A., Rare Earth Compounds. In *CRC Handbook for Thermoelectrics*, Rowe, D. M., Ed. 1995; p 701.

6.   Meyer, G.; Morss, L. R., *Synthesis of lanthanide and actinide compounds*. Luwer Academic Publishers: Norwell, 1991.

7.   Batlogg, B.; Kaldis, E.; Schlegel, A.; Wachter, P., Electronic structure of Sm monochalcogenides. *Physical review b* **1976,** *14* (12), 5503.

8.   Fairchild, S.; Cahay, M.; Murray, P. T.; Grazulis, L.; Wu, X.; Poitras, D.; Lockwood, D. J., Grain size, texture, and crystallinity in lanthanum monosulfide thin films grown by pulsed laser deposition. *Thin Solid Films* **2012,** *524*, 166-172.

9.   Witz, C.; Huhuenin, D.; Lafait, J.; Dupont, S.; Theye, M. L., Comparative optical studies of Ce_2S_3 and Gd_2S_3 compounds. *Journal of Applied Physics* **1996,** *79* (4), 2038-2042.

10.   Segall, M. D.; Philip, J. D. L.; Probert, M. J.; Pickard, C. J.; Hasnip, P. J.; Clark, S. J.; Payne, M. C., First-principles simulation: ideas, illustrations and the CASTEP code. *Journal of Physics: Condens. Matter* **2002,** *14*, 2717-2744.

11.   Holtzberg, F.; Methfessel, S., Rare-Earth Compounds with the Th_3P_4-Type Structure. *Journal of Applied Physics* **1966,** *37* (3), 1433-1435.

12.   Perdew, J. P.; Burke, K.; Ernzerhof, M., Generalized Gradient Approximation Made Simple. *Phys. Rev. Lett.* **1996,** *77*, 3865-3868.

13.   Petersen, M.; Hafner, J.; Marsman, M., Structural, electronic and magnetic properties of Gd investigated by DFT+U methods: bulk, clean and H-covered (0001) surfaces. *Journal of Physics: Condensed Matter* **2006,** *18*, 7021-7043.

14.   (a) Marzari, N.; Vanderbilt, D.; Payne, M. C., Ensemble Density-Functional Theory for Ab Initio Molecular Dynamics of Metals and Finite-Temperature Insulators. *Phys. Rev. Lett.* **1997,** *79*, 1337-1340; (b) Payne, M. C.; Teter, M. P.; Allan, D. C.; Arias, T. A.; Joannopoulos, J. D., Iterative minimization techniques for ab initio total-energy calculations: molecular dynamics and conjugate gradients. *Rev. Mod. Phys.* **1992,** *64*, 1045-1097.

15.   Eriksson, O.; Wills, J.; Mumford, P.; Cahay, M.; Friz, W., Electronic structure of the LaS surface and LaS/CdS interface. *Physical Review B* **1998,** *57* (7), 4067-4072.

16.   Cotton, F. A.; Wilkinson, G., *Advanced Inorganic Chemistry*. second ed.; Interscience Publishers: New York, 1966.

17.   Shim, J. H.; Kim, K.; Min, B. I.; Kang, J.-S., Electronic structures of La_3S_4 and Ce_3S_4. *Physica B* **2002,** *328* (1-2), 148-150.

18.   Cahay, M.; Boolchand, P.; Fairchild, S. B.; Grazulis, L.; Murray, P. T.; Back, T. C.; Semet, V.; Binh, V. T.; Wu, X.; Poitras, D.; Lockwood, D. J.; Yu, F.; Kuppa, V., Review Article: Rare-earth monosulfides as durable and efficient cold cathodes. *Journal of Vacuum Science and Technology B* **2011,** *29* (6), 602-1-14.

19.   Strange, P., A band theory description of the valence transition in samarium sulphide. *Physica b+c* **1985,** *130* (1-3), 44-46.

20.   Batlogg, B.; Kaldis, E.; Schlegel, A.; Schulthess, G. v.; Wachter, P., Optical and Electrical Properties of the Mixed Valence Compound Sm_3S_4. *Solid State Communications* **1976,** *19*, 673-676.

21.   Marin, C. M.; Wang, L.; Brewer, J. R.; Mei, W.-N.; Cheung, C. L., Crystalline α-Sm_2S_3 nanowires: Structure and optical properties of an unusual intrinsically degenerate semiconductor. *Journal of Alloys and Compounds* **2013,** *563*, 293-299.

22.   Grazhulis, V. A.; Bozhko, S. I.; Bolotin, I. L.; Bulanov, O. R.; Ionov, A. M., Electronic structure of the valence band of GdS_x and Gd_3S_4. *Applied Surface Science* **1996,** *104/105*, 68-72.

Chapter 3

CRYSTALLINE α-Sm$_2$S$_3$ NANOWIRES: STRUCTURE AND OPTICAL PROPERTIES OF AN UNUSUAL INTRINSICALLY DEGENERATE SEMICONDUCTOR

3.1 Introduction

The lanthanide sulfides are an intriguing class of semiconducting materials that are of considerable interest for their potential as high temperature thermoelectric materials [1], solar energy conversion materials [2], pigments [3], infrared window materials [4], and phosphor host media [5]. These applications largely stem from their visible light range absorption edges which provide the lanthanide series with their wide range of vibrant colors, from bright yellow (Yb$_2$S$_3$), to maroon (Ce$_2$S$_3$), to deep brown (Nd$_2$S$_3$) [6]. Despite their promise in displacing the use of toxic [7] cadmium chalcogenides in pigment applications [3], the lanthanide sulfides have not been utilized in many of the other applications which utilize cadmium chalcogenides, such as photovoltaics [8] and quantum dots [9]. This can be attributed to the time and energy intensive conventional synthetic methods, and, in part, to the unresolved nature of their optical absorption bands.

The lanthanide sulfides are typically synthesized by sulfurizing the corresponding lanthanide oxides [10] using the highly toxic sulfurization agent hydrogen sulfide (H$_2$S). Their reaction temperatures range from 1000 °C to 1200 °C with the actual process temperature depending on the lanthanide involved and the resulting crystal structure

desired [6b]. The major problem associated with this synthetic strategy is the long reaction time required to fully displace the oxygen from the starting oxide reactants: 4-7 days at the peak reaction temperature [6a]. Recently, carbon disulfide (CS_2) has been applied as the sulfurization agent in place of H_2S [6c]. CS_2 was found to be a more rapid sulfurization agent, bringing the sulfurization time down to around 3 hours and the required sulfurization temperatures down to 800-1200 °C [6c]. However, this superior sulfurization performance of CS_2 comes at the cost of a 1-5 at. % carbon incorporation into the resulting lanthanide sulfides [11].

In general, the lanthanides prefer to take a +3 oxidation state, meaning that a sesquisulfide form (Ln_2S_3) is the preferred stoichiometry. Notably, Yb [6a] and Sm [12] may also attain a +2 state, but the +3 state is generally favored. The crystal structures of Ln_2S_3 generally can take one of four polymorphs: α, γ, δ, or ε. Originally, a β-phase had also been reported, but it has since been discarded because a slight amount of oxygen was later found to be required for its formation [13]. Between the fifteen lanthanide elements and four polymorphs, the resulting lanthanide sesquisulfide's absorption band edges can range from 1.56 eV (for γ phase Gd_2S_3) to 2.73 eV (for α phase La_2S_3) [6b].

Beyond the rough absorption edges, little is known about the nature of the semiconducting band gaps involved with the lanthanide sulfides. This is largely due to the dramatic tailing edge (weak absorption occurring before the main absorption onset) observed in the experimental absorption spectra as noted by Glurdzhidze *et al* as far back as 1979 [14]. Typically, this band tailing is considered indicative of a small concentration of impurities in the sample [15]. While Tauc plot analysis of various lanthanide sulfides were attempted as early as 1983 [6a], the optical spectra of these semiconductors routinely failed

to fit well with direct, indirect, or even direct and indirect forbidden models. Indeed, in a more recent study on single crystalline Gd_2S_3 and Ce_2S_3 samples, Witz *et al* [16] could only postulate that some extrinsic sample effects were obfuscating their reflectivity and absorption data. Consequently, they recommended reliable band structure calculations in order to aid with interpreting these compounds' complex optical spectra.

Of the lanthanide sulfides, the samarium sulfide systems are of particular interest for their semiconductor applications. Since samarium exhibits a propensity for taking on both 2+ and 3+ oxidation states, the reported band gaps for the samarium sulfides range from 0.15 eV for SmS [17], to 2.18 eV for the γ-phase of Sm_2S_3 [6b]. Among different phases of samarium sulfides, α-phase Sm_2S_3 attracts an increasing amount of attention [18] due to reported band gaps in the infrared-to-red range, which are comparable to the industrially important cadmium selenide [9a, 19]. Nonetheless, challenges in understanding the electronic structures of α-Sm_2S_3 have severely limited its industrial applications. Specifically, failures in applying the semiconducting models, used for simple *p*- and *d*-block compounds, to explain the reported absorption and reflectance spectra of α-Sm_2S_3 and their band tailing have led to speculations of impure samples in the reported literature and doubts as to the nature of its band gap. Moreover, the wide range of reported α-Sm_2S_3's absorption band edge value, from 1.69 eV [6b] to 1.88 eV [6c] to even as high as 4.02 eV [18], has of yet been unresolved. The study of α-Sm_2S_3 has further been exacerbated by the lack of reliable band structure calculations for the electron dense *f*-block lanthanide sulfides.

Here we report the rapid synthesis of crystalline α-phase Sm_2S_3 by chemical vapor deposition and the characterization of its electronic structure via a combined approach of absorption spectroscopy and first principles calculations. Interestingly, these materials were found to have a high inherent tendency to crystallize as high aspect ratio nanowires with morphologies similar to naturally occurring amphiboles. Absorption spectroscopy of the resulting nanostructured films was taken both to characterize the rough band edge and band gap characteristics. In order to better understand the unexplained band tailing present in the absorption spectra of these materials, first principles density functional theory (DFT) calculations of ideal, Sm or S deficient α-Sm_2S_3 models were applied to compute possible electronic structures of α-Sm_2S_3. Remarkably, our DFT studies reveal that even in an ideal crystalline state, α-Sm_2S_3 behaves as a heavily degenerate semiconductor (i.e. this material is intrinsically degenerate). This finding matches well with the peculiar experimentally observed behavior of these materials, providing explanation, for the first time, for the prominent tailing edges in their optical absorption spectra which have long been reported for these lanthanide sulfide systems.
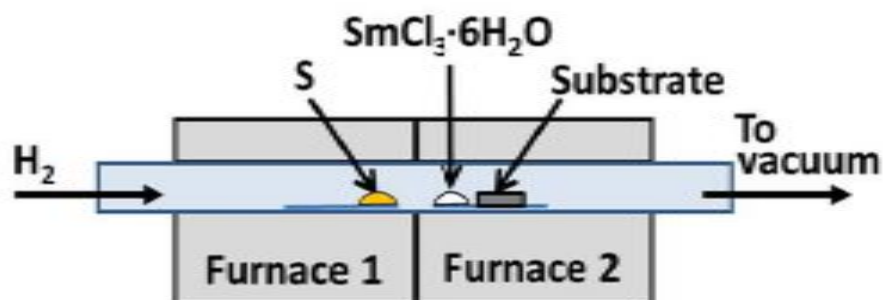
Figure 3.1 Schematic of the experimental setup for the synthesis of α-Sm$_2$S$_3$ nanowire films

3.2 Materials and methods

The α-Sm$_2$S$_3$ nanowire samples were synthesized by a CVD process in a 1-inch diameter quartz tube, inside a dual-furnace reactor. Samarium (III) chloride hexahydrate (SmCl$_3$·6H$_2$O), elemental sulfur (S), and hydrogen (H$_2$) were used as the chemical precursors. (Figure 3.1) The overall empirical reaction equation is proposed as: $2SmCl_3·6H_2O(g) + 3S(g) + 3H_2(g) \rightarrow \alpha$-Sm$_2S_3$(s) + 6HCl (g) + 6H$_2$O (g). 1x1-cm^2 (100) silicon wafers coated with 200-nm thick silicon nitride (University Wafers, South Boston, MA) and 1x1-cm^2 quartz slides were used as the substrates to collect products deposited during the reaction. The silicon nitride coating acted as a diffusion barrier to minimize the formation of silicides on the silicon chips during the reaction. Each substrate was pre-rinsed with ethanol and 18-MΩ de-ionized water, followed by drying with nitrogen before use. The silicon nitride coated substrate was located at 12 cm to the left of the center of the dual furnace. If a quartz substrate was to be coated to collect reaction products for their optical characterization, it was placed adjacent to the silicon nitride coated silicon chip.

In a typical reaction run, 0.1 g of elemental sulfur and 0.3 g of samarium (III) chloride hexahydrate (Sigma-Aldrich, Milwaukee, WI) were loaded on two separate quartz boats at 14 cm to the right of the center of Furnace 1 and at 13.5 cm to the left of the center of Furnace 2, respectively. (Figure 3.1) After the reactor system was pumped down to a base pressure below 9 mTorr, 100 standard cubic centimeters per minute (SCCM) of hydrogen (H$_2$) was applied to purge the quartz-tube in the reactor system. Furnace 1 was then heated to 100 °C over a period of 20 minutes to vaporize the sulfur

and to start the diffusion of sulfur throughout the system. Simultaneously, Furnace 2 was heated to 400 °C to remove the water from the samarium precursor. The flow of the H_2 carrier gas was stopped before Furnace 1 reached 35 °C. After Furnace 1 reached 100 °C and Furnace 2 reached 400 °C, their temperatures were held constant for 10 min. until the reactor pressure re-stabilized. This was then followed by increasing the temperature of Furnace 2 to 875 °C and that of Furnace 1 to 200 °C over a period of ten min. Afterwards, H_2 was re-added to the reaction at 100 SCCM for another 10 min. The typical reaction pressure was at *ca.* 0.6 Torr. At the end of the reaction, the flow of H_2 was stopped. Furnace 1 was opened fully to cool while Furnace 2 was cooled at a rate of over 5 °C/second down to 400 °C before being opened fully for cooling to room temperature.

The morphology and atomic lattice structures of the as-synthesized samples were characterized by field emission scanning electron microscopy (FESEM, Hitachi S-4700, Pleasanton, CA), x-ray powder diffraction (XRD) using a Rigaku D/Max-B Diffractometer (2 kw Cu Kα x-ray beam with an average wavelength of 1.544 Å, Rigaku Americas, Woodlands, TX), and transmission electron microscopy (Tecnai F-20, FEI, Hillsboro, OR) with energy dispersive x-ray spectroscopy (EDX). TEM samples were prepared by sonicating the sulfide coated substrates in ethanol for 1-10 seconds until the ethanol became slightly cloudy, and then drop-casting this solution onto holey carbon TEM grids. UV-Vis-mid-IR absorption spectroscopy was performed on the sulfide coated quartz substrate and evaluated in comparison to a reference quartz standard using a Cary 5000 grating spectrophotometer (Agilent Technologies, Santa Clara, CA). Note that the use of absorption spectroscopy was necessary because the as-synthesized films were determined to be too thin for meaningful diffuse reflectance measurements.

3.3 Theory and calculations

Absorption spectrum analysis was performed using the standard Tauc method [20]. The model behind this method assumes that band to band transitions occur between a concave up and a concave down parabolic band in which the lower band is fully occupied and curved concave down. In such a case, it can be shown [15] that:

$$\alpha \cdot h\nu \propto (h\nu - E_g)^n \qquad [Eq. 1]$$

where α is the coefficient of absorption of the material, $h\nu$ is the energy of the incident photon, and E_g is the energy of the band gap being investigated. Additionally, the value of the exponential n provides insights into the relative positions of the two parabolic bands, where a value of $n=1/2$ corresponds to a direct peak to valley transition between parabolic bands, and a value of $n=2$ corresponds to an indirect transition in which the peak of the valence band is not aligned in k space with valley of the conduction band. Under the assumptions used for Eq. 1, a Tauc plot, featuring (absorbance $\cdot h\nu)^{1/n}$ on the y-axis plotted against photon energy on the x-axis, can be prepared. In such a plot, the value of n which results in a linear graph indicates the nature (direct, indirect, etc.) of the band gap, and the value of the extrapolated x-axis intercept of the linear plot provides the value of E_g.

On the computational side, density functional theory (DFT) implemented in the CASTEP code [21] was applied to calculate the band diagram and density of states of ideal, samarium-deficient, and sulfur-deficient α-Sm_2S_3 lattice models. The unit cell of ideal α-Sm_2S_3 is orthorhombic with space group Pnma (#62) symmetry and lattice parameters a = 7.38 Å, b = 3.97 Å, and c = 15.36 Å containing 8 Sm and 12 S atoms. The plane wave basis set, with an energy cutoff of 380 eV ultra-soft pseudopotential, was employed together with the generalized gradient approximation (GGA), and Perdew-Berke-Ernzerhof (PBE) exchange and correlation functional [22]. The DFT+U method was used for the corrections of on-site coulomb interactions with U = 6 eV for Sm. In addition, we utilized the ensemble density functional theory (EDFT) [23] scheme programmed in CASTEP to overcome the convergence problem inherent in f-electron systems. Furthermore, we constructed two additional models with supercells double the size of the single unit cell (shown in Figure 3.4a and b): one with an S vacancy (i.e. 16 Sm and 23 S atoms), and the other with a Sm vacancy (i.e. 15 Sm and 24 S atoms). This was done in order to simulate the effects of Sm and S deficiencies on the band structure.

3.4 Results and discussion

Typically, the as-synthesized samarium sulfide samples appeared as brownish "felt-like" textured films. FESEM revealed that these films were composed of high aspect ratio wires that often bundled together to form cables of a wide variety of thicknesses and lengths of up to 15 microns. (Figure 3.2a and 2b) Individual wires generally had diameters of 15-30 nm. The product was identified as alpha phase (orthorhombic) samarium sesquisulfide (α-Sm_2S_3) by matching the XRD patterns of these wire-textured

films to the ICDD data (card # 04-007-4140). (Figure 3.2c) While the peak positions in these patterns were strongly indicative of α-Sm_2S_3, the relative intensities of the various indexed peaks varied considerably from sample to sample, indicating a variety of preferred growth alignments. Nonetheless, these diffraction patterns did not appear to show any meaningful amount of samarium oxysulfide contamination. The EDX spectrum of the product obtained under TEM suggested the presence of mainly sulfur and samarium in these wires. (Figure 3.2d) The weak peaks in the spectrum indicating the presence of carbon, copper, and oxygen likely originated from the TEM grid.

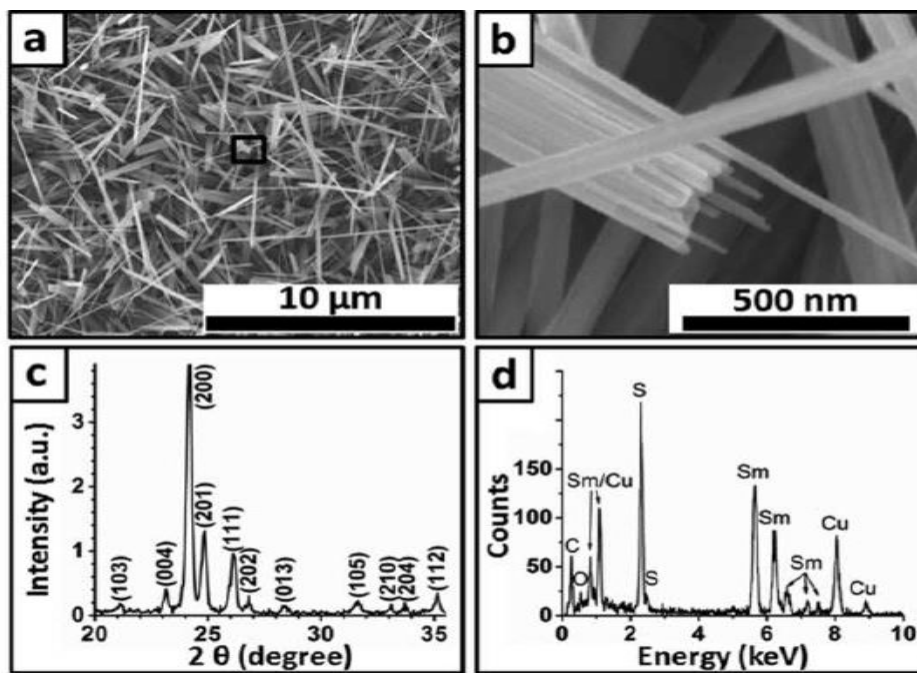**Figure 3.2** (a) Representative SEM image of α-Sm_2S_3 nanowire film on a silicon nitride coated silicon chip. (b) Zoom-in image of the boxed area in Fig. 2a. The imaged wire bundling illustrates the typical morphology of the wires produced in this system. (c) Typical XRD pattern of α-Sm_2S_3 nanostructured films. (d) EDX spectrum of α-Sm_2S_3 nanowires deposited on a holey carbon TEM grid.

High resolution TEM (HRTEM) characterization of the as-synthesized samples provided further insights into the short order crystal structure of the Sm_2S_3 nanowires. (Figure 3.3) Under the TEM, these wires were often terminated by flat or nearly flat ends and were generally found aggregated in a bundle form. Figure 3.3a shows a wire bundle containing more than six obvious wires, each of which had diameters of about 20 nm. Selected area electron diffraction (SAED) obtained at this bundle was complicated due to the beam passing through multiple crystal grains. (Figure 3.3b) Interestingly, diffraction by these bundles often indicated that the crystalline structures of these multiple grains share a common [010] orientation along the length of the wires.

Occasionally, isolated nanowires could be found on the TEM grid, allowing for an un-interfered with study of the material's crystal structure. Figure 3.3c shows the tip of an individual wire of *ca.* 60 nm in diameter with clearly visible vertical grain boundaries. While the very tip of the wire appeared polycrystalline, the nanobeam SAED pattern obtained at the highlighted region (Figure 3.3d) illustrated a much cleaner diffraction pattern than could be obtained from a wire bundle. (Figure 3.3b) High resolution imaging of this region showed atomic lattice columns. (Figure 3.3e) This columnar alignment of atomic lattices is particularly significant since the α-phase lanthanide sesquisulfide crystal structure can only be tilted to show aligned columns when imaged in the [001] or [010] view direction. The simulated [001] view of the α-Sm_2S_3 lattice structure (Figure 3.3f) generated using the CrystalMaker$^{©}$ software (Oxford, England) matched well with the separation spacing among the lattice fringes in our HRTEM zoom-in image. (Figure 3.3e) Similar lattice matching models cannot be obtained in the case of the [010] view.

This finding supports the [010] nanowire growth direction as indicated in Figure 3.3b for the nanowire bundles. The corresponding simulated diffraction pattern in the [001] direction (Figure 3.3g) also matches closely with the actual SAED pattern (Figure 3.3d) taken at the circled area shown in Figure 3.3c. Nonetheless, the left side of Figure 3.3d shows what should be forbidden diffraction spots appear half-way in between the predicted diffraction spot positions. (Figure 3.3g) This likely implies a small break in the crystal symmetry of the sample, permitting otherwise forbidden peaks to appear under the right conditions.
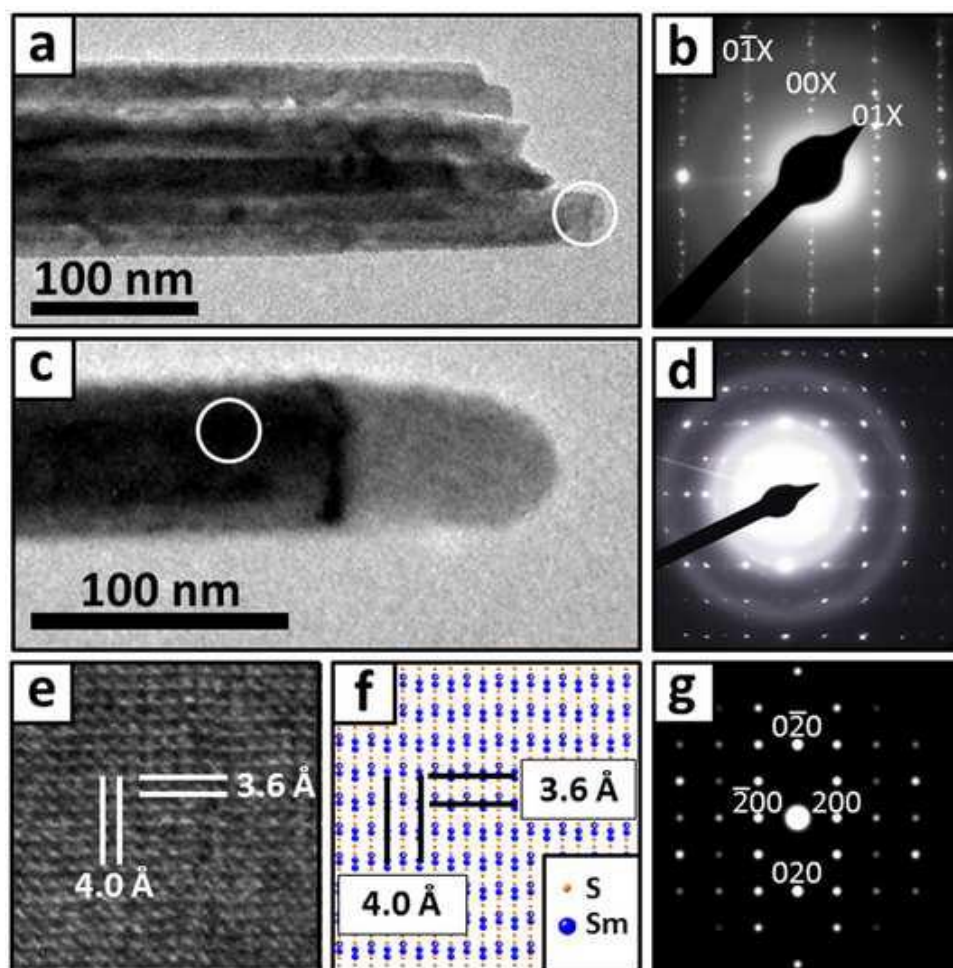
Figure 3.3 (a) TEM image of a typical α-Sm_2S_3 wire bundle. The bundle has a width of 115 nm with an individual wire width of approximately 18 nm. (b) SAED of shown wire bundle taken at the location circled in (a). The parallel lines of the displayed diffraction spots suggest that one axis of orientation is shared amongst the different individual wires in the bundle. (c) TEM image of a separated individual wire. The change in darkness is due to phase contrast and a vertical grain boundary at the tip. (d) SAED of the individual wire at the circled location shown in (c). (e) HRTEM image of the wire shown in (c). (f) Extended CrystalMaker® crystal structure from the [001] view direction. (g) Simulated SAED spectra based on the crystal orientation indicated in (f). Note that this pattern matches well the diffraction spots in the lower right of (d), but this simulated pattern does not account for the weak spots in between the strong spots shown on the left of (d).

To examine the origins of the experimental diffraction spots not explainable with our simulated SAED pattern for an ideal α-Sm_2S_3 lattice, we deliberately introduced either a Sm or S atomic vacancy site in the ideal α-Sm_2S_3 crystal structure model and simulated the resulting SAED patterns. (Figure 3.4) The removal of either a sulfur atom (Figure 3.4a, c, and e) or a samarium atom (Figure 3.4b, d, and f) for every 2 unit cells resulted in almost identical diffraction patterns which showed weak diffraction spots occur half way between each of the spots permitted by the ideal α-Sm_2S_3 crystal structure. Though the removal of one atom for every 40 atoms in a dual-unit cell only constitutes a 2.5% atomic deficiency, such a modification introduced a break in the symmetry and hence caused these normally forbidden diffraction spots to arise. These normally forbidden diffraction spots resulting from the absence of a samarium atom were found to be more intense than those observed in the case of the sulfur atom absent model. (Figure 3.4d versus 3.4c). Our results can be possibly rationalized by noting that the influence of electron diffraction is larger for higher z atoms. Figures 3.4e and 3.4f illustrate that the overlaid simulated SAED patterns fit that of the left side of the experimental diffraction pattern in Figure 3.3d. This implies that a systematic atomic absence of sulfur or samarium was likely present in the region interrogated by part of the probing electron beam. Due to the difference in the intensity of some of the "forbidden" diffraction spots, we suspect that this sample was samarium deficient, at least in the illustrated section of this nanowire.
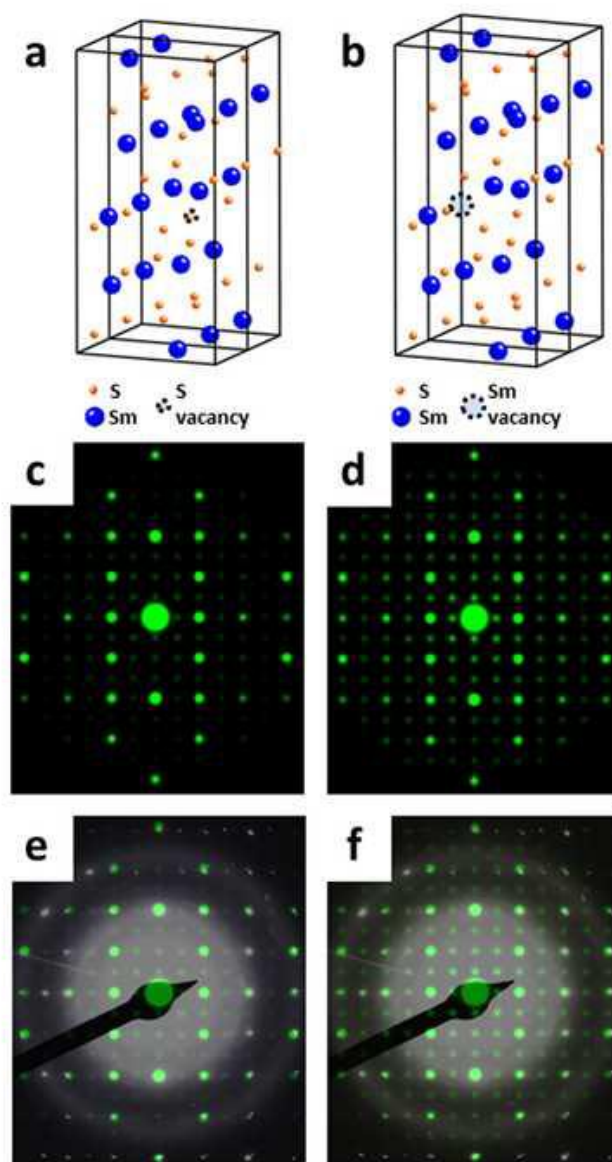
Figure 3.4 Simulated models of α-Sm$_2$S$_3$: (a) model showing the systematic absence of a single samarium atom for every two unit cells. (b) Model showing the absence of a single samarium atom for every two unit cells. (c) Simulated electron diffraction pattern for the model in (a). Note the presence of the faint spots between major spots. (d) Simulated electron diffraction pattern for model (b) under identical conditions as for (c). This pattern is similar to the one in (c) (green) overlaid on the data from Fig. 3d (white). All experimentally observed spots fall under either the normal intense spots or the fainter spots attributed to the missing sulfur atoms in the unit cell. (f) Simulated diffraction pattern in (d) (green) overlaid on the data from Fig. 3d (white). The brighter in between spots better account for the experimental data.

The optical absorption of the as-synthesized α-Sm$_2$S$_3$ nanowire film was evaluated via UV-Vis absorption spectroscopy to determine its band gap characteristics. The absorption band edge of the α-Sm$_2$S$_3$ nanowire film roughly coincided with the previously reported band edge, intercepting at about 700 nm (1.77 eV). [6b] (Figure 3.5a) Optical absorption of the film starts below 2200 nm (0.56 eV) with absorption gradually increasing towards shorter wavelengths. This band tailing phenomenon has been reported before among the absorption spectra of lanthanide sulfides [14, 16]. The largest characteristic *f*-to-*f* transition absorption peaks of samarium sulfide remained observable at 1100, 1270, and 1410 nm, corresponding well to previously reported results for α-Sm$_2$S$_3$ [6b]. To better assess the characteristics of the sample's band gap, we compared two Tauc plots using the absorption data, one assuming a direct band gap model (Equation 1, *n* = 1/2) (Figure 3.5b) and another assuming an indirect band gap model (Equation 1, *n* = 2) [15]. (Figure 3.5c) If we assume that the synthesized α-Sm$_2$S$_3$ nanowire film has a direct band gap, an extrapolated straight line fit of the corresponding Tauc plot would predict a direct band gap of *ca.* 2.4 eV. (Figure 3.5b) As shown in the absorption spectrum, the very large band tailing is once again very apparent in this plot. Indeed, this kind of trailing edge is typically indicative of dopant states present in a pure semiconductor [15]. In contrast, if we assume that the sample has an indirect band gap, the extrapolated line fit of the corresponding Tauc plot indicates the expected gap energy to be close to 0 eV. (Figure 3.5c)
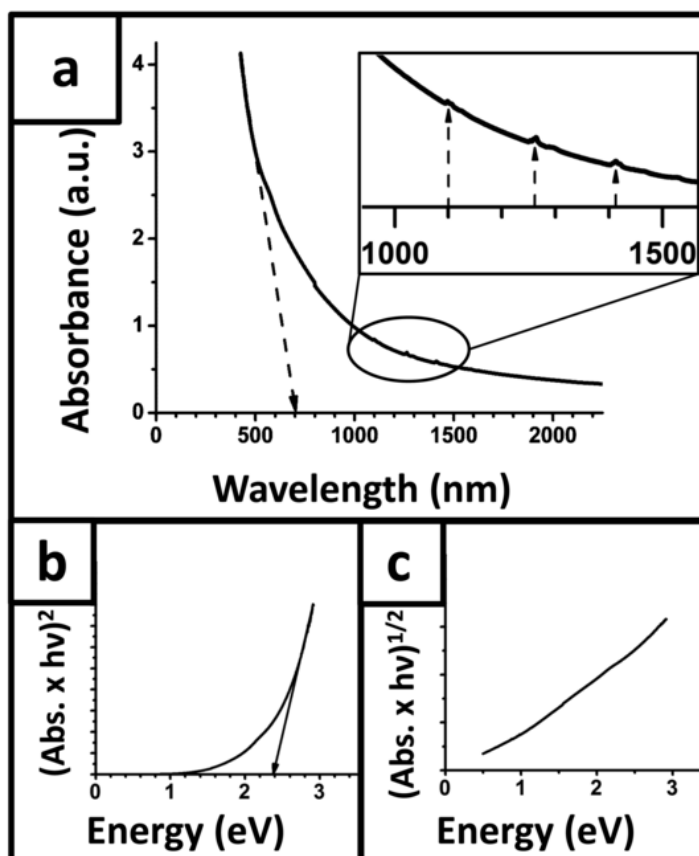
Figure 3.5 (a) Absorption spectrum of a α-Sm$_2$S$_3$ nanowire film with the arrow indicating the rough band edge at about 700 nm (1.77 eV). (inset) Magnified view of the circled region showing the characteristic f-to-f transition peaks of Sm$_2$S$_3$. Note: the small vertical line around 800nm is an artifact due to the change-over of the detectors. (b) Tauc plot of absorption data using a direct band gap model. The direct band gap was estimated to be 2.4 eV (arrow). (c) Tauc plot of absorption data using an indirect band gap model. The indirect band gap was estimated to be near 0 eV.

First principles DFT calculations of the electronic structure of α-Sm_2S_3 reveal several interesting features in the calculated band structure. First, the Fermi level in α-Sm_2S_3 is observed to lie in the midst of a large number of bands. (Figure 3.6a) The corresponding projected density of states (PDOS) diagram indicates that most of these bands are from the p-orbital contributions to the extended crystal structure. (Figure 3.6d) This would suggest that α-Sm_2S_3 is predicted to be metallic since right above the theoretical Fermi level E_F, there are a large number of permissible empty states spanning a width of 0.6 eV. However, above that there lies a direct 1.7 eV gap in the permissible band states rendering the total band gap to be 2.3 eV originally counting from E_F. These features were also visible in the experimental absorption spectrum (Figure 3.5). In particular, the absorption spectrum manifested a sharp increase in absorption starting around 1.77 eV, verifying the 1.7 eV gap found in the DFT calculated band structure. Additionally, according to the Tauc analysis of the absorption data (Figure 3.5b and 3.5c), the direct gap should be about 2.4 eV, a tight fit to the 2.3 eV found by the DFT calculations, while the indirect gap was found to be near 0 eV, which the DFT calculations do show to be an allowed transition. Hence the data implies that the $\square$-Sm_2S_3 may turn out to be an unconventional kind of p-type semiconductor with an abundant density of holes near E_F. In fact, similar observations on FeS_2 were reported by Sun et al [24]. However, in the case of FeS_2, Sun et al ascribed this ubiquitous p-type conductivity to oxygen impurities. For Sm_2S_3, this behavior appears to be truly intrinsic since even for the perfect unit cell used for DFT calculations, there are expected to be a density of holes near the Fermi level.

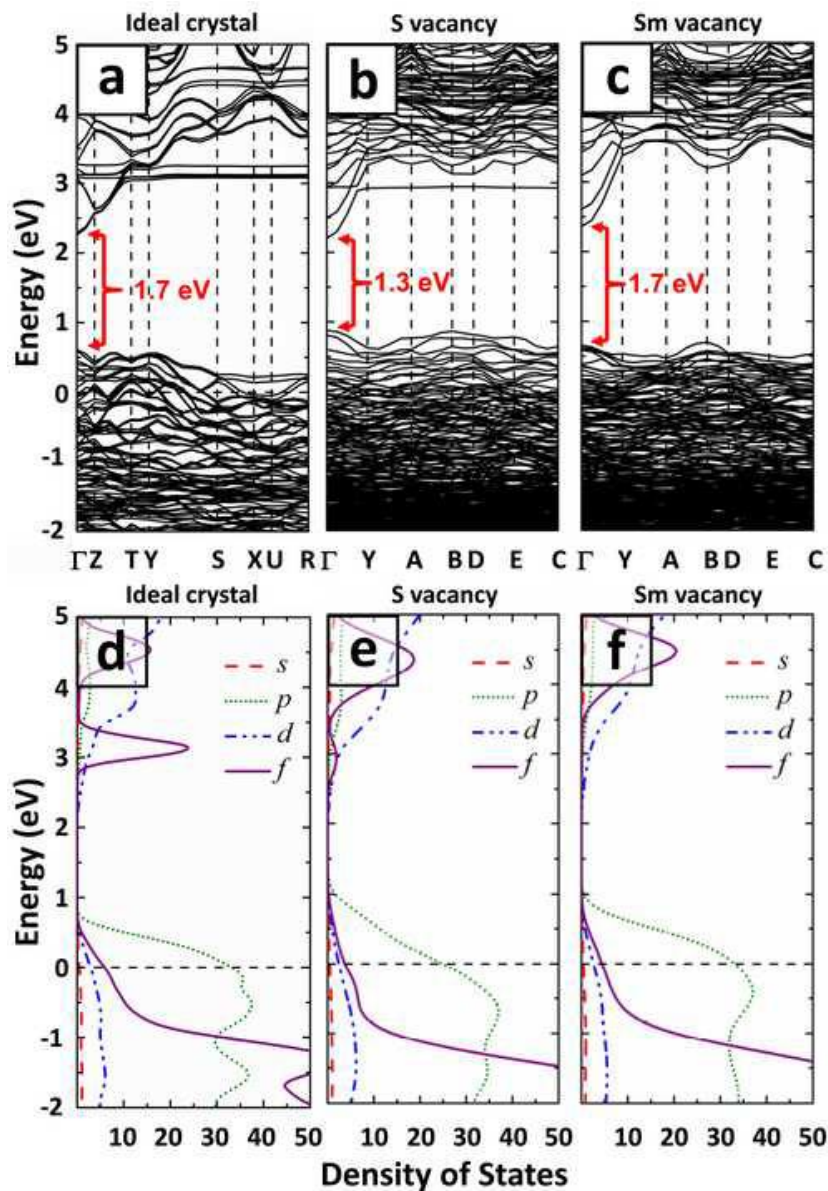**Figure 3.6** Band diagrams for (a) ideal 2:3 stoichiometry single crystalline α-Sm_2S_3 (b) sulfur-deficient $Sm_2S_{2.875}$ and (c) samarium-deficient $Sm_{1.875}S_3$ derived from DFT calculations. Density of state diagrams for the stoichiometric, sulfur-deficient, and samarium-deficient models are displayed in (d), (e), and (f) respectively. The Fermi level is indicated by the dashed lines.

Since our SAED studies of the α-Sm_2S_3 nanowires suggest that the crystal structure of our samples could have various systematic atomic vacancies, we performed additional DFT calculations to yield insights into the effects of such non-idealities on the electronic structure and band diagram of this material. Electronic structure computations were performed for the same models as indicated in Figure 3.4a and 3.4b to explore the two cases where either a single sulfur or samarium atom is missing for every two α-Sm_2S_3 unit cells, which corresponds to a 2.5% deficiency. In these deficient models, we maintained the lattice parameters and optimized the atomic positions. The calculated band structures and the corresponding densities of states of these two models display some features similar to the case of the ideal structure, but also some distinct features. (Figure 3.6) As a point of similarity, the Fermi levels for both models with vacancy defects remain consistently placed in the lower bands. This implies that α-Sm_2S_3 with a slight deficiency (2.5% of atoms missing) in either samarium or sulfur should still possess a p-type degenerate semiconductor resembling electronic structure. As a major point of difference, both atom deficient structures display reductions in the occupancies of the f-shell electrons around 3 eV in their density of state diagrams. This is expected to lead to a reduction of observed f-to-f transitions in optical absorption measurements, suggesting that monitoring the intensity of the absorption spikes (Figure 3.5 at 1100, 1270, and 1410 nm) may be a useful way of monitoring sample purity. Finally, since the p-orbital electrons in particular overlap the Fermi level, it is worth pointing out that the sulfur deficient model showed the biggest change in the density of states for the p-orbitals. For instance, in both the ideal crystal and the Sm deficient crystal, the p-orbital

PDOS at the Fermi level remains steady at 33 (electron state/eV) yet the sulfur deficient system has a p-orbital PDOS of 25 electron state/eV. Nevertheless, the remaining p-states were shifted upward, due to the oxidation state changes of Sm, rendering the direct gap in the band states of this model to be reduced to 1.3 eV (Figure 3.6b), which is an ideal band gap value for function in the solar cell range [25]. We further notice that the direct gap remains about the same, 1.7 eV, for the Sm deficient model as compared to that of the pure Sm_2S_3 (Figure 3.6 a and c). This suggests that careful control of the sulfur content in the unit cells may be particularly useful for controlling the degree of degeneracy and overall band gap of Sm_2S_{3-x} systems.

3.5 Conclusions

In summary, α-Sm_2S_3 has successfully been synthesized via a new chemical vapor deposition based process, which resulted in films composed of highly crystalline nanowires, and which showed a consistent [010] growth direction. The rough absorption edge of the α-Sm_2S_3 films produced by our method was found to be about 1.77 eV, a result that matched well with prior Sm_2S_3 studies [6b, c]. Density functional theory calculations predict that an ideal α-Sm_2S_3 crystal should have a direct gap in the band states spanning 1.7 eV. However, due to the Fermi level being located 0.6 eV below the direct band gap, a full transition from the Fermi level to above the band gap requires 2.3 eV, a value that corroborates well with the 2.4 eV direct band gap Tauc plot of the absorption data. Taken together, this data strongly suggests that α-Sm_2S_3 behaves intrinsically like a heavily doped p-type semiconductor, a property which has long been directly observed in the heavy band tailing in the absorption spectra of this class of

materials [10c-e, 18, 26], and a property that may make α-Sm_2S_3 particularly well suited for serving as the *p*-type leg of photovoltaic diodes or thermoelectric generators.

Our theoretical calculations of samarium- and sulfur-deficient crystal structures retained the distinct *p*-type degenerate semiconductor like band structures of the pure α-Sm_2S_3, but with significant modifications in the PDOS occupancies of the *p*- and *f*-shells neighboring the band gap. This suggests an encouraging method for controlling the electronic properties of samarium sesquisulfide, such as reducing the direct gap in the band states to a theoretically ideal ~1.3 eV [25], by modulating the atomic vacancies. Since the large trailing edge exhibited at the lower photon energies of our α-Sm_2S_3 film's absorption spectrum frequently appears in absorption spectra of *f*-block systems [14, 16], such fascinating "tailing" features in other lanthanide systems may likely be similarly rationalized using band extension arguments as in our theoretical electronic structure arguments for α-Sm_2S_3. We expect that this intrinsically degenerate behavior may be ideal in situations which require the use of a semiconductor, but are not amenable to extrinsic doping. Additionally, the predicted tunability of Sm_2S_3's optically active direct gap may make it an excellent candidate as a next generation photovoltaic material.

3.6 References

1.   Gulubkov, A. V., Kazanin, M. M., Kaminskii, V. V., Sokolov, V. V.,

Thermoelectric Properties of SmSx (x=.8-1.5). *Inorg. Mat.* **2003,** *39* (12), 1251-1256.

2.   Jundale, S. B.; Lokhande, C. D., (Photo)electrochemical studies on p-Sm_2S_3 films.

Solar Energy Materials and Solar Cells **1992,** *28*, 151-157.

3.   Maestro, P., Huguenin, D., Industrial applications of rare earths: which way for

the end of the century? *Journal of Alloys and Compounds* **1995,** *225*, 520-528.

4.   Chess, D. L., Chess, C. A., Biggers, J. V., White, W. B., Processing Ternary

Sulfide Ceramics: Powder Preparation, Sintering, and Hot-Pressing. *J. Am. Ceram. Soc.*

1983, *66* (1), 18-22.

5.   Yim, W. M., Fan, A. K., Stofko, E. J., Preparation and Properties of II-Ln_2-S_4

Ternary Sulfides. *Journal of the Electrochemical Society* **1973,** *120* (3), 441-446.

6.   (a) Schevciw, O., White, W. B., The Optical Absorption Edge of Rare Earth

Sesquisulfides and Alkaline Earth-Rare Earth Sulfides. *Mat. Res. Bul.* **1983,** *18*, 1059-

1068; (b) Forster, C. M., White, W. B., Optical absorption edge in rare earth

sesquisulfides. *Materials Research Bulletin* **2005,** *41*, 448-454; (c) Yuan, H., Zhang, J.,

Yu, R., Su, Q., Synthesis of Rare Earth Sulfides and their UV-vis Absorption Spectra.

Journal of Rare Earths **2009,** *27* (2), 308-311.

7.   Zalups, R. K., Koropatnick, J., *Molecular Biology and Toxicology of Metals*.

Taylor & Francis: NY, 2000.

8.   (a) Reda, S. M., Synthesis and optical properties of CdS quantum dots embedded

in silica matrix thin films and their applications as luminescent solar concentrators. *Acta*

Materialia **2008,** *56*, 259-264; (b) Bonnet, D.; Meyers, P., Cadmium-telluride-Material for thin film solar cells. *Journal of Materials Research* **1998,** *13* (10), 2740-2753.

9.   (a) Huis, M. A.; Veen, A.; Schut, H.; Eijt, S. W. H.; Kooi, B. J.; Hosson, J. T. M., Size-dependent structure of CdSe nanoclusters formed after ion implantation in MgO. *Acta Mater.* **2005,** *53*, 1305-1311; (b) Jaiswal, J. K.; Simon, S. M., Potentials and pitfalls of fluorescent quantum dots for biological imaging. *Trends Cell Biol* **2004,** *14* (9), 497-504.

10.   (a) Havlak, L.; Jary, V.; Nikl, M.; Bohacek, P.; Barta, J., Preparation, Luminescence and structural properties of RE-doped $RbLaS_2$ compounds. *Acta Materialia* **2011,** *59*, 6219-6227; (b) Flahaut, J.; Guittard, M. M.; Patrie, M., Les polysulfures des elements des terres rares. *Bulletin de la Societe Chimique de France* **1959**, 1917-1920; (c) Schevciw, O.; White, W. B., The Optical Absorption Edge of Rare Earth Sesquisulfides and Alkaline Earth-Rare Earth Sulfides. *Materials Research Bulletin* **1983,** *18*, 1059-1068; (d) Forster, C. M.; White, W. B., Optical absorption edge in rare earth sesquisulfides. *Mater. Res. Bull.* **2005,** *41*, 448-454; (e) Yuan, H.; Zhang, J.; Yu, R.; Su, Q., Synthesis of Rare Earth Sulfides and their UV-vis Absorption Spectra. *J. of Rare Earths* **2009,** *27* (2), 308-311.

11.   Ohta, M., Yuan, Haibin, Hirai, Shinji, Yajima, Yoshiyuki, Nishimura, Toshiyuki, Shimakage, Kazuyoshi, Thermoelectric properties of Th3P4-type rare-earth sulfides Ln2S3 (Ln=Gd, Tb) prepared by reaction of their oxides with CS2 gas. *J.l of Alloys and Compds* **2008,** *451*, 627-631.

12.   Picon, M., Domange, L., Flahaut, J., Guittard, M., Patrie, M., Les sulfures Me_2S_3 et Me_3S_4 des elements des terres rares. *Bulletin de la Societe Chimique de France* **1960,** *2*, 221-228.

13.   Vaughan, C. M., White, W. B., Role of Oxygen in Rare Earth Chalcogenide Semiconductors. *MRS Proceedings* **1987,** *97*, 397-402.

14.   Glurdzhidze, L. N., Kekhaiov, T. D., Bzhalava, T. L., Dzhabua, Z. U., Sanadze, V. V., Optical properties of thin samarium sesquisulfide films at 300 K. *Sov. Phys. Solid State* **1979,** *21* (11), 2021-2023.

15.   Pankove, J. I., *Optical Processes in Semiconductors*. Dover: New York, 1971.

16.   Witz, C., Huguenin, D., Lafait, J., Dupont, S., Theye, M. L., Comparative optical studies of Ce2S3 and Gd2S3 compounds. *J. Appl. Phys* **1995,** *79* (4), 2038-2042.

17.   Batlogg, B.; Kaldis, E.; Schlegel, A.; Wachter, P., Electronic structure of Sm monochalcogenides. *Physical review b* **1976,** *14* (12), 5503.

18.   Yan-Chao, H.; Jian-Feng, H.; Xuan, Z.; Li-Yun, C.; Li-Xiong, Y., Preparation of Sm_2S_3 thin films by liquid phase deposition method with self-assembled monolayers. *Journal of Alloys and Compounds* **2012,** *536*, 119-123.

19.   Pal, U.; Samanta, D.; Ghorai, S.; Chaudhuri, A. K., Optical constants of vacuum-evaporated polycrystalline cadmium selenide thin films. *J. Appl. Phys.* **1993,** *74* (10), 6368-6374.

20.   (a) Jeon, S.; Ahn, S.-E.; Song, I.; Kim, C. J.; Chung, U.-I.; Lee, E.; Yoo, I.; Nathan, A.; Lee, S.; Robertson, J.; Kim, K., Gated three-terminal device architecture to eliminate persistent photoconductivity in oxide semiconductor photosensor arrays. *Nature Materials* **2012**; (b) Guloy, A. M.; Ramlau, R.; Tang, Z.; Schnelle, W.; Baitinger,

M.; Grin, Y., A guest-free germanium clathrate. *Nature* **2006,** *443*, 320-323; (c) Liu, L. T.; Kopas, C.; Singh, R. K.; Hanley, R. M.; Newman, N., Growth and characterization of Ba(Cd$_{1/3}$Ta$_{2/3}$)O$_3$ thin films. *Thin Solid Films* **2012,** *520*, 6153-6157; (d) Muthu, K.; Meenakshisundaram, S. P., Synthesis, growth, structure and characterization of a new semiorganic crystal: Tetrakis(thiourea)zinc(II) picrate. *Mater. Lett.* **2012,** *84*, 56-58; (e) Tauc, J., Optical properties and electronic structure of amorphous Ge and Si. *Mater. Res. Bull.* **1968,** *3*, 37-46.

21.   Segall, M. D.; Philip, J. D. L.; Probert, M. J.; Pickard, C. J.; Hasnip, P. J.; Clark, S. J.; Payne, M. C., First-principles simulation: ideas, illustrations and the CASTEP code. *J. Phys: Condens. Matter* **2002,** *14*, 2717-2744.

22.   Perdew, J. P.; Burke, K.; Ernzerhof, M., Generalized Gradient Approximation Made Simple. *Phys. Rev. Lett.* **1996,** *77*, 3865-3868.

23.   (a) Marzari, N.; Vanderbilt, D.; Payne, M. C., Ensemble Density-Functional Theory for Ab Initio Molecular Dynamics of Metals and Finite-Temperature Insulators. *Phys. Rev. Lett.* **1997,** *79*, 1337-1340; (b) Payne, M. C.; Teter, M. P.; Allan, D. C.; et al, Iterative minimization techniques for ab initio total-energy calculations: molecular dynamics and conjugate gradients. *Rev. Mod. Phys.* **1992,** *64*, 1045-1097.

24.   Sun, R.; Chan, M. K. Y.; Kang, S. Y.; Ceder, G., Intrinsic stoichiometry and oxygen-induced *p*-type conductivity of pyrite FeS$_2$. *Physical Review B* **2011,** *84*.

25.   Araujo, G. L.; Marti, A., Absolute limiting efficiencies for photovoltaic energy conversion. *Sol. Energy Mater. Sol. Cells* **1994,** *33*, 213-240.

26.   Witz, C.; Huguenin, D.; Lafait, J.; Dupont, S.; Theye, M., Comparative optical studies of Ce$_2$S$_3$ and Gd$_2$S$_3$ compounds. *J. Appl. Phys* **1995,** *79* (4), 2038-2042.

Chapter 4

SULFIDES SUMMARY AND FUTURE DIRECTIONS

4.1 Lanthanide sulfides summary

Because of the unique electronic structures of the lanthanide metals compared to the transition metals, semiconductors prepared from the lanthanides have unique band structures. In particular, as the f-orbital electrons penetrate into the core shell electrons of the nucleus, compounds composed of lanthanide atoms may still have a large number of unoccupied energy states above and below the Fermi level. Consequently, semiconductors composed of lanthanide elements may exhibit properties much more similar to a metal or highly degenerate semiconductor, even while manifesting a several eV band gap.

Thin films of α-Sm_2S_3 were successfully grown by chemical vapor deposition (CVD) using samarium chloride salts, elemental sulfur, and hydrogen gas. The developed process was able to generate highly crystalline Sm_2S_3 over the course of a couple hours, a sizeable improvement compared to the prior methods of slowly sulfurizing lanthanide oxides. The optical properties of the generated Sm_2S_3 thin films were consistent with both the visible range band gap and with the highly degenerate semiconductor properties predicted from the DFT calculations.

Unfortunately, the highly textured nature of the CVD grown films complicated further study of the electronic and chemical properties of the lanthanide sulfides. Electronically, the nanowire texture of these films made the films discontinuous and

conductivity measurements unreliable. Additionally, the small amount of samarium sulfide materials generated per run by CVD made investigations into the chemical properties of the lanthanide sulfides difficult and slow.

4.2 Future work

If the lanthanide sulfides are ever to find ready commercial applications of their unique electronic structures, a rapid low cost synthetic approach is necessary. Considering the relative ease of forming lanthanide oxides compared to sulfides, the sulfides would need to be prepared in an anaerobic environment. This is further complicated by the ability of the lanthanides to hydrolyze water [1], meaning that any solution approach for generating the lanthanide sulfides would also need to be in non-aqueous conditions.

One approach that shows promise is the high-pressure solvothermal synthesis of lanthanide sulfides. In order for such a method to work, a solvent is needed that has no OH groups, which can be hydrolyzed, but it needs to be able to effectively dissolve lanthanide salts. Additionally, the solvent should be able to dissolve elemental sulfur in order to keep excess sulfur in solution. Finally of course, the solvent should not dissolve much Ln_2S_3 so that once the lanthanide sulfide forms it can precipitate out of solution driving the reaction towards products. The most successful solvent I have found is pyridine. As a highly polar small molecule, pyridine effectively solubilizes the lanthanide chlorides and sulfates. Additionally, pyridine is well known to dissolve elemental S_8 with a solubility of 10.5 g/100g [2]. Finally, as a cyclic compound with no oxygen, pyridine does not oxidize the lanthanide ions in solution.

By utilizing cerium sulfate, elemental sulfur, and thiourea, a brilliant purple solid was successfully prepared (Figure 4.1). As stated before, elemental S_8 is not an effective sulfurizing agent as energy must be supplied to break the sulfur-sulfur bonds. Instead, thiourea is utilized as a source of single sulfur atoms. Industrially, it may be preferable to utilize Na_2S instead of thiourea as such a process would generate less organic waste. These materials were of too poor crystallinity for XRD confirmation of the structure with additional recrystallization or sintering still necessary for XRD characterization.

Alternately, Ghosh et al have recently published a thermal decomposition method utilizing synthetically prepared lanthanide complexes [3]. In this method, a complex of Eu^{3+}, Sm^{3+}, Nd^{3+}, Td^{3+}, or Yb^{3+} with 2-aminocyclopenetene-1-dithiocarboxylic acid ligands were prepared in anhydrous conditions, followed by vacuum drying and heating to 650 °C under argon to decompose and remove the ligands, leaving behind highly crystalline Ln_2S_3 or LnS. Such a synthetic method is likely to leave organic impurities in the sample, but this issue could likely be overcome with subsequent extractions or recrystallizations.

Potential applications of the lanthanide sulfides would primarily make use of their optical and electronic properties. Currently, the main application of these compounds is as lead and cadmium free pigments [4]. Such an application would of course benefit from a lower cost method of production. However, the largest advantage of improved synthetic methods would be having a larger volume of material available for refining and crystallization. As these materials combine a visible range band gap with metallic properties on the infrared range, these materials may serve as next generation solid-state laser materials. This is particularly relevant as the current semiconductor based lasers are

wattage limited by their thermal conductivities [5]. Additionally, the highly degenerate semiconductor properties of these compounds may be highly desirable in certain diodes such as Zener diodes. In such an application, lanthanide sulfide based materials may serve as high wattage diodes, such as those utilized in high power AC-DC converter stations. Last, but certainly not least, the lanthanide sulfides may serve as next generation photocatalytic materials for processes such as the photoreduction of CO_2. [6]

Figure 4.1 Commercial Ce$_2$S$_3$ (left) compared to solvothermally prepared cerium sulfide powder (right).

4.3 References

1.   Cotton, F. A.; Wilkinson, G., *Advanced Inorganic Chemistry*. second ed.; Interscience Publishers: New York, 1966.

2.   Meyer, B., Elemental Sulfur. *Chemical Reviews* 1976, *76* (3), 367-388.

3.   Ghosh, A. B.; Saha, N.; Sarkar, A.; Srivastava, D. N.; Paul, P.; Adhikary, B., Solvent assisted and solvent free orientation of growth of nanoscaled lanthanide sulfides: tuning of morphology and manifestation of photocatalytic behavior. *RSC Advances* 2015, *5*, 102818-102827.

4.   Maestro, P., Huguenin, D., Industrial applications of rare earths: which way for the end of the century? *Journal of Alloys and Compounds* 1995, *225*, 520-528.

5.   Honea, E. C.; Beach, R. J.; Sutton, S. B.; Speth, J. A.; Mitchell, S. C.; Skidmore, J. A.; Emanuel, M. A.; Payne, S. A., 115-W Tm:YAG Diode-Pumped Solid-State Laser. *IEEE Journal of Quantum Electronics* 1997, *33* (9), 1592-1600.

6.   Kanemoto, M.; Shiragami, T.; Pac, C.; Yanagida, S., Semiconductor Photocatalysis. Effective Photoreduction of Carbon Dioxide Catalyzed by ZnS Quantum Crystallites with Low Density of Surface Defects. *J. Phys. Chem.* 1991, *96*, 3521-3526.

Chapter 5

INTRODUCTION TO CERIUM OXIDE AND CO$_2$ CHEMISTRY

5.1 Cerium electronic structure

All of the lanthanides prefer to take the 3+ oxidation state. However, cerium is the closest to an exception in that trend as under oxidative conditions it may take a 4+ state. The ground state electronic configuration of cerium is [Xe]4f^{2}6s^2. As described in Chapter 1, it is very difficult to strip more than one electron out of the lanthanide's 4f subshell due to it penetrating deeply into the core xenon 5p subshell. However, if two 4f electrons are stripped from a cerium atom, the ion is afforded substantial stability as it is able to achieve the noble gas configuration of xenon. Consequently, cerium is a uniquely useful redox element as it is relatively easy for it to switch between the 3+ and 4+ states.

In terms of electrochemical potential, the reduction of Ce^{4+} to Ce^{3+} is accompanied by a standard electrode potential of 1.72 Volts [2]. In practical chemistry terms, this is a ΔG of -166 kJ/mol. Although still a massive difference in potential energy, this is a small enough difference for cerium to exhibit a distinctive valence fluctuation phenomenon [3] in which even bulk properties such as metallic radius are found to behave somewhere in-between a trivalent and tetravalent state complete with an isomorphic phase transition between the primarily 3+ γ phase and the primarily 4+ α phase metals under pressure. Unsurprisingly, this fluctuating valency significantly impacts cerium's chemical properties.

5.2 Cerium oxide (ceria)

The oxide of cerium (ceria) has unique properties in the lanthanide series as a consequence of cerium's unique electronic structure. Unlike the rest of the lanthanide oxides, ceria takes a stable bulk oxide of the form CeO_2. This compound is a cubic fluorite (CaF_2 prototyping) crystal structure (Fm-3m) in which each cerium atom has a cubic coordination to 8 oxygen ions and each oxygen ion is tetrahedrally coordinated to 4 cerium ions (see Figure 5.1). This leaves each cerium atom in the 4+ oxidation state.

Fluorite ceria is stable with cerium in the 4+ state primarily due to the huge lattice energy of the fluorite structure. As a first order approximation, the Kapustinskii equation[4] estimates the lattice energy as:

$$U_L = K \frac{v\,|z^+||z^-|}{r^+ + r^-} \cdot \left(1 - \frac{d}{r^+ + r^-}\right)$$

where K = 1.2025 x 10^{-4} Jm/mol, v is the number of ions in the formula, z^+ is 4, z^- is 2, and d is 3.45 x 10^{-11}m. For cerium, the ionic radius in the 4+ state is 0.97 Å. This is an extremely small ionic radius for a lanthanide, and is only possible for a 4+ ion. From the crystallographic data, the ionic radius of the 2- oxygen is then 1.37 Å. Solving for U_L, we end up with a massive lattice energy term of 10,500 kJ/mol. Basically, even though a free cerium ion is more stable as a 3+ ion, the huge lattice stabilization energy afforded by the fluorite crystal structure makes cerium more stable as a 4+ oxide.
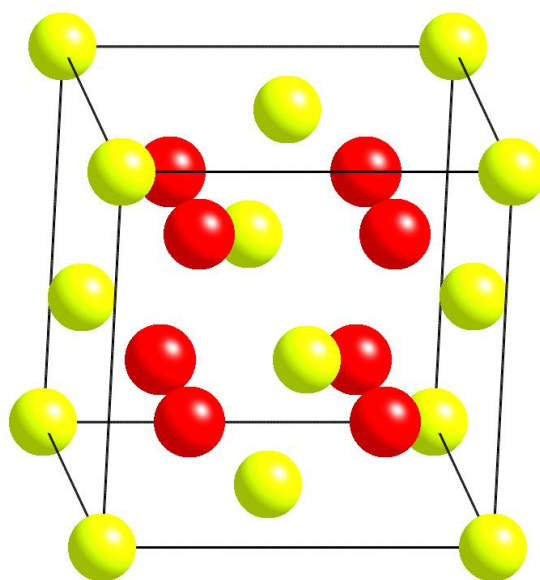
Figure 5.1 Cubic fluorite structure of ceria (CeO$_2$). Yellow spheres are Ce, red spheres are oxygen. Image produced from CrystalMaker$^®$ using ICDD crystallographic data.

An important caveat must be made when claiming that ceria is most stable as a 4+ oxide: equations for the lattice energy assume complete coordination. In other words, for a cerium ion in the middle of the fluorite ceria lattice, a 4+ oxidation state is by far the most stable. However, a cerium ion on the surface of a crystal is missing at least one nearest neighbor. In fact, if the ceria 100 surface is cerium terminated, each of those cerium ions is missing four nearest oxygen neighbors. Because of this, the lattice energy is a much smaller term for surface ions. With a smaller lattice energy term, cerium ions again exhibit a fluctuating valency with a statistically significant ratio of Ce^{3+} and Ce^{4+} ions at the surface, along with the ability to flip between the two oxidation states as a consequence of cerium's unique electronic structure. This bulk stability coupled with significant surface instability is the heart of what makes ceria such an active heterogeneous catalyst.

5.3 Ceria chemistry

Ceria is used both as an active heterogeneous catalyst and as a catalyst support in a wide variety of chemical applications from hydrocarbon cracking [5] to specialty organic applications [6-8]. These applications broadly make use of a number of interrelated properties of ceria. Specifically, these applications make use of ceria's high oxygen mobility, redox chemistry, and Lewis basicity.

Likely the most well-known application of ceria is as a component of the three-way catalytic converter commonly used in automobiles. In this application, three-way catalysis refers to the catalyst's ability to oxidize CO and hydrocarbons to CO_2 while

simultaneously reducing NO_x compounds to nitrogen [5]. In this application, catalysts typically consist of a silica-alumina support supporting a range of noble metal catalysts. What is often forgotten is cerium is the third most abundant element in catalyst with a ratio of roughly 10:100 cerium to silicon atoms [9]. For this application, the primary role that ceria plays is as an oxygen buffer system storing excess oxygen when the exhaust gas is O_2 rich and allowing for efficient oxidation even as the exhaust gases cycle between oxygen rich and poor pulses.

The key feature that enables ceria's use for oxygen storage is the incomplete coordination of the cerium ions at the surface. Because of this, the lattice energy term at the surface is not as high as what is calculated for bulk atoms and a significant percentage of cerium ions take a lower energy 3+ oxidation state instead of the 4+ state taken by internal cerium atoms. In order to maintain a balanced charge on the ceria particle, a corresponding amount of oxygen atoms must leave the ceria lattice causing characteristic oxygen vacancy defects (OVDs) on the ceria surface. Note that unlike typical crystallographic defects, which may be interstitial or Schottky (meaning that both anions and cations are absent), ceria surface defects are predominantly oxygen anions [10]. Consequently, the following reversible reaction can take place on the ceria surface:

$$CeO_2 \rightleftharpoons CeO_{2-x} + x/2 \; O_{2\,(g)} \; (0<x<0.5)$$
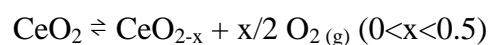
This reversible reaction allows the nanoscale ceria (maximizing active surface area) incorporated into three-way catalysts to store oxygen when the partial pressure of O_2 is high, and release O_2 when the partial pressure is reduced. Additionally, as any of the surface cerium ions may switch between the 3+ and 4+ states (fluctuating valency levels),

surface OVDs enable oxygen mobility through the crystal, useful not just in three-way catalysts but in fuel cell membranes as well [11,8].

In addition to storing and releasing oxygen, ceria is also useful directly in catalysis. In general, ceria's effectiveness as a catalyst comes from the redox properties of its surface. As ceria's surface is a mixture of Ce^{3+} and Ce^{4+} states, the surface can both be further oxidized and further reduced. Because of this, ceria can be directly used for dehydrogenation and carbon-carbon coupling reactions [8]. Additionally, ceria has been demonstrated to be effective for the cyanosilylation of aldehydes using trimethylsilyl cyanide [7].

Finally, ceria is also chemically useful for its Lewis basicity. Although ceria is bifunctional as a redox catalyst, chemical adsorption studies have shown ceria to have a very basic surface with negligible acid sites [12]. This is likely a consequence of ceria's surface normally being oxygen terminated [5]. Since surface oxygen atoms are extremely negatively charged, they act as excellent electron donors to adsorbing Lewis acids. For this reason, the entire lanthanide oxide series is considered basic, albeit to different degrees [12]. However, the combination of fluctuating valency and Lewis basicity makes ceria, in particular, excellent for CO_2 adsorption and carbonate synthesis [13-15].

5.4 Carbon dioxide chemistry

Carbon dioxide is a byproduct of fossil fuel combustion for energy generation. As a consequence, CO_2 is generated as a waste on a colossal scale. In 2012, over 4.8 billion metric tons of carbon dioxide was generated in the U.S. alone [16]. Since CO_2 has been attributed as a key contributor to climate change, it has become increasingly important to

find new ways to utilize and recycle CO_2. Additionally, as such an abundant waste product of energy generation, CO_2 is worth considerably less than nothing (financial programs exist around the world to consume CO_2). Consequently, there is substantial financial opportunity to generate a value added product other than carbon dioxide as the final byproduct of energy generation. Current CO_2 utilization is close to 200 megatons/year, roughly 0.62% of yearly emissions [1]. To become significant, this usage needs to increase by at least an order of magnitude.

Currently, CO_2 utilization primarily takes advantage of carbon dioxide's excellent Lewis acid properties. For instance, urea (H_2NCONH_2) is commercially produced from NH_3 (a weak base) and CO_2. This mature technology is a high pressure process (24 MPa) making use of the two equilibrium reactions shown in scheme 5.1. Currently, this process is used to produce urea at a rate of 155 megatons/year [1]. At these production levels, it is already critical that the process is continuous, but this is made doubly important by the need to remove urea and water from the system in order to shift the reaction equilibria towards products. For any such continuous production process, percent yield becomes less important (note the unused NH_3 and CO_2 are separated and fed back into the reactant stream), but excellent selectivity and reaction kinetics are absolutely critical for production.
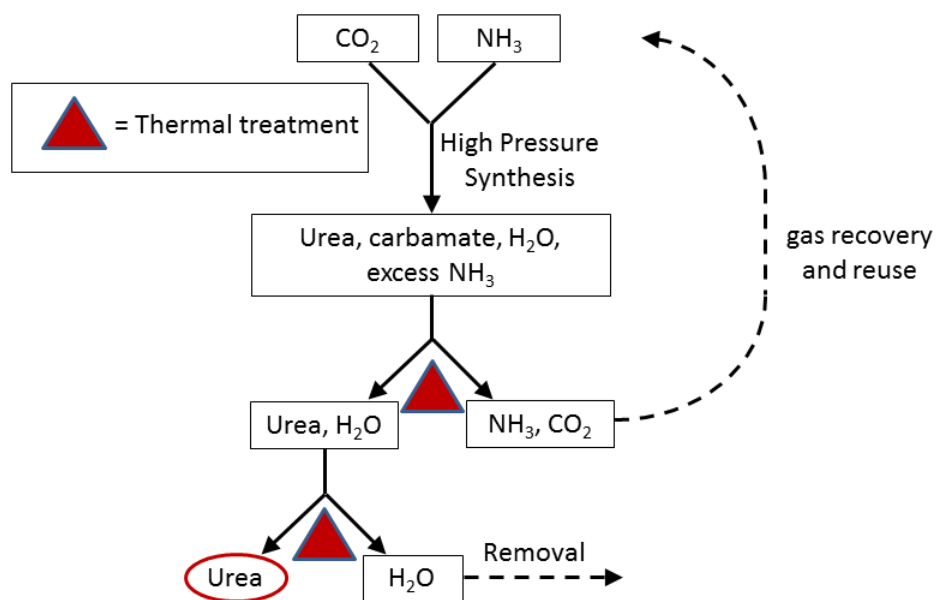
Figure 5.2 Process flow diagram of urea synthesis from CO_2. Adapted with permission from reference [1]. Copyright 2014 American Chemical Society.

Unfortunately, a number of factors make utilizing CO_2 as a chemical reactant very difficult. Most significantly, CO_2 is the most oxidized form of carbon and is an extremely stable molecule with a ΔG_f^o of -396 kJ/mol [1]. Additionally, as a gaseous reactant, the entropy change of the reaction is unlikely to be positive (since products tend to be solid, liquid, or longer chain gases), meaning that the driving force for a spontaneous reaction needs to be a decrease in enthalpy. This is typically accomplished by keeping carbon in its +4 state while increasing the ratio of oxygen to carbon by forming inorganic or organic carbonates. Since such a process is highly entropy unfavored, elevated temperatures are expected to be undesirable for most reactions utilizing gaseous CO_2 as a reagent.

The utilization of gaseous CO_2 as a reactant also carries a number of kinetic limitations. Specifically, CO_2 is a non-polar molecule with two extremely strong carbon-oxygen double bonds that need to be weakened or broken in order to polarize the molecule and enable a nucleophilic attack on the carbon atom. This is referred to as CO_2 activation. Essentially, CO_2 is in such a stable low energy well that pushing the molecule to a transition state takes a large amount of energy. Couple this kinetic limitation with a need for low reaction temperatures and it becomes clear that a catalyst is essential for most any form of industrial application of carbon dioxide.

5.5 Organic carbonates from CO_2

One promising CO_2 utilization reaction is the generation of organic carbonates from CO_2 and alcohols (or diols). Organic carbonates are a family of organic molecules

of the general formula $R_1O(C=O)OR_2$. In general, they are divided into the categories of linear and cyclic carbonates (Figure 5.2) of varying complexity depending on the complexity of the reagent alcohol (for linear carbonates[17]) or polyol (for cyclic carbonates[18]). These compounds are commercially important for a range of applications including lithium ion battery electrolytes (particularly ethylene carbonate[19]) and polycarbonate plastics (notably diphenyl and dimethyl carbonate[20]).

For lithium ion batteries, a mixture of linear and cyclic organic carbonates is essential for use as the battery electrolyte solvent. These compounds are essential to efficient battery operation because they are very stable compounds even under the large reductive and oxidative potentials generated in a modern 3.5 volt battery. Other than glycerol carbonate, the carbonate family shown in Figure 5.2 are all aprotic and with varying degrees of polarity. Consequently, carbonate mixtures are able to dissolve a substantial amount of lithium salt while resisting decomposition. [21].
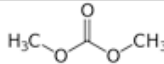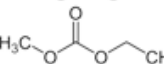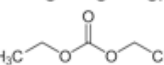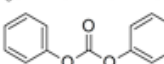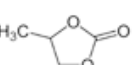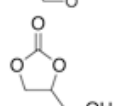
Carbonate	Abbreviation	Name
DMC	DMC	Dimethyl carbonate
EMC	EMC	Ethyl methyl carbonate
DEC	DEC	Diethyl carbonate
DPC	DPC	Diphenyl carbonate
EC	EC	Ethylene carbonate
PC	PC	Propylene carbonate
GC	GC	Glycerol carbonate

Figure 5.3 Simple examples of linear and cyclic carbonates. Note that in cyclic carbonates, two oxygens of the carbonate group itself are part of a ring.

The largest application for organic carbonates is as precursors to polycarbonate plastics. In particular, diphenyl carbonate (DPC) and dimethyl carbonate (DMC) are industrially utilized for the production of polycarbonate plastics, of which there is a demand for ~4.5 million metric tons per year[22]. Currently, polycarbonate plastics are not commodity plastics. Because of their price, polycarbonate plastics occupy a niche between high priced specialty polymers and the commodity plastics[20]. Conventionally, polycarbonate plastic is produced by one of two processes. Traditionally, polycarbonates were produced by the Interfacial Polymerization process. This process relies on the phosgenation of onbisphenol A (BPA) in solvent (such as dichloromethane) using a tertiary amine catalyst under basic conditions (maintained using NaOH) [20]. The drawbacks of this method are the highly toxic nature of phosgene gas ($COCl_2$), as well as the considerable solvent and salt wastes from this process. Alternatively, polycarbonate can be produced by the base-catalyzed transesterification reaction of bisphenol with diphenyl carbonate. This process produces the polymer without solvent, and without the use of phosgene, making for a significantly greener process[20].

Initially, DPC was still produced by a phosgene reaction, somewhat limiting the environmental appeal of the transesterification process. More recently, a two-step process has been applied for the production of DPC:

1) $CH_3OH + CO + \frac{1}{2} O_2 \rightleftharpoons DMC + H_2O$

2) $DMC + 2Phenol \rightleftharpoons DPC + 2CH_3OH$
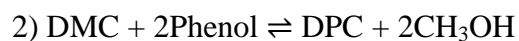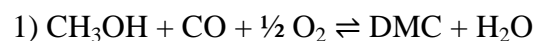
where step one is catalyzed by a transition metal catalyst such as cuprous chloride or

Cu^+X zeolite catalyst[23] and step two is catalyzed by $Ti(OR)_4$[24]. This use of carbon

monoxide as the carbon source eliminates the use of phosgene gas, but neither reaction is

very product favored with product dehydration needed to shift reaction 1 to the right

while reaction 2 must be carried out in stages with continuous product removal to

complete the alcohol substitutions[20].

A further improvement in the environmentally friendly production of

polycarbonates could be realized by the direct synthesis of organic carbonates from CO_2:

$$2ROH + CO_2 \rightleftharpoons (RO)_2CO + H_2O$$
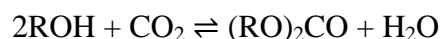
Such a process would use one mole of CO_2 for each mole of organic carbonate produced.

Production of polycarbonate plastics produced from CO_2 would then serve as a form of

carbon dioxide recycling where the solid product made from CO_2 is also a useful product

instead of just a form of CO_2 sequestration. However, due to the decreased activity of

CO_2 compared to CO, excellent catalyst design is essential for commercial utilization.

5.6 Catalysts for the direct synthesis of organic carbonates

Numerous catalysts have been explored for the direct conversion of CO_2 and

methanol to DMC. These catalysts include $Co_{1.5}PW_{12}O_{40}$,[25] K_2CO_3,[26] KOH,[26] ZrO_2,[27]

and CeO_2.[14-15, 28] As a well-used catalyst support with excellent Lewis base properties,

ceria in particular has been extensively studied after doping with Al_2O_3,[15] ZrO_2, Ga_2O_3,

Ni_2O_3, Fe_2O_3, and other lanthanide elements.[29] Unfortunately, the direct conversion of

CO_2 to DMC reported in literature remains characterized by low yields (up to 7.2%[27]) at

high temperatures (80-200 °C [26] [25]) and long reaction times of 3 [29] to 10 hours [26] ,limited

by the thermodynamic stability of CO_2 as discussed previously. [25] [30] To improve product

yields, dehydrating agents such as orthoesters, and molecular sieves have been explored

for this synthetic route.[31] However, orthoesters are expensive as they would need to be

added on a stoichiometric basis with the moles of CO_2 consumed, an unviable proposition

for the amounts of CO_2 that ought to be utilized. Additionally, the life time of molecular

sieves for dehydration reactions is short, on the order of hours. [32] Such a life time

limitation makes it necessary for the molecular sieves to be continuously replaced and

regenerated for large scale processes, an environmental concern if net CO_2 is generated.

5.7 Focus of the oxide section of this dissertation

The latter half of this dissertation focuses on understanding how ceria catalyzes

the direct synthesis of organic carbonates from CO_2 and alcohols. In particular, since

methanol is the simplest alcohol, the reaction of methanol and CO_2 is explored with the

express goal of insights in ceria catalyst design. Chapter 6 focuses specifically on the

liquid chromatography method development which was necessary for optimally low

limits of detection of organic carbonates. Chapter 7 focuses on analyzing the reaction

kinetics of the direct synthesis of dimethyl carbonate using a method of initial rates

approach and the developed liquid chromatography method. From the kinetics data, a

reaction mechanism is discussed particularly with regards to insights into improved

catalyst design. Finally, future studies are proposed for rational catalyst improvements

from an improved understanding of the surface reaction mechanism.

5.8 References

1.   Aresta, M.; Dibenedetto, A.; Angelini, A., Catalysis for the Valorization of Exhaust Carbon: from CO2 to Chemicals, Materials, and Fuels. Technological Use of CO2. *Chemical Reviews* **2014,** *114*, 1709-1742.

2.   Lide, D. R., *CRC Handbook of Chemistry and Physics*. 86 ed.; Taylor & Francis: NY, 2005.

3.   Lawrence, J. M.; Riseborough, P. S.; Parks, R. D., Valence fluctuation phenomena. *Reports on Progress in Physics* **1981,** *44* (1), 1-84.

4.   Kapustinskii, A. F., Lattice energy of ionic crystals. *Q. Rev. Chem. Soc.* **1956,** *10*, 283-294.

5.   Trovarelli, A., *Catalysis by Ceria and Related Materials*. 1 ed.; Imperial College Press: Hackensack, NJ, 2002; Vol. 2.

6.   Gernhart, Z. C.; Bhalkikar, A.; Burke, J. J.; Sonnenfeld, K. O.; Marin, C. M.; Zbasnik, R.; Cheung, C. L., One-pot conversion of cellobiose to mannose using a hybrid phosphotungstic acid-cerium oxide catalyst. *RSC Advances* **2015,** *5*, 28478-28486.

7.   Wang, G.; Wang, L.; Fei, X.; Zhou, Y.; Sabiriano, R. F.; Mei, W.-N.; Cheung, C. L., Probing the bifunctional catalytic activity of ceria nanorods towards the cyanosilylation reaction. *Catalysis Science & Technology* **2013,** *3*, 2602-2609.

8.   Trovarelli, A.; Fornasiero, P., *Catalysis by Ceria and Related Materials*. 2 ed.; Imperial College Press: Hackensack, NJ, 2013; Vol. 12.

9.   Fernandez-Ruiz, R.; Furio, M.; Galisteo, F. C.; Larese, C.; Granados, M. L.; Mariscal, R.; Fierro, J. L. G., Chemical Analysis of Used Three-Way Catalysts by Total Reflection X-ray Fluorescence. *Anal. Chem.* **2002,** *74*, 5463-5469.

10.   Steel, B. C. H.; Floyd, J. M., The Oxygen Self-Diffusion and Electrical Transport Properties of Non-Stoichiometric Ceria and Ceria Solid Solutions. *Proc. Brit. Ceram. Trans.* **1971,** *19*, 55-76.

11.   Menendez, C. L.; Zhou, Y.; Marin, C. M.; Lawrence, N. J.; Coughlin, E. B.; Cheung, C. L.; Cabrera, C. R., Preparation and characterization of Pt/Pt:CeO$_{2-x}$ nanorod catalysts for short chain alcohol electrooxidation in alkaline media. *RSC Advances* **2014,** *4*, 33489-33496.

12.   Sato, S.; Takahashi, R.; Kobune, M.; Gotoh, H., Basic properties of rare earth oxides. *Applied Catalysis A: General* **2009,** *356*, 57-63.

13.   Tomishige, K.; Yasuda, H.; Yoshida, Y.; Nurunnabi, M.; Li, B. T.; Kunimori, K., Catalytic performance and properties of ceria based catalysts for cyclic carbonate synthesis from glycol and carbon dioxide. *Green Chemistry* **2004,** *6* (4), 206-214.

14.   Santos, B. A. V.; Pereira, C. S. M.; Silva, V. M. T. M.; Loureiro, J. M.; Rodrigues, A. E., Kinetic study for the direct synthesis of dimethyl carbonate from methanol and CO$_2$ over CeO$_2$ at high pressure conditions. *Applied Catalysis A: General* **2013,** *455*, 219-226.

15.   Aresta, M.; Dibenedetto, A.; Pastore, C.; Angelini, A.; Aresta, B.; Papai, I., Influence of Al$_2$O$_3$ on the performance of CeO$_2$ used as catalyst in the direct carboxylation of methanol to dimethylcarbonate and the elucidation of the reaction mechanism. *Journal of Catalysis* **2010,** *269*, 44-52.

16.   *Inventory of U.S. Greenhouse Gas Emissions and Sinks: 1990 – 2012*; Office of Atmospheric Programs, US Environmental Protection Agency.: Washington DC, 2014.

17.   Honda, M.; Tamura, M.; Nakagawa, Y.; Nakao, K.; Suzuki, K., Organic carbonate synthesis from CO2 and alcohol over CeO2 with 2-cyanopyridine: Scope and mechanistic studies. *Journal of Catalysis* **2014,** *318*, 95-107.

18.   Honda, M.; Tamura, M.; Nakao, K.; Suzuki, K.; Nakagawa, Y.; Tomishige, K., Direct Cyclic Carbonate Synthesis from CO_2 and Diol over Carboxylation/Hydration Cascade Catalyst of CeO_2 with 2-Cyanopyridine. *ACS Catalysis* **2014,** *4* (1893-1896).

19.   Aurbach, D.; Talyosef, Y.; Markovsky, B.; Markevich, E.; Zinigrad, E.; Asraf, L.; Gnanaraj, J. S.; Kim, H.-J., Design of electrolyte solutions for Li and Li-ion batteries: a review. *Electrochimica Acta* **2004,** *50*, 247-254.

20.   Polycarbonates. In *Kirk-Othmer Enc. of Chem. Tech.*, 5 ed.; Kirk-Othmer, Ed. John Wiley & Sons: NY, 2004; Vol. 19, pp 797-827.

21.   (a) Etacheri, V.; Marom, R.; Elazari, R.; Salitra, G.; Aurbach, D., Challenges in the development of advanced Li-ion batteries: a review. *Energy & Environmental Science* **2011,** *4*, 3243-3262; (b) Xu, K., Electrolytes and Interphases in Li-Ion Batteries and Beyond. *Chemical Reviews* **2014,** *114*, 11503-11618.

22.   *IHS Chemical 2012 World Polycarbonate and ABS Analysis*; IHS Inc.: 2012.

23.   Anderson, S. A.; Root, T. W., Kinetic studies of carbonylation of methanol to dimethyl carbonate over Cu^+X zeolite catalyst. *Journal of Catalysis* **2003,** *217*, 396-405.

24.   Harrison, G. E.; Dennis, A. J.; Sharif, M. Continuous Production Process of Diarylcarbonates. 5426207, 1995.

25.   Aouissi, A.; Al-Othman, Z. A.; Al-Amro, A., Gas-Phase Synthesis of Dimethyl Carbonate from Methanol and Carbon Dioxide Over $Co_{1.5}PW_{12}O_{40}$ Keggin-Type Heteropolyanion. *International Journal of Molecular Sciences* **2010,** *11*, 1343-1351.

26.   Cai, Q.; Lu, B.; Guo, L.; Shan, Y., Studies on synthesis of dimethyl carbonate from methanol and carbon dioxide. *Catalysis Communications* **2009,** *10*, 605-609.

27.   Eta, V.; Maki-Arvela, P.; Leino, A.-R.; Kordas, K.; Salmi, T.; Murzin, D. Y.; Mikkola, J.-P., Synthesis of Dimethy Carbonate from Methanol and Carbon Dioxide: Circumventing Thermodynamic Limitations. *Ind. Eng. Chem. Res.* **2010,** *49*, 9609-9617.

28.   (a) Wang, S.; Zhao, L.; Wang, W.; Zhao, Y.; Zhang, G.; Ma, X.; Gong, J., Morphology control of ceria nanocrystals for catalytic conversion of CO_2 with methanol. *Nanoscale* **2013,** *5*, 5582-5588; (b) Yoshida, Y.; Arai, Y.; Kado, S.; Kunimori, K.; Tomishige, K., Direct synthesis of organic carbonates from the reaction of CO_2 with methanol and ethanol over CeO_2 catalysts. *Catalysis Today* **2006,** *115*, 95-101.

29.   Lee, H. J.; Joe, W.; Jung, J. C.; Song, I. K., Direct synthesis of dimethyl carbonate from methanol and carbon dioxide over Ga_2O_3-CeO_2-ZrO_2 catalysts prepared by a single-step sol-gel method: Effect of acidity and basicity of the catalysts. *Korean J. Chem. Eng.* **2012,** *29* (8), 1019-1024.

30.   Dibenedetto, A.; Angelini, A.; Aresta, M.; Ethiraj, J.; Fragale, C.; Nocito, F., Converting wastes into added value products: from glycerol to glycerol carbonate, glycidol and epichlorohydrin using environmentally friendly synthetic routes. *Tetrahedron* **2011,** *67* (6), 1308-1313.

31.   Stoye, D., Solvents. In *Ullmann's Encyclopedia of Industrial Chemistry*, Wiley-VCH Verlag GmbH & Co. KGaA: 2000.

32.   Sun, Q.; Wang, N.; Xi, D.; Yang, M.; Yu, J., Organosilane surfactant-directed synthesis of hierarchical porous SAPO-34 catalysts with excellent MTO performance. *Chemical Communications* **2014,** *50* (49), 6502-6505.

Chapter 6

LIQUID CHROMATOGRAPHY METHOD DEVELOPMENT FOR SEPARATING ORGANIC CARBONATES

6.1 Introduction

Lithium ion batteries have been one of the biggest successes of modern electrochemistry. Their usage has grown from small portable music players to automobile and aviation battery systems [1]. Due to continued demand for new batteries offering greater energy densities, higher power densities, better safety and shorter charging times, lithium ion battery research has continually received increased attention. One thrust in lithium ion battery research has been the development of improved electrolyte chemistry. Such a focus makes good sense from a historical perspective since it was the use of ethylene carbonate in the late 1980s as a replacement for the aprotic propylene carbonate solvent that reduced graphite exfoliation on recharging and enabled rechargeable lithium ion batteries to become a commercial reality [2]. This success of battery electrolyte research has since attracted research for similar revolutionary improvements in electrolyte chemistry, with the current state-of-the-art consisting of binary and tertiary mixtures of ethylene carbonate (EC), propylene carbonate (PC), dimethyl carbonate (DMC), ethyl-methyl carbonate (EMC), and diethyl carbonate (DEC), along with a lithium containing salt (often as $LiPF_6$) and sacrificial additives for improving electrode stability and battery safety [3].

Surprisingly little has been reported about separating electrolyte mixtures in lithium ion batteries for characterization of these dynamic systems. Recently, gas chromatography methods have been reported to provide good separation and characterization of the electrolyte family of organic carbonates in lithium ion batteries [4]. However, conventional gas chromatography methods for organic compounds, require flame ionization detection methods that typically pyrolize and destroy the analyte, leaving it excellent for *in situ* analysis, but poor for yielding separated analytes for follow up analysis. Gas chromatography methods also require high injector temperatures of around 230 °C to maintain a gas vapor [4a, 4d]. This can be a major instrumentation challenge when working with battery electrolytes because the common lithium salt, $LiPF_6$, decomposes into caustic HF and PF_5 at temperatures above 107 °C [4a, 5]. For this reason, a liquid-liquid extraction of the organic carbonates from the electrolyte salt solution has been recommended and is highly desirable, resulting in gas chromatography often being used as a semi-quantitative characterization method [4a].

Few studies have been reported on the characterization and separation and of lithium ion battery electrolytes using high performance liquid chromatography (HPLC), which is generally considered as non-destructive to the separated analytes and complementary to gas chromatography. Although problematic at high temperatures, the conversion reaction of $LiPF_6$ in the electrolyte to HF and OPF_3 is slightly endothermic [5] with a decomposition temperature in water of 70 °C [6]. $LiPF_6$ is known to react with water impurities in battery electrolytes to generate HF[7] However, in pure water solutions, $LiPF_6$ has been found to be quite stable by NMR studies[5], suggesting that $LiPF_6$ should be stable in the low

concentrations present during liquid chromatography. Typical HPLC methods make use of a C_{18} reversed phase silica column, which separates analytes based on their hydrophobicity. Such HPLC methods have been shown to separate the electrolyte family of carbonates under optimized conditions [8]. However, these methods require gradient pumps and mixers while offering poor resolution due to the similar hydrophobicity of electrolyte carbonates, with published methods showing ethylene, vinylene, and propylene carbonate all eluting within the first minute [8a]. Alternatively, an ion-exchange resin has been successfully applied for the characterization of ethylene and glycerol carbonate. This method has the advantages of not being a silica based column, a potential issue where HF could be involved. Additionally, this method provided excellent separation of ethylene and glycerol carbonate [9], but was not used to explore any additional battery electrolyte carbonates. Unfortunately, the CarH column by Touzard and Matignon no longer appears to be commercially available, necessitating method development on an alternative column

Herein, we report the use of an isocratic, aqueous ion-moderated-partition HPLC method for separating and identifying six organic carbonates in the common lithium ion battery electrolyte family. Considering the similar chemical structures and properties of these carbonates, we applied a polymer-based ion-exchange HPLC column that relies on multiple modes of interactions which specializes in separating and quantifying structurally similar (and frequently isomer) molecules[10]. Limits of detection (LOD) and limits of quantification (LOQ) for the six pure organic carbonates were reported for a simple refractive index detector. Effects of column temperature and mobile phase elution flow rate were studied for improving the peak resolution of the chromatograms. The developed

method was applied to identify and quantify carbonate components of the battery electrolytes from a functioning commercial lithium ion battery.

6.2 Materials and methods

Materials

Diethyl carbonate (DEC) (anhydrous, ≥ 99%), ethylene carbonate (EC) (98%), ethyl methyl carbonate (EMC) (98%), glycerol carbonate (GC) (4-hydroxymethyl-1,3-dioxolan-2-one, ≥90%), propylene carbonate (PC) (anhydrous, 99.7%) and sulfuric acid (99.999%, HPLC grade) were purchased from Sigma-Aldrich (St. Louis, MO). Dimethyl carbonate (DMC) (99+%) was acquired from Acros Organics (Bridgewater, NJ). DriSolv Methanol (anhydrous, 99.8%) was obtained from EMD Millipore (Billerica, MA). 18650 type lithium ion battery obtained from McMaster-Carr (Elmhurst, IL) All purchased chemicals were used as received. 18 MΩ·cm deionized water was generated using a Synergy filtration system (VWR, Radnor, PA). 0.2 µm polytetrafluoroethylene (PTFE) syringe filters were purchased from VWR (Radnor, PA).

Sample preparation

The calibration curves for all selected organic carbonates (DEC, DMC, EC, EMC, GC and PC) were obtained from their respective standard solutions. A stock solution of 15,000 ppm was prepared for each of the carbonates. The calibration standards were then prepared by serial dilutions of the stock solution of the respective carbonate. The concentrations of the standard solutions for the six carbonates ranged from 50 to 15,000 ppm. While the water-soluble cyclic carbonate samples (EC, GC, PC) were diluted in deionized water, the linear carbonates (DEC, DMC, EMC), on account of their low water solubility, were diluted in methanol [11]. In order to evaluate the HPLC system conditions

for best separations of the carbonates, a 100 mM solution containing all six selected organic carbonates was prepared in deionized water.

A commercial 18650 type lithium ion battery cell was disassembled so as to obtain rinses of the anode and cathode with water for evaluating the carbonate components in the battery electrolyte. The cell was first fully discharged, followed by removing the battery case and unrolling a 1-inch length segment of the cathode and anode. The segment of cathode and anode were put in separate beakers containing 25 mL water immediately after unrolling to prevent solvent evaporation. Samples were centrifuged and filtered with 0.2 μm PTFE syringe filters prior to HPLC analysis.

HPLC analysis

The high performance liquid chromatography (HPLC) analysis was conducted on a Waters instrument comprised of a Waters 717 plus auto sampler (Waters, Milford, MA), a Waters 515 pump (Waters, Milford, MA), a PerkinElmer series 200 vacuum degasser (PerkinElmer, Waltham, MA) and a Waters 410 Differential refractometer (Waters, Milford, MA). The chromatographic separations were performed using a 300 mm x 7.8 mm Aminex HPX-87H column with 9 μm particle size in conjunction with a 30 mm x 4.6 mm micro-guard Cation-H guard column cartridge (Bio-Rad Laboratories, Inc., Hercules, CA).

The organic carbonate samples were analyzed using a modified HPLC method previously developed by the National Renewable Energy Laboratory for analyzing carbohydrates [12]. The mobile phase consisted of 5 mM sulfuric acid which had been sonicated for an hour prior to passing it through the in-line degasser. An injection volume of 10 μL was maintained for all experiments. In a typical experiment, the column and the

detector were kept at 55 °C and 35 °C, respectively along with a mobile phase flow rate of 0.6 mL/min. Peak resolution studies were conducted by varying both the column temperature (35, 45 and 55°C) and the mobile phase flow rate (0.2, 0.3 and 0.6 mL/min.) while keeping the remaining parameters constant. Data acquisition was performed with Chrom Perfect Spirit Version.5.5.6 chromatography software (Justice Laboratory Software, Denville, NJ).

The limits of detection (LOD) were determined as the concentrations corresponding to a signal-to-noise ratio (S/N) of 3 and limit of quantification (LOQ) was determined as the concentrations corresponding to a S/N of 10 [13]. The noise was determined as the root mean square (RMS) noise of the baseline and the signal was obtained as the peak height using Chrom Perfect Spirit Version 5.5.6 data acquisition software.

The peak resolution (R_s) for DMC-EC was calculated by measuring the retention times and peak width at half- height of the analytes [14]

$$R_s = \frac{1.18\,(t_{EC} - t_{DMC})}{w_{1/2,DMC} + w_{1/2,EC}} \; ,$$

where R_s is the resolution for DMC-EC, t_{DMC} is the retention time of DMC, t_{EC} is the retention time of EC, $w_{1/2,\,DMC}$ is the peak width at half-height of DMC and $w_{1/2,\,EC}$ is the peak width at half-height of EC.

The capacity factor for DMC and EC was calculated on the basis of the experimental retention times of the two and the void time of the column [15]

$$k = \frac{(t_R - t_0)}{t_0} \, ,$$

where k is the capacity factor, t_R is the retention time of DMC or EC and t_0 is the retention time of the mobile phase.

6.3 Results and discussion

Calibration, detection limits and quantification limits

External standard calibration curves were employed for the quantification of six organic carbonates (DEC, DMC, EC, EMC, GC and PC). Five standard solutions covering a broad range of concentrations (50 - 15,000 ppm) were used to obtain the calibration curves. The linear regression of each calibration curve was analyzed using Microsoft Excel 2010 software. Linear relationships were found for all carbonates evaluated with R^2 > 0.9990. (Fig. 6.1) The sensitivity of this analytical method for carbonate mixtures analysis was determined by calculating the limits of detection (LOD) and limits of quantification (LOQ) of each of the carbonates. (Fig. 6.1)
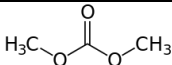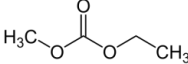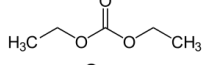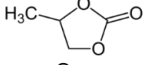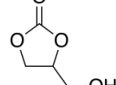
Carbonate	Abbreviation	Linear Regression	R^2	LOD (ppm)	LOQ (ppm)
	DMC	y = 510,994.4x - 910.3	0.99994	7.3	24.3
	EMC	y = 624,772.9x - 3853.2	0.99993	14.6	48.5
	DEC	y = 690,706.5x - 7,456.2	0.99912	30.8	102.7
	EC	y = 700,865.9x - 1209.4	0.99999	7.5	25
	PC	y = 912,036.5x - 2343.8	0.99992	8.2	27.2
	GC	y = 1,114,379.2x - 1,987.6	0.99997	3.8	12.7

Figure 6.1 Calibration curves, limits of detection (LOD) and limits of quantification (LOQ) for six organic carbonates: DMC, EMC, DEC, EC, PC and GC.

HPLC analysis of organic carbonates standard solution

The HPLC column employed for the separation and identification of organic carbonates is a strong cation-exchange column with a polystyrene-divinylbenzene resin backbone and exchangeable hydrogen ion (H^+) as the counter ion [16]. This column is commonly employed in the quantification of sugars, alcohols, aldehydes, ketones, organic acids and furan derivatives [10, 17]. The mechanism employed by this column for sample identification is termed as ion-moderated partition, which includes multiple modes of interactions between the analyte and the mobile and stationary phase [18]. However, to our best knowledge, the application of this column for the separation of organic carbonates has never been reported. The separation and identification of organic carbonates was initially conducted by using a simple, aqueous isocratic method originally developed for biomass analysis. A 10 μL injection of the 100 mM solution containing mixture of pure carbonates was performed on the HPLC with the column temperature maintained at 55 °C. The detector temperature was kept at 35 °C and the mobile phase flow rate was held at 0.6 mL/min. Under these conditions, in *ca.* 42 minutes, this method separated four (GC, PC, EMC, and DEC) out of six carbonates as indicated in the chromatogram in Fig. 6.2. However, DMC and EC co-eluted as a single peak. Glycerol, a common impurity found in pure GC samples, was also detected along with the carbonates. Note that though organic carbonates such as EC, PC and GC are known to be degraded in the presence of an acidic, basic additive or a salt [19], no noticeable decomposed products of these carbonates such as alcohols in the employed acidic mobile phase were detected. This further affirmed the reliability of this HPLC method.
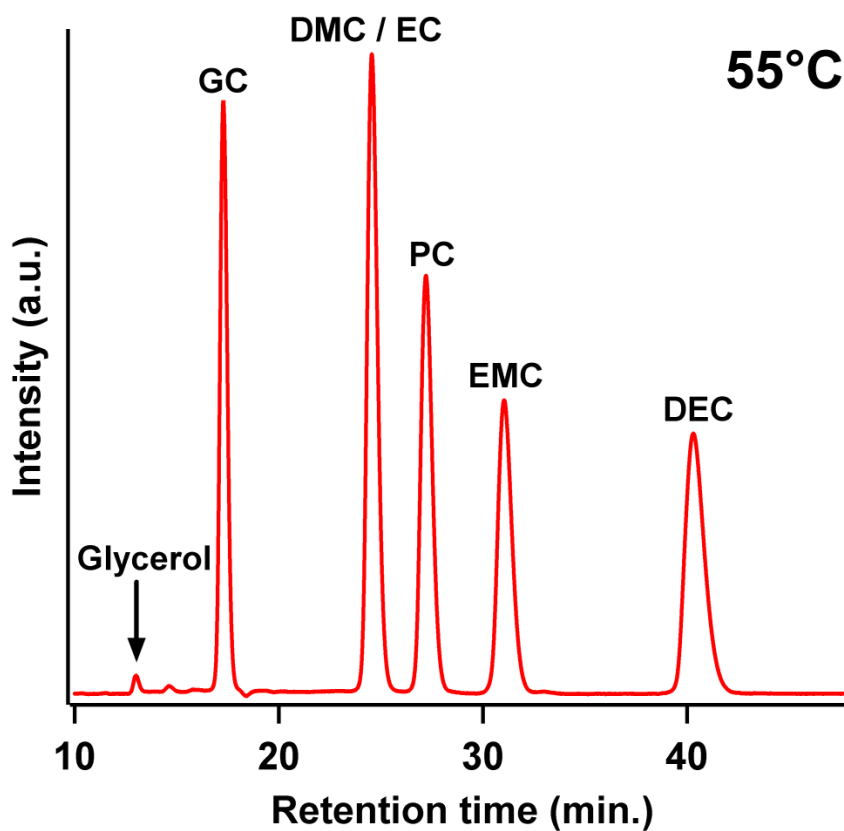
Figure 6.2 HPLC chromatogram of a 100 mM solution mixture of six organic carbonates. (GC: glycerol carbonate; DMC: dimethylcarbonate; EC: ethylene carbonate; PC: propylene carbonate; EMC: ethyl methyl carbonate; DEC: diethyl carbonate) HPLC condition– column temperature: 55 °C, detector temperature: 35 °C, mobile phase: 5mM H_2SO_4, mobile phase flow rate: 0.6 mL/min. and injection volume: 10 μL.

Effect of column temperature on the elution of DMC and EC

Chromatographic variables that include column temperature and mobile phase flow rate are known to affect the separation of co-eluting peaks in organic acid metabolites [20] and biomass hydrolysate samples [21]. In order to improve the separation between DMC and EC, the effect of the change in column temperature on the resolution of these carbonates was studied at three temperatures (55 °C, 45 °C and 35 °C) while keeping the remaining conditions the same. The peak resolution (R_s) and capacity factors (k) were used to evaluate the effect of column temperature on the separation of these two analytes. A decrease in the column temperature from 55 °C to 45 °C did not improve the peak resolution of DMC and EC. However, further lowering the column temperature to 35°C resulted in the separation of these two carbonates. (Fig. 6.3) For two analytes to be baseline resolved, their R_s value should be greater than 1.5 [22]. Although DMC and EC could not be baseline resolved at 35 °C, the R_s value for the carbonate pair was improved to 0.93. The k values of analytes are known to be temperature-dependent. Conditions which may increase the difference in k values for a pair of co-eluting organic acids was claimed to enhance the separation between them [22b]. At 45 °C, the k value for the combined DMC and EC peak was 3.23. However, lowering the column temperature to 35 °C raised the k value of EC to 3.45, while that of DMC stayed the same. This likely led to the separation of EC and DMC into two different peaks.
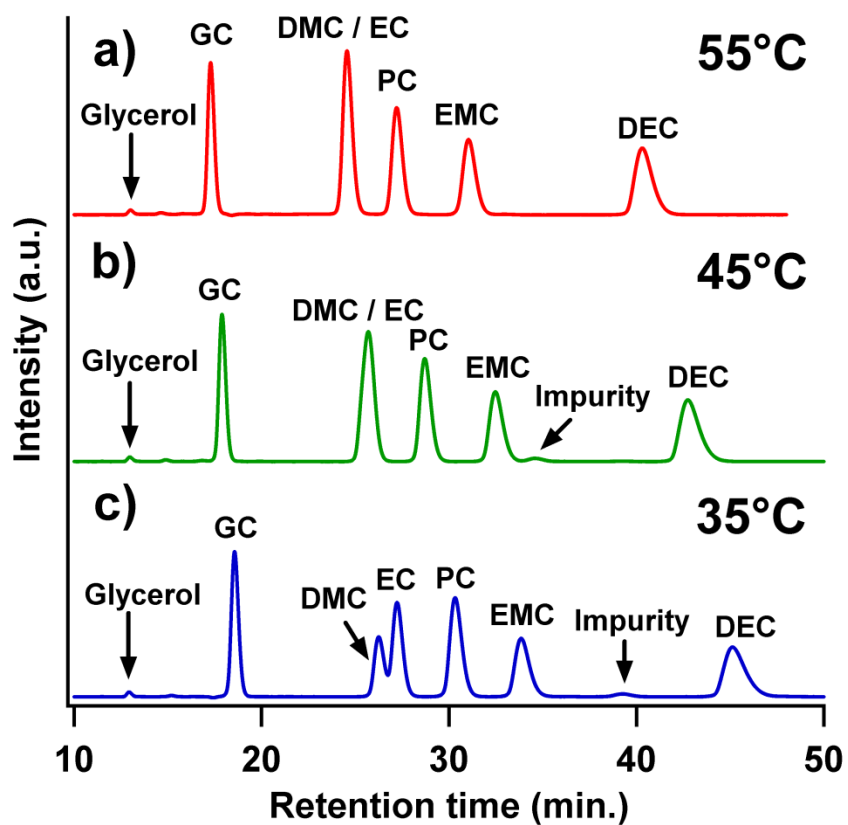
Figure 6.3 HPLC chromatograms of a 100 mM solution mixture of six organic carbonates at three different column temperatures: a) 55 °C, b) 45 °C, and c) 35 °C. HPLC conditions– detector temperature: 35 °C, mobile phase: 5 mM H_2SO_4, mobile phase flow rate: 0.6 mL/min. and injection volume: 10 μL.

The elution order of the evaluated cyclic and linear organic carbonates in our HPLC analysis was postulated to follow different carbonate-column interaction mechanisms. Among the three cyclic carbonates evaluated (EC, PC and GC), GC eluted first, followed by EC and then PC. Since GC is the most polarized molecule and PC being the least polarized one among these three carbonates, this order of elution implied that the polarity of these three carbonates governed their order of elution. Accordingly, the elution of these cyclic carbonates likely followed a reverse phase mechanism similar to the one reported in phenols separation [23]. However for the three evaluated linear carbonates, the elution of DMC was followed by EMC and then DEC. This result suggested that the elution order followed the increasing chain length of the alkyl groups in these carbonates. This in turn suggested that the separation of these linear carbonates followed a size exclusion separation mechanism. Lowering the column temperature was also found to increase band spreading. This was confirmed by the alteration in the shape of the DEC peak shape as the temperature decreased from 55 °C to 35 °C. Nevertheless, such change in column temperature only marginally affected the total analysis time which remained around 45 minutes at the three evaluated column temperatures. Note that the effects of column temperatures below 35 °C on the HPLC analysis were not evaluated because such temperatures were reported to result in the shrinkage of the column polymer backbone and damage the column [22b].

Effect of mobile phase flow rate on the elution of DMC and EC

Apart from the column temperature, mobile phase flow rate is known to affect the separation of closely eluting biomass hydroxylate compounds on the Aminex column [21, 22b]. In order to better resolve DMC and EC, studies of the mobile phase flow rate were

performed at 0.6, 0.3, and 0.2 mL/min. while the column temperature was maintained at 35 °C and the remaining conditions were kept the same. The efficiency of the separation for DMC and EC was evaluated in terms of R_s and k for these two analytes. The initial R_s value for DMC-EC at 0.6 mL/min. was found to be 0.93. A gradual decrease in the flow rate to 0.3 mL/min. marginally improved the R_s value to 1.15. The best R_s value of 1.22 was obtained at 0.2 mL/min. A complete baseline separation could not be achieved for the carbonate pair under these conditions. Nonetheless, our results demonstrated that this HPLC method can be easily employed to identify the presence of these two carbonates in an organic carbonate mixture. Since the void time of the mobile phase is inversely related to the flow rate and lowering the flow rate causes an elevation in the column void time, the k values for DMC and EC did not ameliorate much with the change in the mobile phase flow rate [24].

Identification of organic carbonates in the electrolytes of a lithium ion rechargeable battery

A major focus in lithium ion batteries (LIBs) research is the development of novel materials for electrolytes and electrodes to increase the lifetime of these batteries. The majority of electrolytes used in LIBs contain a lithium hexafluorophosphate ($LiPF_6$) salt in a solvent mixture composed of linear and cyclic carbonates [25]. Typically, these electrolytes are analyzed by destructive methods including gas chromatography [4d]. Thus, this reported HPLC method has the potential to provide a milder, non-destructive means to analyze the electrolytes of these batteries. We applied this method to analyze the organic carbonate components in the electrolytes present in the anode and cathode of a commercial LIB. In our study, DMC, EC and PC were revealed as major carbonate

components in the anode electrolyte wash whereas EC and PC constituted the major

carbonate components in the cathode electrolyte wash. (Fig.6.4) A shoulder at the

beginning of the EC peak hinted the possible presence of DMC in the cathode extract. The

difference in the peak areas of DMC in the cathode and anode electrolyte extract suggests

poor electrolyte diffusion across the separator, a feature previously observed by gas

chromatography studies of LIBs [4d]. Along with these carbonates, some unidentified

impurities and possibly additives were observed. Some negative peaks, likely due to the

difference in the composition of the sample solvent and the mobile phase [26], were also

detected in the chromatogram. Although DMC and EC could not be baseline resolved

under the current experimental conditions, this HPLC method clearly separates the two

carbonates from each other. By analyzing the peak areas in chromatogram, the ratio of

DMC: EC: PC in the anode electrolyte extract was found to be 1:5:1, v/v, while that of

EC: PC in the cathode electrolyte extract was determined to be 4:1, v/v. The amount of

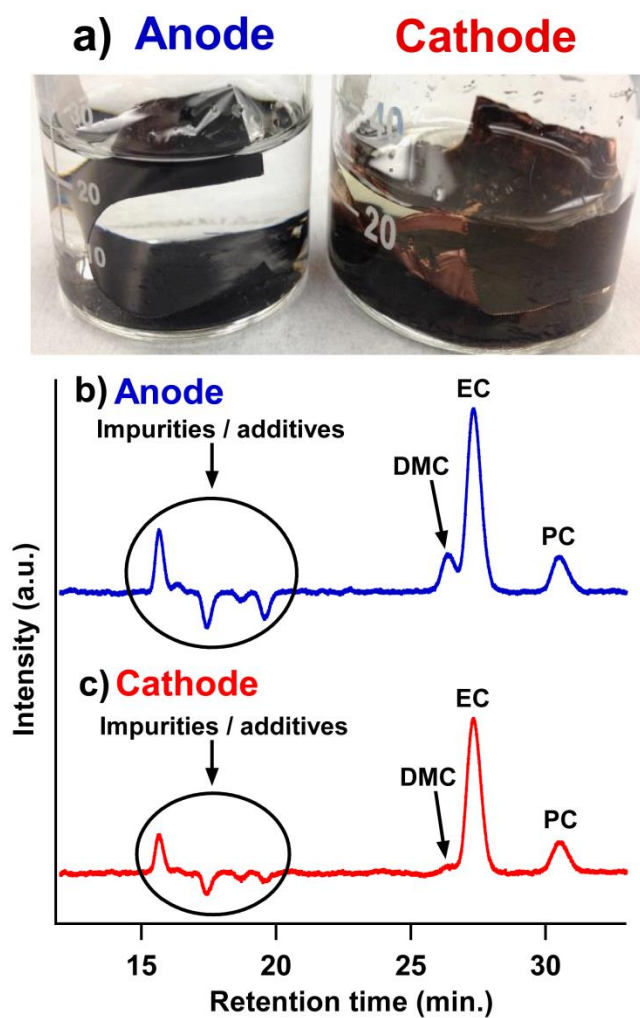DMC in the cathode washing solution was below the LOD and could not be estimated.

Figure 6.4 a) Photos of (left) an anode and (right) a cathode of a disassembled commercial lithium ion battery immersed in water. b) and c) HPLC chromatograms of electrolytes extracted from anode and cathode, respectively. HPLC condition– column and detector temperature: 35 °C, mobile phase: 5 mM H_2SO_4, mobile phase flow rate: 0.6 mL/min., and injection volume: 10 μL.

6.4 Conclusions

A new ion-moderated partition HPLC method was developed for analyzing six common organic carbonates including glycerol carbonate, dimethyl carbonate, ethylene carbonate, propylene carbonate, ethyl methyl carbonate and diethyl carbonate. This method made use of an ion-exchange HPLC column originally designed for biomass hydroxylate analysis using an isocratic, aqueous mobile phase. It needed no additional sample preparation in the form of derivatization. Since it required milder operating temperatures as compared to gas chromatography, it provided a non-destructible means to analyze carbonates which can be easily recovered and further studied in post HPLC analysis. Though this method provided quantitative separation of four of the six organic carbonates examined, a decrease in column temperature was demonstrated to be effective at qualitatively separating the remaining two carbonates. The method was illustrated to be applicable in the characterization of organic carbonates of a functional commercial lithium ion battery.

6.5 References

1.　　　Williard, N.; He, W.; Hendricks, C.; Pecht, M., Lessons Learned from the 787 Dreamliner Issue on Lithium-Ion Battery Reliability. *Energies* **2013,** *6*, 4682-4695.

2.　　　Xu, K., Electrolytes and Interphases in Li-Ion Batteries and Beyond. *Chemical Reviews* **2014,** *114*, 11503-11618.

3.　　　Etacheri, V.; Marom, R.; Elazari, R.; Salitra, G.; Aurbach, D., Challenges in the development of advanced Li-ion batteries: a review. *Energy & Environmental Science* **2011,** *4*, 3243-3262.

4.　　　(a) Petibon, R.; Rotermund, L.; Nelson, K. J.; Gozdz, A. S.; Xia, J.; Dahn, J. R., Study of Electrolyte Components in Li Ion Cells Using Liquid-Liquid Extraction and Gas Chromatography Coupled with Mass Spectrometry. *Journal of The Electrochemical Society* **2014,** *161* (6), A1167-A1172; (b) Weber, W.; Wagner, R.; Streipert, B.; Kraft, V.; Winter, M.; Nowak, S., Ion and gas chromatography mass spectroscopy investigations of organophosphates in lithium ion battery electrolytes by electrochemical aging at elevated cathode potentials. *J Power Sources* **2016,** *306*, 193-199; (c) Grutzke, M.; Kraft, V.; Hoffmann, B.; Klamor, S.; Diekmann, J.; Kwade, A.; Winter, M.; Nowak, S., Aging investigations of a lithium-ion battery electrolyte from a field-tested hybrid electric vehicle. *Journal of Power Sources* **2015,** *273*, 83-88; (d) Terborg, L.; Weber, S.; Passerini, S.; Winter, M.; Karst, U.; Nowak, S., Development of gas chromatographic methods for the analyses of organic carbonate-based electrolytes. *Journal of Power Sources* **2014,** *245*, 836-840.

5.   Yang, L.; Zhang, H.; Driscoll, P. F.; Lucht, B.; Kerr, J. B., Six-Membered-Ring Malonatoborate-Based Lithium Salts as Electrolytes for Lithium Ion Batteries. *ECS Transactions* **2011,** *33* (39), 57-69.

6.   Guo, Y., Thermal Runaway. In *Encyclopedia of Electrochemical Power Sources*, Garche, J.; Dyer, C. K.; Moseley, P. T.; Ogumi, Z.; Rand, D.; Scrosati, B., Eds. Elsevier: New York, 2009; pp 241-261.

7.   Chen, Z.; Ren, Y.; Jansen, A. N.; Lin, C.-k.; Weng, W.; Amine, K., New class of nonaqueous electrolytes for long-life and safe lithium-ion batteries. *Nature Communications* **2013,** *4*.

8.   (a) Gasgnier, M., Rare Earth Compounds (Oxides, Sulfides, Silicides, Boron, ...) as Thin Films and Thin Crystals Physico-Chemical Properties and Applications. *Physica Status Solidi (a)* **1989,** *114* (1), 11-71; (b) Cheng, H.; Gadde, R. R., Determination of Propylene Carbonate in Pharmaceutical Formulations Using Liquid Chromatography. *Journal of Pharmaceutical Sciences* **1985,** *74* (6), 695-696.

9.   Pelet, S.; Yoo, J. W.; Mouloungui, Z., Analysis of Cyclic Organic Carbonates with Chromatographic Techniques. *J. High Resol. Chromatogr.* **1999,** *22* (5), 276-278.

10.   Sluiter, A.; Hames, B.; Ruiz, R.; Scarlata, C.; Sluiter, J.; Templeton, D., Determination of sugars, byproducts, and degradation products in liquid fraction process samples. *National Renewable Energy Laboratory, Technical Report NREL/TP-510-42618* **2006**.

11.   Schäffner, B.; Schäffner, F.; Verevkin, S. P.; Börner, A., Organic carbonates as solvents in synthesis and catalysis. *Chemical Reviews* **2010,** *110* (8), 4554-4581.

12.   Bhalkikar, A.; Gernhart, Z. C.; Cheung, C. L., Recyclable magnetite nanoparticle catalyst for one-pot conversion of cellobiose to 5-hydroxymethylfurfural in water. *Journal of Nanomaterials* **2015,** *2015*, 264037.

13.   (a) Shrivastava, A.; Gupta, V. B., HPLC: isocratic or gradient elution and assessment of linearity in analytical methods. *Journal of Advanced Scientific Research* **2012,** *3* (2); (b) Shrivastava, A.; Gupta, V. B., Methods for the determination of limit of detection and limit of quantitation of the analytical methods. *Chronicles of Young Scientists* **2011,** *2* (1), 21.

14.   Calabrò, M. L.; Raneri, D.; Tommasini, S.; Ficarra, R.; Alcaro, S.; Gallelli, A.; Micale, N.; Zappalà, M.; Ficarra, P., Enantioselective recognition of 2,3-benzodiazepin-4-one derivatives with anticonvulsant activity on several polysaccharide chiral stationary phases. *Journal of Chromatography B* **2006,** *838* (1), 56-62.

15.   Alasandro, M., Separation of diastereoisomers of DuP 105, a novel oxazolidinone antibacterial agent, by supercritical fluid chromatography on a Chiralcel OD column. *Journal of Pharmaceutical and Biomedical Analysis* **1996,** *14* (7), 807-814.

16.   Blake, J. D.; Clarke, M. L.; Richards, G. N., Determination of organic acids in sugar cane process juice by high-performance liquid chromatography: improved resolution using dual aminex HPX-87H cation-exchange columns equilibrated to different temperatures. *Journal of Chromatography A* **1987,** *398*, 265-277.

17.   (a) Scarlata, C. J.; Hyman, D. A., Development and validation of a fast high pressure liquid chromatography method for the analysis of lignocellulosic biomass hydrolysis and fermentation products. *Journal of Chromatography A* **2010,** *1217* (14), 2082-2087; (b) Chen, Z.; Jin, X.; Wang, Q.; Lin, Y.; Gan, L., Confirmation and

determination of sugars in soft drink products by IEC with ESI-MS. *Chroma* **2009,** *69* (7-8), 761-764; (c) Soleimani, M.; Tabil, L., Simultaneous quantification of carbohydrates, alcohols, and toxic components in a bio-based medium using dual-detection HPLC analysis. *American Journal of Analytical Chemistry* **2013,** *4* (5), 265-272.

18.   Jupille, T.; Gray, M.; Black, B.; Gould, M., Ion moderated partition HPLC. *American Laboratory* **1981,** *13* (8), 80-&.

19.   Gaetano, F. D. A. Organic cyclic carbonates. Dec. 21. 1965, 1965.

20.   Bell, D. J.; Blake, J. D.; Prazak, M.; Rowell, D.; Wilson, P. N., Studies on yeast differentiation using organic acid metabolites Part 1. Development of methodology using high performance liquid chromatography. *Journal of the Institute of Brewing* **1991,** *97* (4), 297-305.

21.   Pecina, R.; Bonn, G.; Burtscher, E.; Bobleter, O., High-performance liquid chromatographic elution behaviour of alcohols, aldehydes, ketones, organic acids and carbohydrates on a strong cation-exchange stationary phase. *Journal of Chromatography A* **1984,** *287*, 245-258.

22.   (a) Péter, A.; Péter, M.; Ilisz, I.; Fülöp, F., Comparison of column performances in direct high-performance liquid chromatographic enantioseparation of 1- or 3-methyl-substituted tetrahydroisoquinoline analogs. Application of direct and indirect methods. *Biomedical Chromatography* **2005,** *19* (6), 459-465; (b) Xie, R.; Tu, M.; Wu, Y.; Adhikari, S., Improvement in HPLC separation of acetic acid and levulinic acid in the profiling of biomass hydrolysate. *Bioresource Technology* **2011,** *102* (7), 4938-4942.

23.   Wood, R.; Cummings, L.; Jupille, T., Recent developments in ion-exchange chromatography. *Journal of Chromatographic Science* **1980,** *18* (10), 551-558.

24. Snyder, L. R.; Kirkland, J. J.; Glajch, J. L., *Practical HPLC method development*. John Wiley & Sons: New York, 2012.

25. Scrosati, B.; Garche, J., Lithium batteries: Status, prospects and future. *Journal of Power Sources* **2010,** *195* (9), 2419-2430.

26. Snyder, L. R.; Kirkland, J. J.; Dolan, J. W., *Introduction to modern liquid chromatography*. John Wiley & Sons: New York, 2011.

Chapter 7

KINETIC AND MECHANISTIC INVESTIGATIONS OF THE DIRECT SYNTHESIS OF DIMETHYL CARBONATE FROM CARBON DIOXIDE OVER CERIA NANOROD CATALYSTS

7.1 Introduction

The direct synthesis of dimethyl carbonate (DMC) from carbon dioxide (CO_2) and methanol (MeOH) has drawn intense interest because both chemicals are abundant, renewable and relatively inexpensive. CO_2 is an abundant carbon waste which is produced on the order of billions of metric tons in the U.S. from burning fossil fuels for energy. [1] Methanol is primarily produced from the methane component of natural gas, of which there are over 350 trillion cubic feet of confirmed reserves in the United States alone. [2] In addition, methanol is also commercially produced directly from CO_2 and water or hydrogen. [3] Thus, the direct synthesis of DMC from CO_2 and methanol has the potential to remove three moles of CO_2 for every mole of DMC formed. DMC is of particular interest as it is a ready plug-in commercial chemical used both as electrolyte solvent for lithium ion batteries (for which there is a market for ~20 thousand tons per year) [4] and as an attractive green feedstock for polycarbonate plastics (which have a current world demand of ~4.5 million tons). [5] Consequently, the direct conversion of CO_2

and methanol to DMC has attracted considerable attention for both environmental and commercial reasons.

Numerous catalysts have been explored for the direct conversion of CO_2 and methanol to DMC. These catalysts include $Co_{1.5}PW_{12}O_{40}$,[6] K_2CO_3,[7] KOH,[7] ZrO_2,[8] and CeO_2.[9] As an excellent catalyst support with both Lewis acid and base properties, ceria in particular has been extensively studied after doping with Al_2O_3,[9c] ZrO_2, Ga_2O_3, Ni_2O_3, Fe_2O_3, and other lanthanide elements.[10] Unfortunately, the direct conversion of CO_2 to DMC reported in literature remains characterized by low yields (up to 7.2%[8]) at high temperatures (80-200 °C[7][6]) and long reaction times of 3[10] to 10 hours[7], limited by the thermodynamic stability of CO_2.[6][11] To improve product yields, dehydrating agents such as orthoesters, and molecular sieves have been explored for this synthetic route.[12] However, orthoesters are expensive and difficult to recover. Furthermore, the life time of molecular sieves for dehydration reaction can be short, on the order of hours.[13] Such a short life time makes it necessary for molecular sieves to be continuously replaced and regenerated for large scale processes, a costly concern for industry and an environmental concern if net CO_2 is generated.

Determining the mechanistic kinetics in the direct synthesis of DMC has the potential to inspire improved catalyst design, thereby decreasing the activation energy barrier and mitigating the problems of long reaction times and high reaction temperatures. Unfortunately, such kinetic studies are made difficult by the very same long reaction times, high pressures, and extremely anhydrous conditions which the kinetics are being studied in order to resolve. Since the initial amount of water on the reactor walls, tubes, catalyst, and gas cylinder cannot be measured before every run, the

very low product yields of DMC and water typical for this reaction can result in significant deviation in the equilibrium product yield depending on the initial conditions. As a result, previous kinetic models based on modeling the reaction profile have shown good agreement between the simulation and the experimental data in the initial rate region, but with larger deviations later in the reaction (after 5-25 hours) when close to equilibrium conditions. [9d] Additionally, experiments and simulations for the kinetics of alcohol and CO_2 reactions are difficult because these reactions have a significant activation volume ($\Delta v^{\#}$), which describes the impact of pressure on the rate constant similar to how activation energy relates temperature and rate. [9d] Hence, a small leak or a slight water contamination will result in a dramatically different reaction profile than had the depressurization not occurred, making reaction rate modeling difficult for this system.

Here we report our detailed study of the kinetics for the conversion of CO_2 and methanol into DMC using ceria nanorods as the catalyst. As the synthesis of DMC from CO_2 and methanol is a slow reaction, we focus on utilizing the initial rates of conversion in order to determine the reaction order with respect to ceria and methanol concentrations. Provided that care is taken to maintain a constant reaction pressure, a method of initial rates is found to be effective at isolating the parameters that impact the rate from those that affect the equilibrium. Additionally, the high surface area of the ceria nanorods used in this study allowed for a reduced activation energy compared to that used previously for the synthesis of DMC, [9d] allowing for reasonable rates with small catalyst loading.

7.2 Materials and methods

Synthesis of ceria nanorods

Ceria nanorod catalysts were prepared using a modified, reported hydrothermal method [14] that incorporated a lengthened calcination time to ensure the dryness of the catalysts. Briefly, 0.5 g of cerium (III) sulfate hydrate (Sigma-Aldrich) was mixed with 40 mL of a 10 M sodium hydroxide (Sigma-Aldrich) aqueous solution in a 50 mL Teflon autoclave liner. This Teflon liner was sealed in a stainless steel autoclave bomb (Parr 4744, Moline, IL) and placed in a convection oven for 15 hours at 120 °C. The solid product was vacuum-filtered through 3.0 μm polycarbonate membrane filters (EMD Millipore) and dried for 1 hour at 50 °C on the membrane. Afterwards, the catalyst was separated from the filter membrane, pulverized, and dried for an additional hour at 50 °C. The rods were then mixed with 100 mL of 15% aqueous hydrogen peroxide (Macron) solution and the resulting mixture was sonicated for 30 minutes. After an additional hour of stirring, the ceria catalyst was again vacuum-filtered through 3.0 μm polycarbonate membrane filters and dried overnight in a convection oven at 50 °C. Finally, the catalyst was calcined under pure oxygen by placing on a quartz boat in the center of a 1"-quartz tube furnace. The system was isolated from atmosphere by a glass double bubbler using Fomblin oil (Solvay). 500 SCCM of 99.6% extra dry oxygen (Matheson Tri-Gas) was continuously supplied during calcination. The sample was heated to 400 °C over 30 minutes, and held for 4 hours before being allowed to slowly cool to room temperature.

Evaluation of catalyst performance

Catalyst performance was evaluated based on the conversion of CO_2 and methanol to dimethyl carbonate (DMC) in a high pressure stainless steel reactor (Parr 4560, Moline, IL). (Figure 7.1) In a typical reaction, 0.10 grams of previously prepared catalyst was weighed out and placed in an 80 °C drying oven for 1 hour of drying. Since water is a byproduct of the formation of DMC, care must be taken to avoid the addition of any additional water. For that reason, the reactor head was purged with CO_2 (99.99% purity Matheson Tri-gas) and heated to 80 °C via a heat gun before each reaction. The steel reactor vessel was likewise heated in a drying oven to at least 80 °C for 1 hour prior to the reaction. After heating, the catalyst and reactor vessel were allowed to cool to near room temperature in a DriRite filled glass desiccator. After cooling, 15 mL of anhydrous methanol (DriSolv, EMD Millipore) and the 0.1 gram of dried catalyst were combined promptly in the reactor prior to reactor sealing. The methanol utilized had a manufacturer certified water content below 60 ppm. Methanol dryness was maintained by extracting under dry nitrogen and periodically monitored by HPLC.
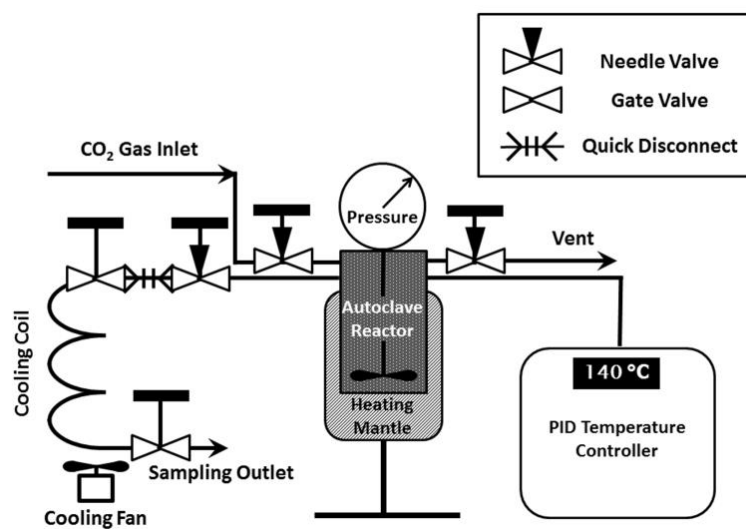
Figure 7.1 Schematic diagram of the experimental set up used in this study. Reactor was pressurized with a direct connection to a compressed CO_2 gas tank.

CO_2 pressurization was optimized such that the reactions took place at a constant 2000psi reaction pressure regardless of reaction temperature. If the reaction was to be performed at 140 °C, the reactor was pressurized with CO_2 such that the pressure held at 800 psi at 22 °C. If the reaction temperature was below 140 °C, the sealed reactor was chilled using a water-ice slurry to the desired temperature (e.g. 6 °C for a 125 °C reaction temperature) and pressurized with CO_2. This ensured that the reaction pressure remained a constant 2000 psi (138 bar) regardless of the reaction temperature. The sealed and pressurized assembly was then heated to the reaction temperature with constant stirring. As CO_2 is known to be in the supercritical state above 74 bar and 31 °C, and CO_2 is the reaction solvent, we do not expect there to be an issue with mass transport between phases. This lack of a mass transport limitation has been confirmed by previous studies where no apparent reaction profile differences were found with regard to the stirring speed. [9d, 11] Also, we evaluated the use of a baffle insert to improve the reactant mixing and the insert was found to have no observable effects on the experimental results. The reactor was held at the desired temperature (±1 °C) and 2000±100 psi for the specified reaction time. Afterwards, the heating mantle was removed and the reactor was cooled rapidly by a small fan before being carefully vented over ~20 minutes in order to avoid liquid loss. After fully depressurizing the reactor, the liquid product was collected for chemical analysis. The catalyst was separated from the carbonate sample by centrifugation and the liquid product was filtered using 0.2 μm PTFE syringe filters (VWR) prior to analysis.

GC-MS method for identification of reaction products

The identity of our major reaction product was determined to be DMC by using gas chromatography-mass spectrometry (GC-MS). For GC analysis, the oven (Thermo

Scientific Focus with PolarisQ MS, Waltham, MA) temperature was ramped from 80 to 250 °C at 20 °C/min. Inlet temperature was kept at 120 °C and helium was used as the carrier gas. The injection volume was 1 µL carried out in splitless mode. The mass spectrometer detector was operated in electron ionization mode. The presence of DMC in the reaction products was verified via characteristic electron ionization fragments at 45 and 59 m/z in the MS data.

HPLC method for quantification of reaction products

The methanol and DMC content of our reaction products were analyzed using a high performance liquid chromatography (HPLC) method developed by the National Renewable Energy Laboratory. [15] Briefly, 10 µL of filtered analyte was injected into the HPLC instrument (Waters, Milford, MA). The mobile phase used was 0.005 M sulfuric acid (99.999% HPLC grade, Sigma-Aldich) with a flow rate of 0.6 mL/min. An Aminex HPX-87H (Bio-Rad Laboratories Inc., Hercules, CA) sugars and alcohols column heated at 55 °C was used to separate DMC (retention time 24.7 minutes) from methanol (retention time 18.6 minutes). The separated components were detected using a Waters 410 Differential Refractometer (Waters, Milford, MA) held at 35 °C. The assignment of DMC and methanol were confirmed both based on retention time using DMC (Acros Organics, 99+% extra dry) and methanol references. The concentration of DMC in the product mixture was determined by integrating the area of the peak at 24.7 minutes and comparing the resulting area with external DMC standards.

Physical characterization of the catalysts

The crystal structure of the as-synthesized catalyst samples was determined using powder X-ray diffraction (PANalytical Empyrean, Westborough, MA) using a Cu Kα source with an average wavelength of 1.544 Å. Diffraction peak assignments were indexed using the ICDD data card #04-016-6171. The surface area was measured by Brunauer-Emmett-Teller (BET) analysis using a Micromeritics ASAP 2460 surface area and porosity analyzer (Micromeritics, Norcross, GA) and nitrogen. Morphological analysis of the catalyst micro and nanoscale structure was made by transmission electron microscopy (TEM; Hitachi H7500, Pleasanton, CA) operating at 80 kV.

7.3 Results and discussion

Structural characterization of the catalysts

The morphological and atomic structure of the as-synthesized ceria nanorods catalyst was studied by transmission electron microscopy (TEM) and powder X-ray diffraction (XRD). Our TEM analysis revealed that the synthesized nanorods had a range of lengths from ~50 to a few hundred nanometers. (Figure 7.2a and b) Due to their one-dimensional structures, even when the nanorods stick together, the resulting agglomerate remained porous instead of close packed. (Figure 7.2a) As shown in the XRD pattern in Figure 7.2c, the crystal structure of these ceria nanorods is well-matched to that of fluorite-structured CeO_2. No diffraction peaks due to impurities were detected by XRD. The relatively broad peak widths are characteristic of nanoscale crystallites. Note that the 3-dimensional network structures of nanorods allowed them to have a large BET surface area of 82.24 ± 0.13 m^2/g even after calcining for 4 hours at 400 °C.
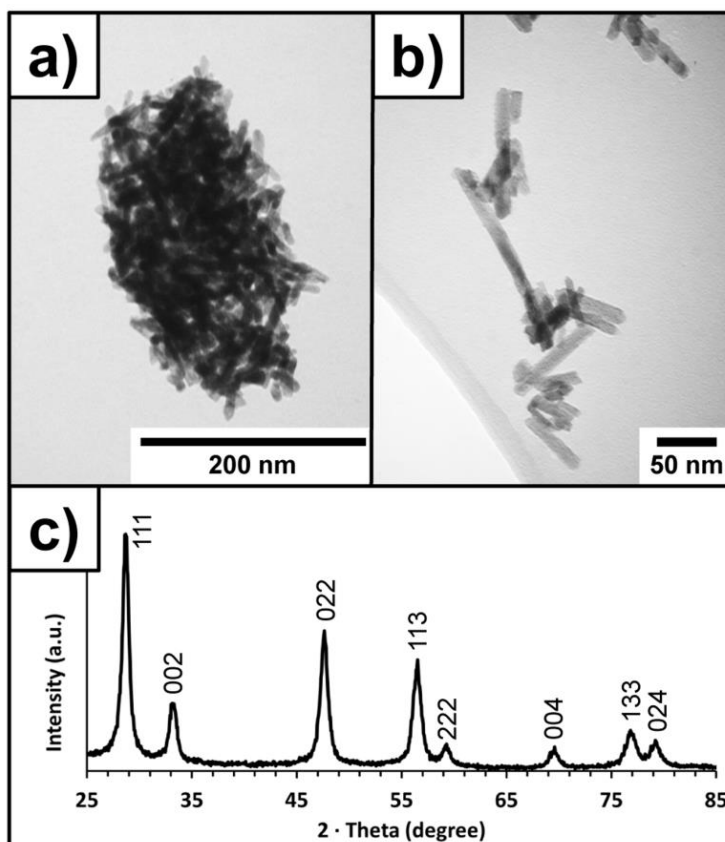
Figure 7.2 (a) TEM image of a typical ceria nanorod agglomerate. Note the large pores that remain present as a consequence of the large aspect ratio of the rods. (b) TEM image of isolated nanorods after sonication for dispersion. (c) XRD pattern of the ceria nanorods used in this study. All peaks present match to those of fluorite-structured CeO_2.

This BET surface area of nanorods only slightly decreased to 76.6 ± 0.11 m^2/g after their use for catalysis (125 °C and 2000 psi for 1 hour with 15 mL methanol). Such a small decrease of catalyst surface area demonstrates the excellent robustness of the nanorod catalysts to the pressures utilized in this study.

Effect of temperature on the reaction profile

From a thermodynamic standpoint, the conversion of CO_2 and methanol to DMC is expected to be unfavorable at high temperatures.

Eq. 1) $CO_{2\,(g)} + 2CH_3OH_{(l)} \rightleftarrows CH_3OCOOCH_{3\,(l)} + H_2O_{(l)}$
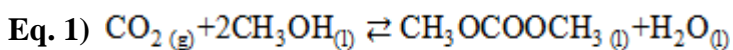
From Eq. 1, the overall reaction results in a large decrease in entropy (ΔS) both in terms of three moles of reactants forming two moles of products, as well as from the overall change from gas and liquid reagents to purely liquid products. This is characteristic of all CO_2 (gas) to organic carbonate (liquid) reactions. Fortunately, the enthalpy change (ΔH) is also negative (-20 kJ/mol [9d]), making the overall direct synthesis of DMC an enthalpy driven process. Although the system is not quite a constant pressure process, it is helpful to think of the system in terms of Gibbs free energy (ΔG) in accordance with equation 2:

Eq. 2) $\Delta G = \Delta H - T\Delta S$

Since a reaction is only spontaneous when ΔG is negative, a negative ΔH and a negative ΔS suggest that the reaction only favors products at low temperatures. To examine this deduction, we prepared a series of direct DMC synthesis experiments at two different reaction temperatures (125 and 140 °C) but with consistent amounts of methanol (15 mL) and ceria nanorod catalyst (0.10 g) in order to compare the reaction profiles with respect

to temperature (Figure 7.3). Although our reactor was equipped with a sampling coil, we found that the decrease in pressure with each sampling (~100 psi drop) impacted the overall equilibrium value of DMC. Sampling multiple data points in series would have a drastic impact on the reaction profile because the vented CO_2 could not be restored. Instead of sampling a series of data points from a single run, the reaction profiles shown in Figure 7.3 are reconstructed from the end product concentrations observed from 24 separate experiments. As illustrated in Figure 7.3, the reaction profiles at both temperatures show a linear initial region, followed by an apex as the equilibrium DMC concentration is approached. As predicted from thermodynamics, a reduced reaction temperature leads to a higher equilibrium product concentration. However, given enough time at elevated temperatures, the DMC concentration begins to decrease instead of simply plateauing.
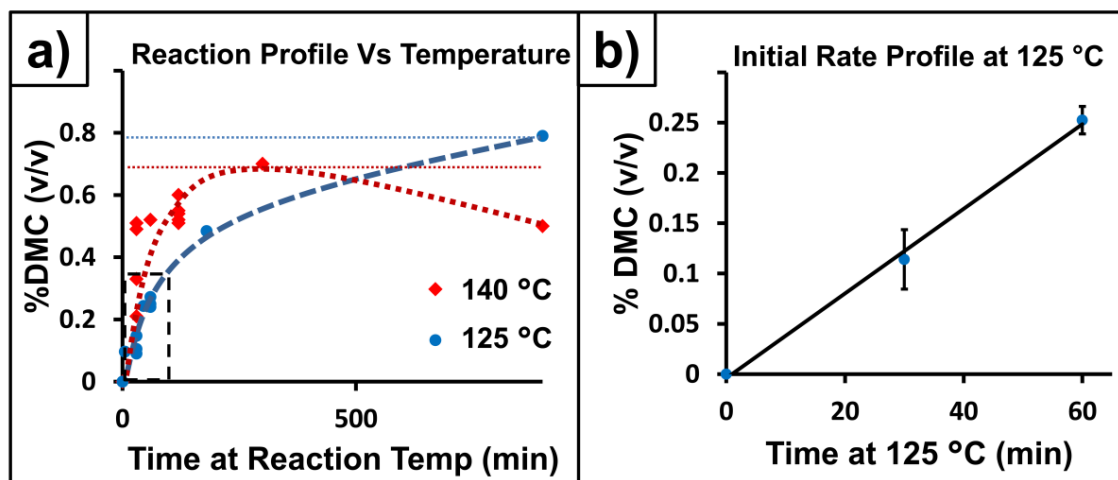
Figure 7.3 (a) Concentration of DMC product in percent by volume versus reaction time at (red diamonds) 140 °C and (blue dots) 125 °C. All 24 reaction runs shown were performed with 0.10 g of ceria, 15 mL of methanol and a reaction pressure of 2000 ± 100 psi. Each data point is from a separate reaction run. Dashed line box shows the initial rate region used for this study. (b) Reaction profile at 125 °C showing the linear initial rate profile. Data points shown are the average concentrations from reactions of 30 and 60 minutes long. Error bars are one standard deviation.

From our HPLC analysis, this observation was attributed to a slow formation of at least one major side product as seen in Figure 7.4. Such a phenomenon was previously observed and discussed in the formation of DMC from carbon monoxide and methanol by Anderson *et al.* [16] The side product observed at 13.3 minutes was largely visible as a consequence of the excellent limits of detection (down to 4 ppm for organic carbonates) made possible by the ion-moderated partition high performance liquid chromatography (HPLC) method utilized for the sample analysis. [17] Furthermore, this HPLC method allowed for low (55 °C column) temperatures for the analysis and thus allowed us a better opportunity to observe volatile or fragile side products than when the samples were analyzed by GC-MS.
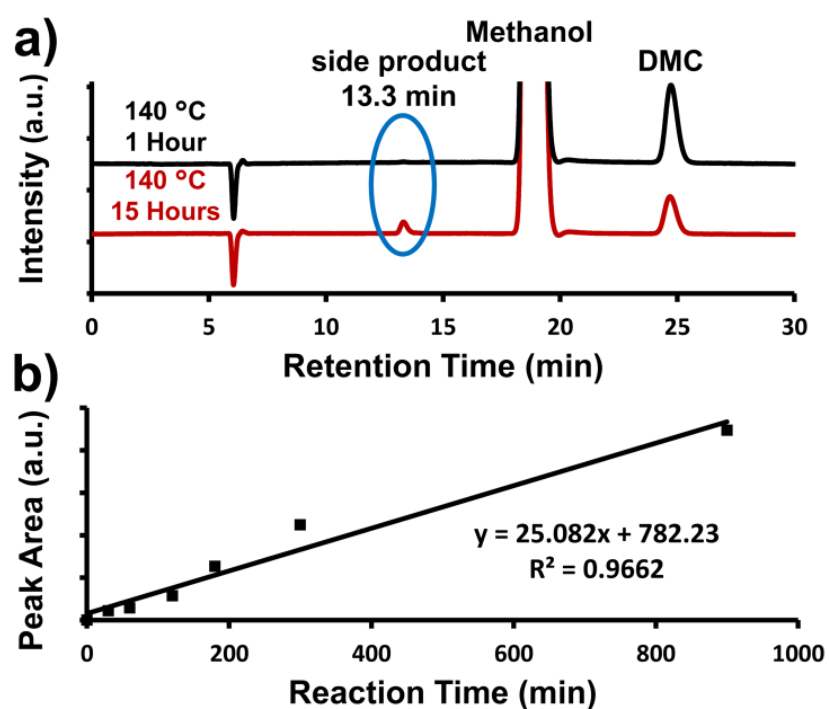
Figure 7.4 (a) HPLC chromatograms of product mixtures from the direct synthesis of DMC with ceria nanorods catalysts at 140 °C after reaction times of 1 hour and 15 hours. Note that the increasingly large side product peak is visible at the retention time of 13.3 minutes. (b) Kinetics for the side product identified at 13.3 minutes. Peak area increases largely linearly with respect to time at 140 °C.

As shown in Figure 7.4, the concentration of the observed side product increased linearly with reaction time, suggesting that its production followed a pseudo-zeroth order reaction. While the formation of this side product was trivial in the initial rate region for the reaction, the continued formation of side products significantly impacts the reaction profile once DMC production slows as equilibrium is neared and leads to a gradual decrease in DMC yield over time. This introduces complexity to the overall reaction profile, again highlighting the importance of acquiring kinetics information from the relatively clean initial rate region.

From Figure 7.3, a decrease in temperature of merely 15 °C is enough to half the initial rate for the reaction from 0.0087 %DMC/min to just 0.0042 %DMC/min. Since the reaction profile at 140 °C stays linear for only the first 30 minutes and well past 60 minutes for temperatures below 140, the initial rate was measured at 120, 125, 130, and 140 °C by collecting samples at 30 and 60 minutes. The results are summarized in the Arrhenius plot in Figure 7.5.
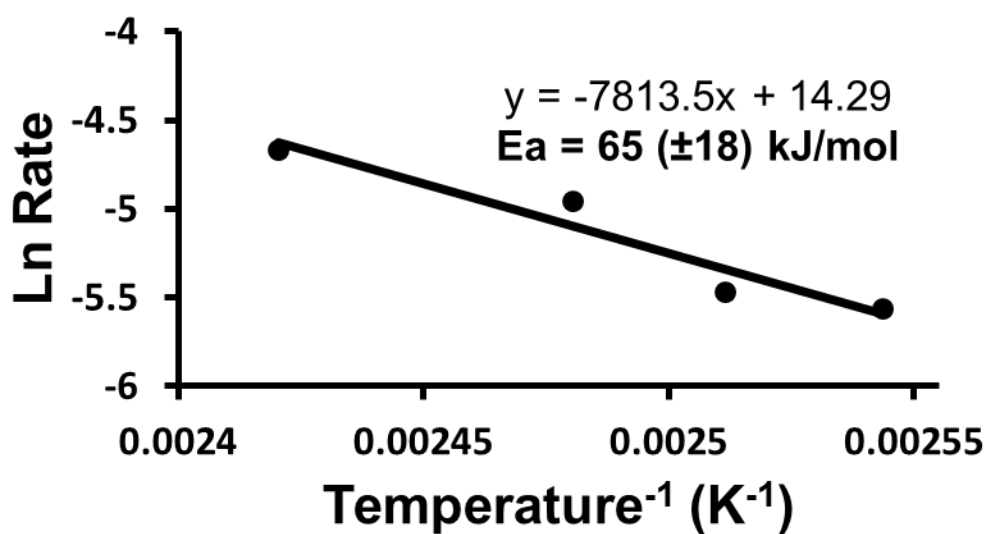
Figure 7.5 Arrhenius plot composed of initial rate data at 140 °C, 130 °C, 125 °C and 120 °C for the direct synthesis of DMC with ceria nanorod catalysts. The activation energy (Ea) of this reaction was found to be 65 ± 18 kJ/mol. Error range at the 70% confidence interval.

A linear fit of the Arrhenius plot shows a slope of -7813.5, which indicated an activation energy of 65 ± 18 kJ/mol, while the y-intercept indicates a pre-exponential factor of 1.6×10^6. This value of activation energy is far lower than the activation energy (106 kJ/mol) previously reported for a non-nanostructured ceria catalyst. [9d] However, 65 kJ/mol is still a substantial activation barrier. Consequently, reaction conditions have to be chosen as a compromise between low yields at fast rates with high temperatures, or theoretically higher yields at lower temperatures that nonetheless are never obtained due to poor kinetics.

Initial rate kinetic studies

In an effort to improve reaction rates at reduced reaction temperatures, we have attempted to experimentally determine the rate law equation for conversion of CO_2 and methanol (MeOH) to DMC exclusively using initial rate kinetics. The general rate equation takes the form:

Eq. 3) $\text{Rate} = k [CO_2]^a [MeOH]^b [*]_0^c$

where k is the experimental rate constant for the overall reaction, $[*]_0$ indicates the concentration of catalyst active sites, and a, b, and c are experimentally determined constants. While the rate constant is strictly controlled by the temperature, pressure, activation energy, and activation volume, the overall rate is also a function of the concentration of reactants and catalyst loading. In order to estimate the order of the reaction with respect to each reagent, we conducted a series of initial rate experiments in which the loading of ceria and amount of methanol were varied while maintaining a

constant 2000 psi reaction pressure, consistent amounts of CO_2, and a consistent reaction

temperature of 125 °C. Since the initial rate region remains well behaved and linear for

well over 60 minutes at these conditions, the reaction was stopped at 30 or 60 minutes for

each initial rate experiment and the concentration of DMC in the products was quantified

by HPLC. The results of these experiments are shown as log-log plots in Figures 7.6 and

7.7. As expected, there is a positive direct relationship between the concentrations of

catalyst in the reactor versus the initial rate as the catalyst loading is increased from 0.05

g to 0.125 g (Figure 7.6). A log-log plot of the rate versus catalyst concentration (in M)

reveals a reaction order of +0.88±0.37. Within experimental error, this is a positive first

order reaction, as expected for a heterogeneous catalyst. Surprisingly, the initial rate had

an inverse relationship with the concentration of methanol added, with a log-log plot

giving a slope of -1.18 as methanol loading increased from 10 to 30 mL. (Figure 7.7)

This indicates that methanol is competing with the reagents that are involved in the rate

controlling step, namely CO_2. As a whole, these results suggest that the observed

experimental rate equation is roughly: $\text{Rate} = k[CO_2]^{a(>0)} [*]_0^{\sim -1} [MeOH]^{\sim(-1)}$ with the

concentration of methanol likely competing for the same surface sites as CO_2 negatively
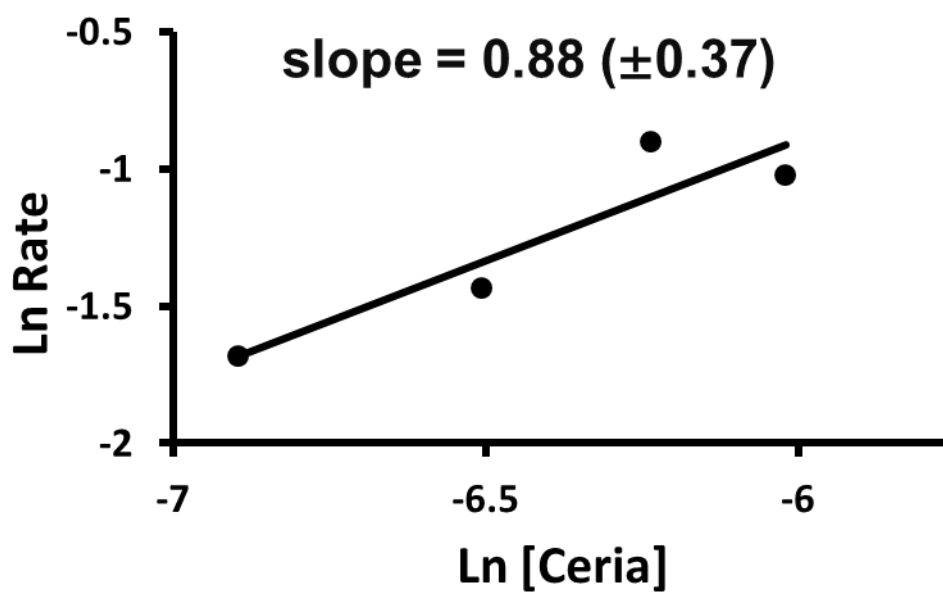
impacting the reaction rate.

Figure 7.6 Kinetics study of the initial rate of DMC production versus ceria nanorod catalyst loading. All experiments were performed using 15 mL of methanol at 125 °C and 2000 psi with the concentration of DMC sampled after a 30 minute reaction. Slope error assuming a 70% confidence interval.
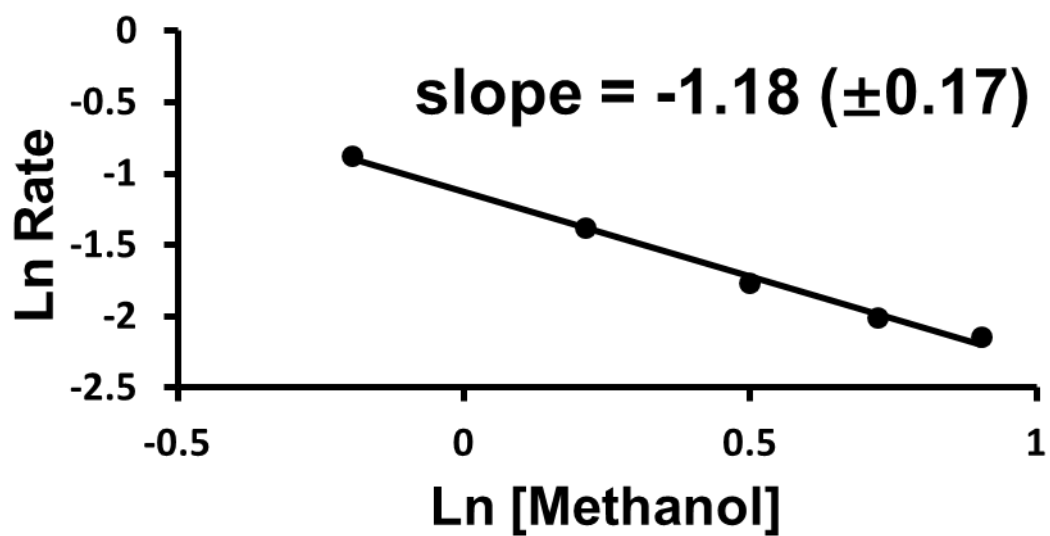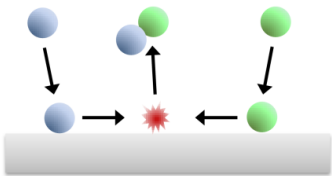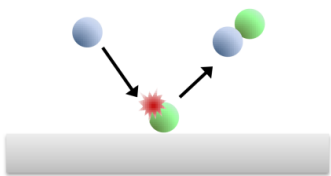
Figure 7.7 Kinetics study of the initial rate of DMC production versus methanol loading. All experiments used 0.1 g of ceria and were performed at 125 °C and 2000 psi with the concentration of DMC sampled after a one hour reaction. Slope error assuming a 95% confidence interval.

Mechanistic insights

Our kinetics studies provide experimental evidence that helps to clarify the reaction mechanism of the direct synthesis of DMC from CO_2 and methanol. The fact that the rate of the reaction is strongly impacted by the amount of catalyst present suggests that the rate controlling step in the reaction occurs on the catalyst surface. For methanol to not positively factor into the experimental rate law, the adsorption of CO_2 on the catalyst surface has to be occurring in a separate elementary step than the adsorption of methanol. This is consistent with a Langmuir-Hinshelwood (LH) type mechanism since it reveals that the CO_2 and methanol must be interacting with the catalyst in two separate steps with the CO_2 adsorption rate determining. Figure 7.8 compares two typical reaction mechanisms for heterogeneously catalyzed reactions proposed in the literature: the Langmuir-Hinshelwood (LH) mechanism and the Eley-Rideal (ER) mechanism. [9d, 11]

Shown in Figure 7.8 are the elementary steps for two previously proposed reaction mechanisms along with the apparent rate law expression that we would expect to observe if the given step were rate determining and the previous steps relatively rapid. Note that the concentration of methanol necessarily appears in the apparent rate laws for any of the later reaction steps after the adsorption of CO_2 in the LH mechanism (Step 1) while also appearing in every apparent rate law derived from the shown ER mechanism. Also note that for simplicity's sake, the rate law is still shown in terms of available catalyst sites [*]. However, changing the catalyst loading directly varies the total catalyst sites $[*]_0$ which is equal to the available catalyst sites plus the occupied catalyst sites.

Step	Langmuir-Hinshelwood (LH) mechanism		Eley-Rideal (ER) mechanism	
	Elementary reaction step	Rate law if rate determining	Elementary reaction step	Rate law if rate determining
1	$CO_2 + * \rightleftharpoons CO_2^*$	$R = k\,[CO_2]\,[*]$	$MeOH + * \rightleftharpoons MeOH^*$	$R = k\,[MeOH]\,[*]$
2	$MeOH + * \rightleftharpoons MeOH^*$	$R = k\,[MeOH]\,[*]$	$MeOH^* + CO_2 \rightleftharpoons MC^*$	$R = k\,[MeOH]\,[CO_2]\,[*]$
3	$2MeOH^* + CO_2^* \rightleftharpoons DMC^* + H_2O^* + *$	$R = k\,[CO_2]\,[MeOH]^2\,[*]^3$	$MC^* + MeOH^* \rightleftharpoons DMC + H_2O + *$	$R = k\,[CO_2]\,[MeOH]^2\,[*]^2$
4	$DMC^* \rightleftharpoons DMC + *$	$R = k\,[MeOH]\,[*]\,[CO_2]^{1/2}$		
5	$H_2O^* \rightleftharpoons H_2O + *$	$R = k\,[MeOH]\,[*]\,[CO_2]^{1/2}$		

* = available catalyst active site   MC = methyl carbonate

Figure 7.8 Elementary mechanistic steps previously proposed for the formation of DMC from CO_2 and methanol by a Langmuir-Hinshelwood and an Eley-Rideal mechanism. [9d, 11] Apparent rate law was shown for each step if the given step was significantly slower than the preceding step(s).

In order to derive the reaction rate law with respect to the total catalyst sites, a few assumptions must be made. If the adsorption of CO_2 is slow while the adsorption of methanol is fast, then the catalyst surface is likely saturated with adsorbed methanol as the most abundant reactive intermediate (*mari*). This is very similar to what is observed in the Haber process where the reaction between the relatively energetic H_2 molecule is limited by the rate of adsorption of the very stable N_2 molecule on the catalyst surface in a Langmuir-Hinshelwood mechanism. In the Haber process, such adsorption phenomena results in a positive rate order with respect to N_2, and a reaction order of -1 with respect to H_2 [18]. Similarly, if we assume that methanol is the *mari* in our system, then the total concentration of surface sites $[*]_0 \approx [MeOH^*] + [*]$. Assuming that step 1 of the LH mechanism as shown is the rate determining step, the derived rate law expression for the conversion of CO_2 to DMC is:

Eq. 4) $\text{Rate} = \dfrac{k_1\,[CO_2]\,[*]_0}{K_2\,[MeOH]+1}$

where k_1 is the rate constant for the first elementary step and K_2 is the equilibrium constant for step 2. This rate law is in excellent agreement with our initial rate kinetics with a positive reaction order with respect to the catalyst and CO_2, and a reaction order of -1 with respect to methanol. However, a detailed study of the initial rate with varying CO_2 partial pressures (but constant total pressure) is still recommended for further verification of the derived first reaction order with respect to CO_2.

The discussed initial reaction rate kinetics experiments strongly suggest that the conversion of methanol and CO_2 to DMC over ceria catalysts follows a Langmuir-Hinshelwood mechanism where the CO_2 and methanol are binding to the catalyst in

separate steps, consistent with previous kinetics studies modeling the reaction from the reaction profile. [9d] Interestingly, this result contrasts with that shown for the production of DMC from methanol and carbon monoxide over copper zeolite catalysts, which were found to have a non-negative rate order with respect to methanol and are believed to follow an ER mechanism. [19] This suggests that the production of DMC from CO_2 instead of CO may take a very different pathway for the production of DMC despite the apparent similarity of the overall reaction

7.4 Conclusions

The reaction profile and kinetics were studied for the direct conversion of CO_2 and methanol into dimethyl carbonate over ceria nanorod catalysts. The nanorod catalysts were found to have an activation energy barrier of 65±14 kJ/mol, substantially lower than the 106 kJ/mol previously reported for bulk ceria. [9d] Consistent with an enthalpy driven reaction, reduced temperatures were found to favor DMC formation, although the reaction remained limited by slow kinetics. Taking advantage of the slow reaction rates at lower reaction temperatures, a method of initial rates approach was successfully utilized. The rate order with respect to ceria was ~1 (experiment: 0.88), while that of methanol was ~ -1 (experiment: -1.2). These results are consistent with a Langmuir-Hinshelwood type mechanism where the CO_2 and methanol must first interact with the solid catalyst in two separate steps with the CO_2 adsorption step being rate controlling. These results suggest that the kinetics for the conversion of CO_2 and methanol to DMC would best be improved by (1) maximizing the surface area of the ceria catalysts, (2) reducing the energy barrier required for CO_2 adsorption, and (3) conducting the reaction with a low ratio of methanol to CO_2 in the feed gas.

7.5 References

1.   *Inventory of U.S. Greenhouse Gas Emissions and Sinks: 1990 – 2012*; Office of Atmospheric Programs, US Environmental Protection Agency.: Washington DC, 2014.

2.   *U.S. Crude Oil and Natural Gas Proved Reserves, 2014*; U.S. Energy Information Administration.: Washington, DC, 2015.

3.   (a) Shulenberger, A. M.; Ragnar, F. J.; Ingolfsson, O.; Tran, K.-C. Process for producing liquid fuel from carbon dioxide and water. 2012; (b) Li, Y.; Junge, K.; Beller, M., Improving the Efficiency of the Hydrogenation of Carbonates and Carbon Dioxide to Methanol. *ChemCatChem* **2013,** *5*, 1072-1074.

4.   Xu, K., Electrolytes and Interphases in Li-Ion Batteries and Beyond. *Chemical Reviews* **2014,** *114*, 11503-11618.

5.   (a) Haba, O.; Itakura, I.; Ueda, M.; Kuze, S., Synthesis of polycarbonate from dimethyl carbonate and bisphenol-a through a non-phosgene process. *Journal of Polymer Science* **1999,** *37* (13), 2087-2093; (b) Tundo, P.; Selva, M., The Chemistry of Dimethyl Carbonate. *Acc. Chem. Res.* **2002,** *35*, 706-716; (c) *IHS Chemical 2012 World Polycarbonate and ABS Analysis*; IHS Inc.: 2012.

6.   Aouissi, A.; Al-Othman, Z. A.; Al-Amro, A., Gas-Phase Synthesis of Dimethyl Carbonate from Methanol and Carbon Dioxide Over $Co_{1.5}PW_{12}O_{40}$ Keggin-Type Heteropolyanion. *International Journal of Molecular Sciences* **2010,** *11*, 1343-1351.

7.   Cai, Q.; Lu, B.; Guo, L.; Shan, Y., Studies on synthesis of dimethyl carbonate from methanol and carbon dioxide. *Catalysis Communications* **2009,** *10*, 605-609.

8. Eta, V.; Maki-Arvela, P.; Leino, A.-R.; Kordas, K.; Salmi, T.; Murzin, D. Y.; Mikkola, J.-P., Synthesis of Dimethy Carbonate from Methanol and Carbon Dioxide: Circumventing Thermodynamic Limitations. *Ind. Eng. Chem. Res.* **2010,** *49*, 9609-9617.

9. (a) Wang, S.; Zhao, L.; Wang, W.; Zhao, Y.; Zhang, G.; Ma, X.; Gong, J., Morphology control of ceria nanocrystals for catalytic conversion of CO_2 with methanol. *Nanoscale* **2013,** *5*, 5582-5588; (b) Yoshida, Y.; Arai, Y.; Kado, S.; Kunimori, K.; Tomishige, K., Direct synthesis of organic carbonates from the reaction of CO_2 with methanol and ethanol over CeO_2 catalysts. *Catalysis Today* **2006,** *115*, 95-101; (c) Aresta, M.; Dibenedetto, A.; Pastore, C.; Angelini, A.; Aresta, B.; Papai, I., Influence of Al_2O_3 on the performance of CeO_2 used as catalyst in the direct carboxylation of methanol to dimethylcarbonate and the elucidation of the reaction mechanism. *Journal of Catalysis* **2010,** *269*, 44-52; (d) Santos, B. A. V.; Pereira, C. S. M.; Silva, V. M. T. M.; Loureiro, J. M.; Rodrigues, A. E., Kinetic study for the direct synthesis of dimethyl carbonate from methanol and CO_2 over CeO_2 at high pressure conditions. *Applied Catalysis A: General* **2013,** *455*, 219-226.

10. Lee, H. J.; Joe, W.; Jung, J. C.; Song, I. K., Direct synthesis of dimethyl carbonate from methanol and carbon dioxide over Ga_2O_3-CeO_2-ZrO_2 catalysts prepared by a single-step sol-gel method: Effect of acidity and basicity of the catalysts. *Korean J. Chem. Eng.* **2012,** *29* (8), 1019-1024.

11. Eta, V.; Maki-Arvela, P.; Warna, J.; Salmi, T.; Mikkola, J. P.; Murzin, D. Y., Kinetics of dimethyl carbonate synthesis from methanol and carbon dioxide over ZrO2-MgO catalyst in the presence of butylene oxide as additive. *Applied Catalysis A: General* **2011,** *404* (1-2), 39-46.

12.   Stoye, D., Solvents. In *Ullmann's Encyclopedia of Industrial Chemistry*, Wiley-VCH Verlag GmbH & Co. KGaA: 2000.

13.   (a) Sun, Q.; Wang, N.; Xi, D.; Yang, M.; Yu, J., Organosilane surfactant-directed synthesis of hierarchical porous SAPO-34 catalysts with excellent MTO performance. *Chemical Communications* **2014,** *50* (49), 6502-6505; (b) Zhang, M.; Xiao, M.; Yu, Y.; Wang, S.; Choi, M. J.; Meng, Y., Synthesis of $Co_{1.5}PW_{12}O_{40}$ and Its Catalytic Performance of Completely Converting Methanol to Ethylene. *Chemical Communications* **2016,** *52*, 1151-1153.

14.   Lawrence, N. J.; Brewer, J. R.; Wang, L.; Wu, T.-S.; Wells-Kingsbury, J.; Ihrig, M. M.; Wang, G.; Soo, Y.-L.; Mei, W.-N.; Cheung, C. L., Defect Engineering in Cubic Cerium Oxide Nanostructures for Catalytic Oxidation. *Nano Letters* **2011,** *11*, 2666-2671.

15.   (a) Sluiter, A.; Hames, B.; Ruiz, R.; Scarlata, C.; Sluiter, J.; Templeton, D., Determination of sugars, byproducts, and degradation products in liquid fraction process samples. *National Renewable Energy Laboratory, Technical Report NREL/TP-510-42618* **2006**; (b) Gernhart, Z. C.; Bhalkikar, A.; Burke, J. J.; Sonnenfeld, K. O.; Marin, C. M.; Zbasnik, R.; Cheung, C. L., One-pot conversion of cellobiose to mannose using a hybrid phosphotungstic acid-cerium oxide catalyst. *RSC Advances* **2015,** *5*, 28478-28486.

16.   Anderson, S. A.; Manthata, S.; Root, T. W., The decomposition of dimethyl carbonate over copper zeolite catalysts. *Applied Catalysis C* **2005,** *280*, 117-124.

17.   Bhalkikar, A.; Marin, C. M.; Cheung, C. L., Method Development for Separating Lithium Ion Electrolyte Carbonates using Ion-Moderated Partition High Performance Liquid Chromatography. *Pending Review* **2016**.

18.   (a) Becue, T.; Davis, R. J.; Garces, J. M., Effect of Cationic Promoters on the Kinetics of Ammonia Synthesis Catalyzed by Ruthenium Supported on Zeolite X. *Journal of Catalysis* **1998,** *179*, 129-137; (b) Davis, M. E.; Davis, R. J., *Fundamentals of Chemical Reaction Engineering*. Dover Publications: Mineola, 2012.

19.   Anderson, S. A.; Root, T. W., Kinetic studies of carbonylation of methanol to dimethyl carbonate over Cu^+X zeolite catalyst. *Journal of Catalysis* **2003,** *217*, 396-405.

7.6 Supplementary information

Legend: DMC = dimethyl carbonate

MeOH = methanol

MC = methyl carbonate

$_f$ = indicating forward reaction direction

$_r$ = indicating reverse reaction direction

k_x = rate constant of elementary step x
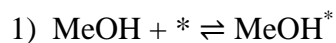
[*] = concentration of available catalyst sites

$[*]_0$ = concentration of total catalyst sites (proportional to [ceria])

$[A^*]$ = concentration of A bound to catalyst site

$[*]_0 = [*] + [A*] + [B*] + \ldots$

Derivations of Apparent Rate Laws Shown in Figure 7.8

A. Eley-Rideal Mechanism Elementary Steps from Figure 7.8

1) $MeOH + * \rightleftharpoons MeOH^*$

2) $MeOH^* + CO_2 \rightleftharpoons MC^*$

3) $MC^* + MeOH^* \rightleftharpoons DMC + H_2O + *$
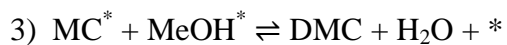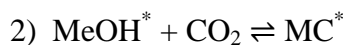
If step 1 is rate limiting:

$$\text{Rate}_f = k_{1f} [\text{MeOH}]^1 [*]^1 \qquad\qquad \text{-Rate} = r_f - r_r \approx r_f \text{ in initial rate}$$

If step 2 is rate limiting and previous steps are fast:

$$\text{Rate}_f = k_{2f} [\text{MeOH}^*]^1 [\text{CO}_2]^1 \qquad\qquad \text{-Rate} = r_f - r_r \approx r_f \text{ in initial rate}$$

$$[\text{MeOH}^*] = \frac{k_{1f}}{k_{1r}} [\text{MeOH}] [*] \qquad\qquad \text{-From equilibrium cond, in step 1}$$

$$\text{Rate}_f = \frac{k_2\, k_{1f}}{k_{1r}} [\text{MeOH}]^1 [*]^1 [\text{CO}_2]^1 \qquad\qquad \text{-Substitution}$$

$$\text{Rate} = k [\text{MeOH}] [\text{CO}_2] [*] \qquad\qquad \text{-Combine rate constants and QED}$$

If step 3 is rate limiting and previous steps are fast:

$$\text{Rate}_f = k_3 [\text{MC}^*] [\text{MeOH}^*] \qquad\qquad \text{-Rate} = r_f - r_r \approx r_f \text{ in initial rate}$$
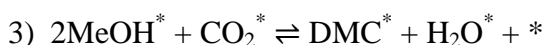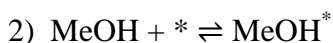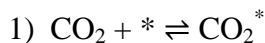
$$[\text{MeOH}^*] = \frac{k_{1f}}{k_{1r}} [\text{MeOH}] [*] \qquad\qquad \text{-From step 1 equilibrium}$$
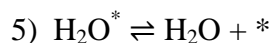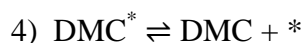
$$[\text{MC}^*] = \frac{k_{2f}}{k_{2r}} [\text{CO}_2] [\text{MeOH}^*] \qquad\qquad \text{-From step 2 equilibrium}$$

$$\text{Rate}_f = \frac{k_3 k_{2f} k_{1f} k_{1f}}{k_{2r} k_{1r} k_{1r}} [\text{CO}_2] [\text{MeOH}] [*] [\text{MeOH}] [*] \qquad \text{-Substitution}$$

$$\text{Rate} = k [\text{CO}_2] [\text{MeOH}]^2 [*]^2 \qquad\qquad \text{- Combine rate constants and QED}$$

B. Langmuir-Hinshelwood Mechanism Elementary Steps from Figure 8

1) $CO_2 + * \rightleftharpoons CO_2{}^*$

2) $\text{MeOH} + * \rightleftharpoons \text{MeOH}^*$

3) $2\text{MeOH}^* + CO_2{}^* \rightleftharpoons \text{DMC}^* + H_2O^* + *$

4) $DMC^* \rightleftharpoons DMC + *$

5) $H_2O^* \rightleftharpoons H_2O + *$

If step 1 is rate limiting:

$$Rate = k_{1f}\,[CO_2]\,[*]$$

If step 2 is rate limiting:

$$Rate = k_{2f}\,[MeOH]\,[*]$$

If step 3 is rate limiting and previous steps are fast:

$$Rate = k_{3f}\,[CO_2{}^*]\,[MeOH^*]\,[MeOH^*] \qquad \text{-Rate} = r_f - r_r \approx r_f \text{ in initial rate}$$

$$[CO_2{}^*] = \frac{k_{1f}}{k_{1r}}\,[CO_2]\,[*] \qquad \text{-From equilibrium cond. in step 1}$$

$$[MeOH^*] = \frac{k_{2f}}{k_{2r}}\,[MeOH]\,[*] \qquad \text{-From equilibrium cond. in step 2}$$

$$Rate = \frac{k_3 k_{2f} k_{2f} k_{1f}}{k_{1r} k_{2r} k_{2r}}\,[CO_2]\,[*]\,[MeOH]\,[*]\,[MeOH]\,[*] \quad \text{-Substitution}$$

$$Rate = k\,[CO_2]\,[MeOH]^2\,[*]^3 \qquad \text{- Combine rate constants and QED}$$

If step 4 is rate limiting and previous steps are fast:

$$Rate = k_{4f}\,[DMC^*] \qquad \text{-Rate} = r_f - r_r \approx r_f \text{ in initial rate}$$

$$[DMC^*]\,[H_2O^*] = \frac{k_{3f}}{k_{3r}}\,\frac{[MeOH^*]^2\,[CO_2{}^*]}{[*]} \qquad \text{-From equilibrium cond. in step 3}$$

$$[DMC^*]\,[H_2O^*] = \frac{k_{3f} k_{2f} k_{2f} k_{1f}}{k_{3r} k_{2r} k_{2r} k_{1r}}\,\frac{[MeOH]^2\,[*]^2\,[CO_2][*]}{[*]}$$

$[DMC^*] = [H_2O^*]$ -If no H_2O^* source other than step 3

$$[DMC^*]^2 = \frac{k_{3f}k_{2f}k_{2f}k_{1f}}{k_{3r}k_{2r}k_{2r}k_{1r}} [MeOH]^2 [CO_2] [*]^2 \qquad \text{-Substitution}$$

$$[DMC^*] = \frac{k_3^{1/2}k_2k_1^{1/2}}{k_3^{1/2}k_2k_1^{1/2}} [MeOH] [CO_2]^{1/2} [*] \qquad \text{-Square root of both sides}$$

$$Rate = \frac{k_{4f}k_{3f}^{1/2}k_{2f}k_{1f}^{1/2}}{k_{3r}^{1/2}k_{2r}k_{1r}^{1/2}} [MeOH] [CO_2]^{1/2} [*] \qquad \text{-Substitution}$$

$$Rate = k [MeOH] [*] [CO_2]^{1/2} \qquad \text{- Combine rate constants and QED}$$

If step 5 is rate limiting and previous steps are fast:

$$Rate = k_{5f} [H_2O^*] \qquad\qquad\qquad \text{-Rate} = r_f - r_r \approx r_f \text{ in initial rate}$$

$$[DMC^*] [H_2O^*] = \frac{k_{3f}}{k_{3r}} \frac{[MeOH^*]^2 [CO_2^*]}{[*]} \qquad \text{-From equilibrium cond. in step 3}$$

$$[DMC^*] [H_2O^*] = \frac{k_{3f}k_{2f}k_{2f}k_{1f}}{k_{3r}k_{2r}k_{2r}k_{1r}} \frac{[MeOH]^2 [*]^2 [CO_2][*]}{[*]} \text{-From equilibrium cond. steps 1, 2}$$

$[DMC^*] = [H_2O^*]$ -If no H_2O^* source other than step 3

$$[H_2O^*]^2 = \frac{k_{3f}k_{2f}k_{2f}k_{1f}}{k_{3r}k_{2r}k_{2r}k_{1r}} [MeOH]^2 [CO_2] [*]^2 \qquad \text{-Substitution}$$

$$[H_2O^*] = \frac{k_3^{1/2}k_2k_1^{1/2}}{k_3^{1/2}k_2k_1^{1/2}} [MeOH] [CO_2]^{1/2} [*] \qquad \text{-Square root of both sides}$$

$$Rate = \frac{k_{5f}k_{3f}^{1/2}k_{2f}k_{1f}^{1/2}}{k_{3r}^{1/2}k_{2r}k_{1r}^{1/2}} [MeOH] [CO_2]^{1/2} [*] \qquad \text{-Substitution}$$

$$Rate = k [MeOH] [*] [CO_2]^{1/2} \qquad \text{- Combine rate constants and QED}$$

C. Addendum to Langmuir-Hinshelwood Mechanism from Figure 7.8

Step 3 in published LH mechanism is most likely a quasi-equilibrated reaction by combining the following two elementary steps.

3a) $MeOH^* + CO_2^* \rightleftharpoons MC^* + *$

3b) $MC^* + MeOH^* \rightleftharpoons DMC^* + H_2O^*$

If step 3a is the rate limiting while steps ahead of 3a are fast, then:

$$Rate = k_{3af} [MeOH^*][CO_2^*] \qquad \qquad \text{-Rate} = r_f - r_r \approx r_f \text{ in initial rate}$$

$$[CO_2^*] = \frac{k_{1f}}{k_{1r}} [CO_2] [*] \qquad \qquad \text{-From equil. cond. in step 1 (Sec. B)}$$

$$[MeOH^*] = \frac{k_{2f}}{k_{2r}} [MeOH] [*] \qquad \qquad \text{-From equil. cond. in step 2 (Sec. B)}$$

$$Rate = \frac{k_{3af}k_{1f}k_{2f}}{k_{1r}k_{2r}} [CO_2] [MeOH] [*]^2 \qquad \text{-Substitution. 1st order with respect}$$

$$\text{to MeOH}$$

If step 3b is the rate limiting while steps ahead of 3b are fast, then:

$$Rate = k_{3bf} [MC^*][MeOH^*] \qquad \qquad \text{-Rate} = r_f - r_r \approx r_f \text{ in initial rate}$$

$$[CO_2^*] = \frac{k_{1f}}{k_{1r}} [CO_2] [*] \qquad \qquad \text{-From equil. cond. in step 1 (Sec. B)}$$

$$[MeOH^*] = \frac{k_{2f}}{k_{2r}} [MeOH] [*] \qquad \qquad \text{-From equil. cond. in step 2 (Sec. B)}$$

$$[MC^*] = \frac{k_{3af}}{k_{3ar}} \frac{[MeOH^*] [CO_2^*]}{[*]} \qquad \qquad \text{-From equil. cond. in step 3a}$$

$$\text{Rate} = \frac{k_{3af}k_{3bf}k_{1f}k_{2f}{}^2}{k_{3ar}k_{1r}k_{2r}{}^2} [CO_2] [MeOH]^2 [*]^2 \qquad \text{-Substitution. 2nd order with respect}$$

to MeOH

Rate Law Derivation for Equation 4

D. Langmuir-Hinshelwood Mechanism Elementary Steps

1) $CO_2 + * \rightleftharpoons CO_2{}^*$

2) $MeOH + * \rightleftharpoons MeOH^*$

3) $2MeOH^* + CO_2{}^* \rightleftharpoons DMC^* + H_2O^* + *$

4) $DMC^* \rightleftharpoons DMC + *$

5) $H_2O^* \rightleftharpoons H_2O + *$

If CO_2 is rate determining and MeOH* is the most abundant reactive intermediate (*mari*):

1) $CO_2 + * \rightarrow CO_2{}^*$ $\qquad\qquad$ -k_1 rate constant

2) $MeOH + * \rightleftharpoons MeOH^*$ $\qquad\qquad$ -K_2 quasi equilibrated equilibrium constant

3') $2MeOH^* + CO_2{}^* \rightleftharpoons DMC + H_2O + 3*$ -Quasi equilibrated reaction combining steps

3-5

If step 1 is rate determining:

$\qquad$ Rate $= r_{1f} - r_{1r} \approx r_{1f}$ in initial rate region

$\qquad$ $r_{1f} = k_1 [CO_2] [*]$

$$K_2 = \frac{[MeOH^*]}{[MeOH][*]}$$ -From equilibrium condition step 2

$$[MeOH^*] = K_2 [MeOH][*]$$ -Cross multiplication

If MeOH is the *mari*

$$[*]_0 \approx [MeOH^*] + [*]$$

$$[*]_0 = K_2 [MeOH] [*] + [*]$$ - Substitution

$$[*]_0 = [*] (K_2 [MeOH] + 1)$$ - Associative

$$[*] = \frac{[*]_0}{K_2 [MeOH]+1}$$ - Divide sides by $K_2[MeOH] + 1$

$$Rate = r_1 = \frac{k_1 [CO_2] [*]_0}{K_2 [MeOH]+1}$$ - Substitution and QED

Chapter 8

SUMMARY AND FUTURE DIRECTIONS

8.1 Ceria catalyzed carbonate synthesis summary

Ceria is an effective catalyst for the conversion of CO_2 to dimethyl carbonate. With the use of ceria nanorods, the activation energy for the direct conversion was reduced to 65 kJ/mol compared with over 100 kJ/mol for bulk ceria particles. Additionally, the reaction rate order was observed to be positive and direct with catalyst loading, indicating that the catalyst surface was involved in the rate determining step and thus the reaction is taking place on the ceria surface. Additionally, the rate equation for the reaction is not positive for methanol, indicating that the rate is limited by the adsorption of CO_2 to the ceria surface, likely in a Langmuir-Hinshelwood type mechanism such as the one discussed at the end of Chapter 7. [1]

What is not known is just how CO_2 interacts with the ceria surface in order to become activated for the formation of organic carbonates. CO_2 is known to form a large number of surface carbonate species on the surfaces of bases, and we do not yet know which surface CO_2 species is involved in the formation of dimethyl carbonate.

8.2 FTIR investigations

We know that ceria is playing a role in adsorbing and activating CO_2 into a form that more readily reacts with methanol to form dimethyl carbonate. However, ceria is not a metallic surface: it is a highly ionic surface. Consequently, the surface charges are

highly localized and adsorption sites are not energetically equivalent. This means that improved catalytic performance would be achieved not just by improving the total amount of CO_2 on the surface, but by improving the amount of CO_2 adsorbed at the right locations. In other words, if the whole surface is not equivalent, we want to make sure that we have as many active sites as possible on the catalyst.

In order to investigate the structure of the adsorbed carbon dioxide on the catalysts, we deliberately omitted adding methanol to the reactor and instead only pressurized the reactor with CO_2 and heated the system to reaction temperature with stirring for two hours. Immediately after cooling and venting, the high pressure CO_2 treated catalyst was pressed in a pellet with KBr salt and the resulting Fourier Transform Infrared (FTIR) Spectroscopy spectrum was acquired within about 10 minutes of venting. The resulting spectra was compared to the indexed peaks from a recent experimental + DFT study by Vayssilov et al[2] with the results shown in Figure 8.1. As can be seen, a wide variety of carbonate structures are visible on the ceria surface with the most pronounced peaks at 1567, 1366, and 1161 cm^{-1}. These most pronounced peaks all correspond to polycarbonate vibration modes. According to Vayssilov, polycarbonate (OCOCO) species are less energetically favorable than single CO_2 molecules on the ceria surface. Instead, OCOCO only is expected to form once there is no longer a part of ceria available for interaction with CO_2. This is to be expected under supercritical conditions as CO_2 serves as the solvent molecule in the direct synthesis of DMC.
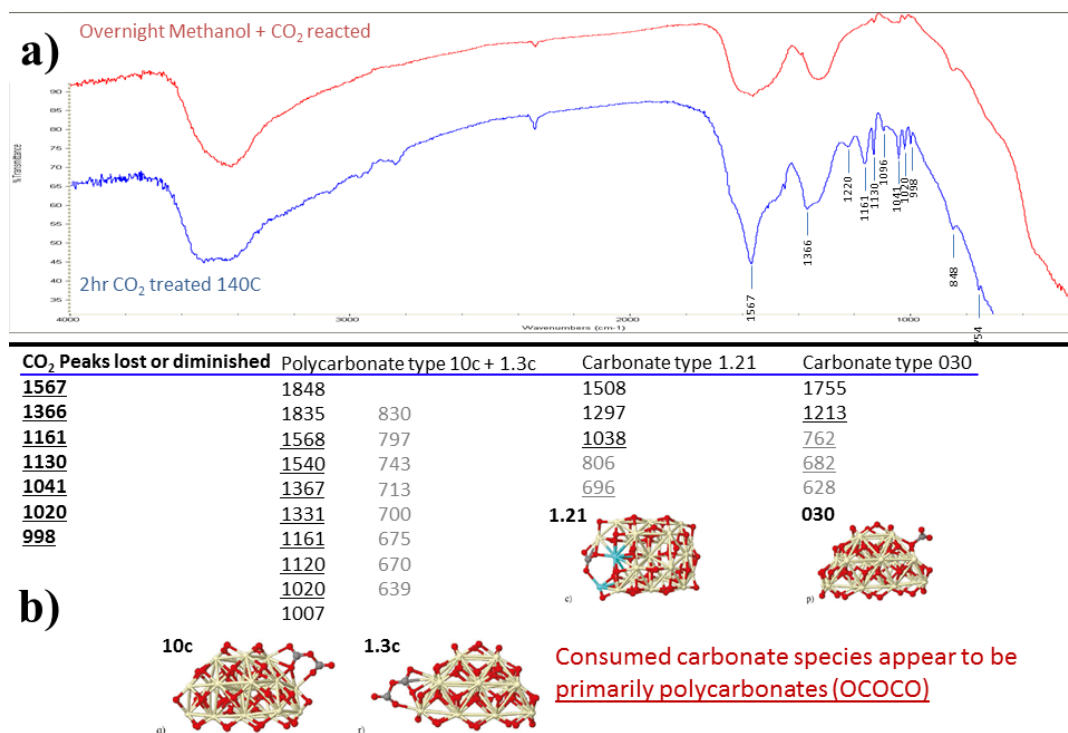
Figure 8.1 (a) FTIR transmission spectra of CO_2 treated ceria directly after cooling and venting (Blue) and after a subsequent treatment with methanol (red). Note the pronounced peaks from 1567 cm^{-1} to about 1000 cm^{-1} which are removed after reacting with methanol at room temperature. (b) Peak positions (in cm^{-1}) which were found to be removed by the methanol compared to peak positions published for CO_2 on ceria. The majority of the sharp peaks removed by methanol correspond to polycarbonates of type 10c and 1.3c as shown. Underlined wavenumbers indicate a match, while values below 900 cm^{-1} are ghosted out due to those values largely falling outside the transmission window for the instrument. Structures adapted with permission from reference[2]. Copyright 2011 American Chemical Society.
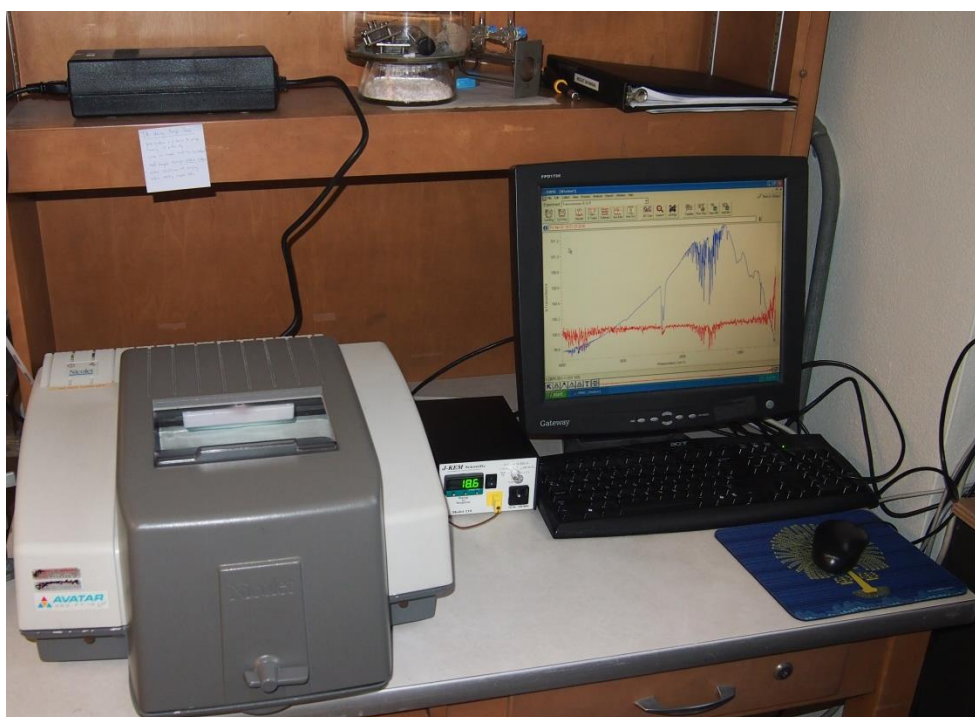
Figure 8.2 Nicolet Avatar 360 utilized for investigation of surface carbonates.

What is interesting is just how intense the peaks corresponding to polycarbonate are on the ceria under reaction conditions. Considering that OCOCO is in a higher energy form of CO_2 compared to isolated CO_2 on the surface, it may be that this moiety is the activated form of CO_2 involved in the reaction with methanol, as suggested by the fact that exposure to methanol at room temperature was enough to remove the polycarbonate peaks while leaving behind broad bands of more stable carbonates. Finally, it was noted by Vayssilov et al that various CO_2 chemisorption species are more prevalent on differing ceria surfaces with polycarbonate species preferring nanoparticle faces and edges.

8.3 Facet investigations

In order to give further insights into the active sites on our ceria nanorods, we have also prepared ceria nano-octahedra and nano-cubes which display primarily (111) and (100) facets respectively (Figure 8.3). The ceria nano-octahedra manifested a reduced surface area compared to the nanorods (19 m^2/g compared to 82 m^2/g), so judging by the ~first order rate equation with respect to the catalyst loading, the octahedra would be expected to show one forth the rate of the nanorods for the production of DMC. Instead, this rate was found to be one fiftieth of that observed for ceria nanorods (~0.005 instead of 0.25 %DMC/hr). Likewise, ceria nano-cubes display a decreased surface area of 35 m^2/g and we would expect to see some decrease in the rate of DMC production compared to nanorods. However, these show a rate of just one fiftieth of that of the nanorods (~0.005 %DMC/hr), suggesting that neither the 111 nor the 100 facet is the active surface on the nanorod catalysts.
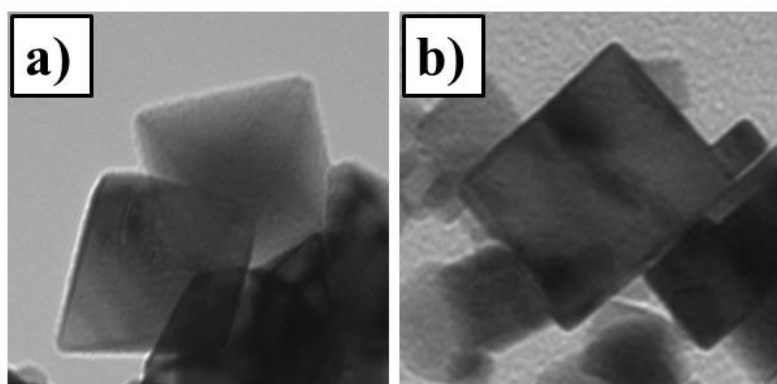
Figure 8.3 TEM images of (a) ceria nano-octahedra and (b) ceria nano-cubes. The edge lengths of the largest shown nanoparticles in each is roughly 50 nm.

8.4 Future work

The rate equation derived in Chapter 7 could be further improved by measuring the reaction initial rate while varying the concentration of CO_2. If the rate equation derived from the proposed Langmuir-Hinshelwood mechanism is correct, then we would expect to see a first order relationship between the initial rate and CO_2 concentration. However, if the active species of CO_2 on the catalyst surface is a polycarbonate, then it is expected that the reaction order will be closer to two with respect to CO_2. Determining this rate order is complicated by the direct synthesis of DMC having an activation volume, meaning that system pressures need to be kept constant. This could be achieved by adding argon gas into the reactor (through a one-way valve) with CO_2 when pressurizing the reactor such that the pressure at the reaction temperature remains the same 2000 psi, then measuring the initial rates of reaction versus CO_2 partial pressure.

Since the activation energy for the direct synthesis of DMC from CO_2 and methanol has been calculated, and we know that the adsorption of CO_2 is the rate determining step, it may then be possible to determine which moiety of CO_2 on ceria is the active intermediate by quantitative FTIR. To do this, the formation rates of the various carbonates would need to be determined at multiple reaction temperatures. Since the IR absorption peak area is proportional to the amount of carbonate present, the change in integrated area for a given peak should correspond with the change in concentration. The carbonate species that is the active intermediate should have an activation energy of ~65 kJ/mol, while the remaining carbonate species are side products and should be avoided in order to improve catalyst selectivity.

The facet studies of ceria suggest that neither the (111) nor the (100) crystal facets are the active sites on our ceria nanorods. [3] Considering that these are the most prevalent ceria surfaces, this suggests that a relatively small amount of our catalyst is active for the conversion of CO_2 to DMC, possibly just the (110) or (211) facets present at the tip of ceria nanorods. If this is the case, then it should be possible to improve the activity of our catalysts by growing longer and wider nanorods, then aggressively sonicating them to expose a larger amount of (110) facets. Considering the large difference in rates observed for nanorods versus cubes, we expect that such a catalyst may offer huge improvements in catalytic rates for the production of organic carbonates.

Finally, once a ceria catalyst has been selected which provides optimal rates and selectivity for the direct synthesis of DMC from CO_2 and methanol, this catalyst should be tested for the formation of other carbonates from CO_2 and alcohols. In particular, a catalyst which offers good rates for the direct synthesis of diphenyl carbonate from CO_2 and phenol could transform the polycarbonate plastic industry while consuming large sums of carbon dioxide.

8.5 References

1.   Santos, B. A. V.; Pereira, C. S. M.; Silva, V. M. T. M.; Loureiro, J. M.; Rodrigues, A. E., Kinetic study for the direct synthesis of dimethyl carbonate from methanol and CO_2 over CeO_2 at high pressure conditions. *Applied Catalysis A: General* **2013,** *455*, 219-226.

2.   Vayssilov, G. N.; Mihaylov, M.; Petkov, P. S.; Hadjiivanov, K. I.; Neyman, K. M., Reassignment of the Vibrational Spectra of Carbonates, Formates, and Related Surface Species on Ceria: A Combined Density Functional and Infrared Spectroscopy Investigation. *The Journal of Physical Chemistry C* **2011,** *115*, 23435-23454.

3.   Sakthivel, T. S.; Reid, D. L.; Bhatta, U. M.; Mobus, G.; Sayle, D. C.; Seal, S., Engineering of nanoscale defect patterns in CeO_2 nanorods via ex situ and in situ annealing. *Nanoscale* **2015,** *7*, 5169-5177.